Gallagher, S.J., Fulthorpe, C.S., Bogus, K., and the Expedition 356 Scientists
Proceedings of the International Ocean Discovery Program Volume 356
publications.iodp.org

doi:10.14379/iodp.proc.356.109.2017

Site U1464[1]

S.J. Gallagher, C.S. Fulthorpe, K. Bogus, G. Auer, S. Baranwal, I.S. Castañeda, B.A. Christensen, D. De Vleeschouwer, D.R. Franco, J. Groeneveld, M. Gurnis, C. Haller, Y. He, J. Henderiks, T. Himmler, T. Ishiwa, H. Iwatani, R.S. Jatiningrum, M.A. Kominz, C.A. Korpanty, E.Y. Lee, E. Levin, B.L. Mamo, H.V. McGregor, C.M. McHugh, B.F. Petrick, D.C. Potts, A. Rastegar Lari, W. Renema, L. Reuning, H. Takayanagi, and W. Zhang[2]

Keywords: International Ocean Discovery Program, IODP, Expedition 356, *JOIDES Resolution*, Site U1464, Roebuck Basin, Indonesian Throughflow, Miocene, Pliocene, Pleistocene, Australian monsoon, subsidence, aridity, anhydrite, sabkha, reefs, Rowley Shoals, tropical carbonates

Contents

Background and objectives

At 270 m water depth, International Ocean Discovery Program (IODP) Site U1464 is currently in an outer ramp setting (James et al., 2004), ~50 km southeast of the Rowley Shoals (Figures **F1**, **F2**). The seabed in the vicinity of the site is poorly sorted, carbonate-rich (>90%) sediment made up of bioclastic gravel, sand, and mud (Jones, 1973; James et al., 2004). Site U1464 is 5 km updip from a drowned "fossil" shoal described by Jones (1973) and Ryan et al. (2009) and is connected to the site by parallel laterally persistent reflectors on seismic Profile JN87-07 (Figure **F3**). Therefore, improved ages for these reflectors may allow us to date the initiation and demise of this reef/shoal.

The proximity of Site U1464 to a previously identified drowned shoal makes this site unique and significant. Stratigraphic data and paleobathymetric determinations obtained will allow robust estimates of the subsidence history of this part of the northwest shelf and its role in carbonate platform drowning.

As the most northern site of the Expedition 356 coring transect, the sediment and biota at Site U1464 are likely to record strong Western Pacific Warm Pool and Indonesian Throughflow signals vital to understanding the (geo)history of these important oceanic features. The strata of this site should also contain a Pliocene–Pleistocene record of the Australian monsoon and aridity.

Operations

Transit to Site U1464

After the 79 nmi transit from IODP Site U1463 averaging 10.7 kt, the vessel arrived at Site U1464 at 0348 h (UTC + 8 h) on 19 September 2015. Shortly after arrival (0430 h), a seafloor positioning beacon was deployed.

Site U1464

The original plan for Site U1464 was to core four holes: three advanced piston corer (APC) holes to refusal, with the last two holes being extended to 600 m or refusal with the extended core barrel (XCB) system. The final hole was intended to be a deep hole to total depth (840 meters below seafloor [mbsf]) cored with the rotary core barrel (RCB) system. We began the first hole (U1464A) with the XCB system to ensure that the surface sediments were suitable for piston coring. After two cores, we determined that the APC system would be appropriate. The second hole (U1464B) was piston cored with both the APC and half-length APC (HLAPC) systems to 316.9 m drilling depth below seafloor (DSF). After completing the piston coring to refusal, we decided to core the deep hole with the RCB system. Subsequently, this allowed us to accurately allocate time for the remainder of the site. After preparing the RCB system and starting Hole U1464C, the hole was advanced by drilling without coring to 308.0 m DSF with a center bit installed. The center bit was pulled and RCB coring continued to a final depth of 840.0 m DSF. The hole was conditioned for logging and the bit was dropped to the bottom of the hole. While pulling the drill string to logging depth (86.88 m DSF), the hole was displaced with heavy mud from 363.1 m DSF to the seafloor. The triple combination (combo) tool string was assembled and deployed. The tool string performed a downlog to 783.7 m wireline log depth below seafloor (WSF), 56.3 m from the bottom of Hole U1464C. While logging up with the calipers open, the hole collapsed, trapping the tool string at 619.1 m WSF. The triple combo was successfully recovered after stripping over the wireline and washing over the tool string with the drill pipe. The tool string was pulled to the surface with two T-bars and laid out to the storage racks. During recovery of the logging tool string, we had to stop rotating the drill string, and as a result it became stuck in the hole; it was recovered with overpull, rotation, and pumping, and the drill

[1] Gallagher, S.J., Fulthorpe, C.S., Bogus, K., Auer, G., Baranwal, S., Castañeda, I.S., Christensen, B.A., De Vleeschouwer, D., Franco, D.R., Groeneveld, J., Gurnis, M., Haller, C., He, Y., Henderiks, J., Himmler, T., Ishiwa, T., Iwatani, H., Jatiningrum, R.S., Kominz, M.A., Korpanty, C.A., Lee, E.Y., Levin, E., Mamo, B.L., McGregor, H.V., McHugh, C.M., Petrick, B.F., Potts, D.C., Rastegar Lari, A., Renema, W., Reuning, L., Takayanagi, H., and Zhang, W., 2017. Site U1464. *In* Gallagher, S.J., Fulthorpe, C.S., Bogus, K., and the Expedition 356 Scientists, *Indonesian Throughflow*. Proceedings of the International Ocean Discovery Program, 356: College Station, TX (International Ocean Discovery Program). http://dx.doi.org/10.14379/iodp.proc.356.109.2017

[2] **Expedition 356 Scientists' addresses.**

MS 356-109: Published 26 February 2017

Figure F1. Map of the northwest shelf showing major basins and location of modern and "fossil" reefs. Stars = Expedition 356 sites, green circles = Deep Sea Drilling Project/Ocean Drilling Program sites and other core locations referred to in text, yellow circles = industry well locations (Angel = Angel-1; G2/6/7 = Goodwyn-2, Goodwyn-6, Goodwyn-7; A1 = Austin-1; M/MN1 = Maitland/Maitland North-1; TR1 = West Tryal Rocks-1). WA = Western Australia, NT = Northern Territory, SA = South Australia, QLD = Queensland, NSW = New South Wales.

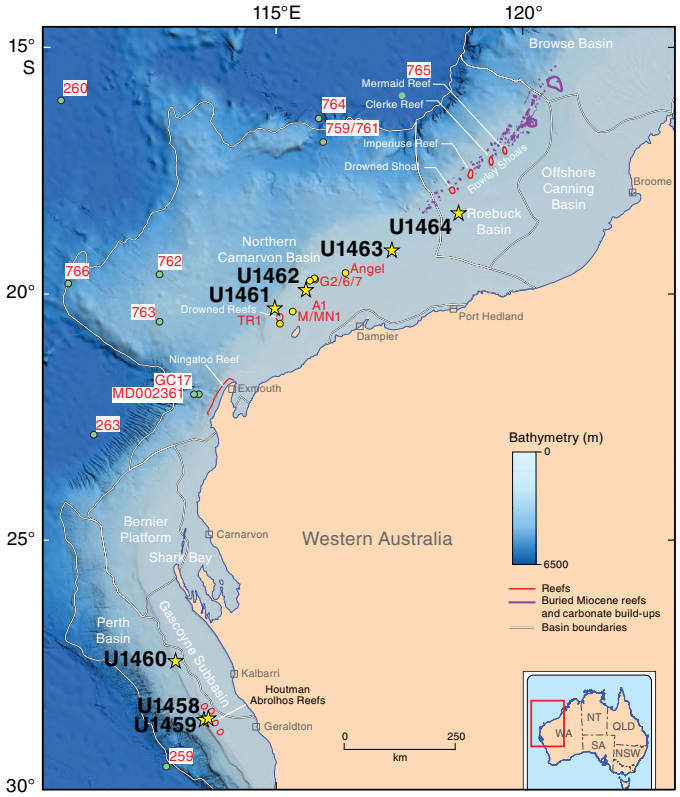

string was then pulled back to the surface. With over two days of operational time remaining, the APC/XCB coring system was reassembled and Hole U1464D was started. We first used the APC system to core to 293.5 m DSF. All APC cores were oriented and six in situ temperature measurements were taken. After reaching refusal, the coring system was switched over to the XCB system and coring continued to a final depth of 529.6 m DSF. The last core was on deck at 1410 h on 26 September 2015. The drill string was pulled back to the surface and the rig floor secured, ending Expedition 356 coring operations at 2100 h on 26 September. The total time spent on Site U1464 was 185.25 h (7.7 days) (Tables **T1**, **T2**).

We cored 606.7 m with the APC system and recovered 554.41 m of core (91%). The HLAPC system cored 3.7 m and recovered 3.75 m of core (101%), whereas 255.5 m was cored with the XCB system, recovering 34.85 m of core (14%). The RCB system was used to core 532.0 m and recovered 94.03 m of core (18%). The overall recovery for Site U1464 was 49%.

Hole U1464A

After a 79 nmi transit (7.4 h) from Site U1463, we arrived at Site U1464 at 0348 h on 19 September. The APC/XCB bottom-hole assembly (BHA) was assembled, and we decided to begin Hole U1464A (18°03.9125′S, 118°37.8824′E) with the XCB coring system to establish the character of the upper sediments. The seafloor was tagged at 260.0 meters below sea level (mbsl) and an XCB core barrel was dropped. Hole U1464A was started at 0655 h on 19 September, and Cores 356-U1464A-1X and 2X were cut to 19.4 m DSF with no recovery (0%). The sediment was deemed appropriate for APC coring. Hole U1464A was terminated at 0845 h. The total time spent on Hole U1464A was 5.0 h (0.2 days).

Hole U1464B

The vessel was offset 20 m east, a nonmagnetic APC core barrel was dressed with a core liner, and Hole U1464B (18°03.9115′S, 118°37.8935′E) was started at 0915 h on 19 September. Based on the recovery of the mudline core (2.26 m), the seafloor depth was calcu-

Figure F2. Bathymetric map showing the seafloor around Sites U1463 and U1464. Bathymetric data are derived from the Geoscience Australia Australian bathymetry and topography grid, June 2009. The positions of multichannel seismic profiles are shown. Red dots = locations of preexisting industry wells.

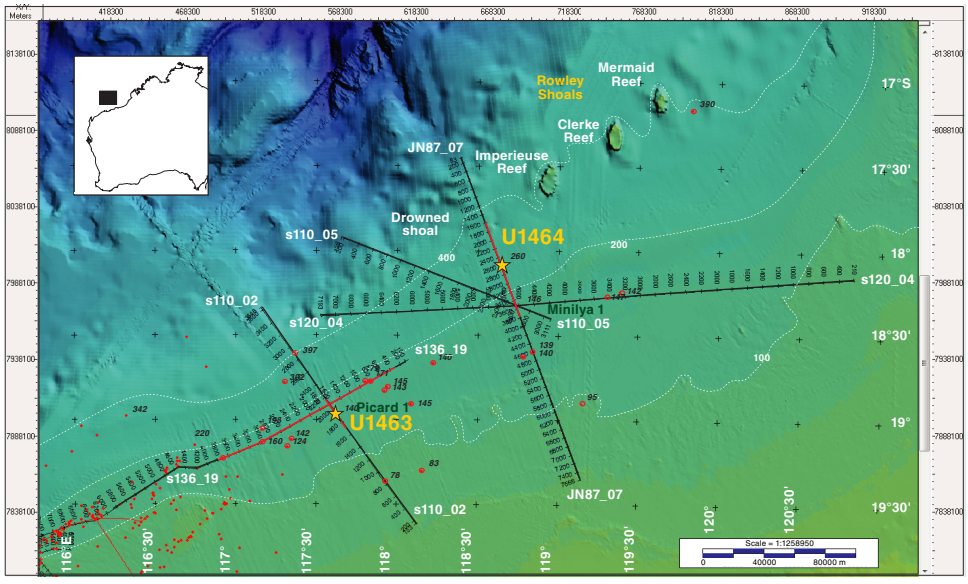

Figure F3. Multichannel seismic profile across Site U1464 showing the targeted reflector at 840 mbsf.

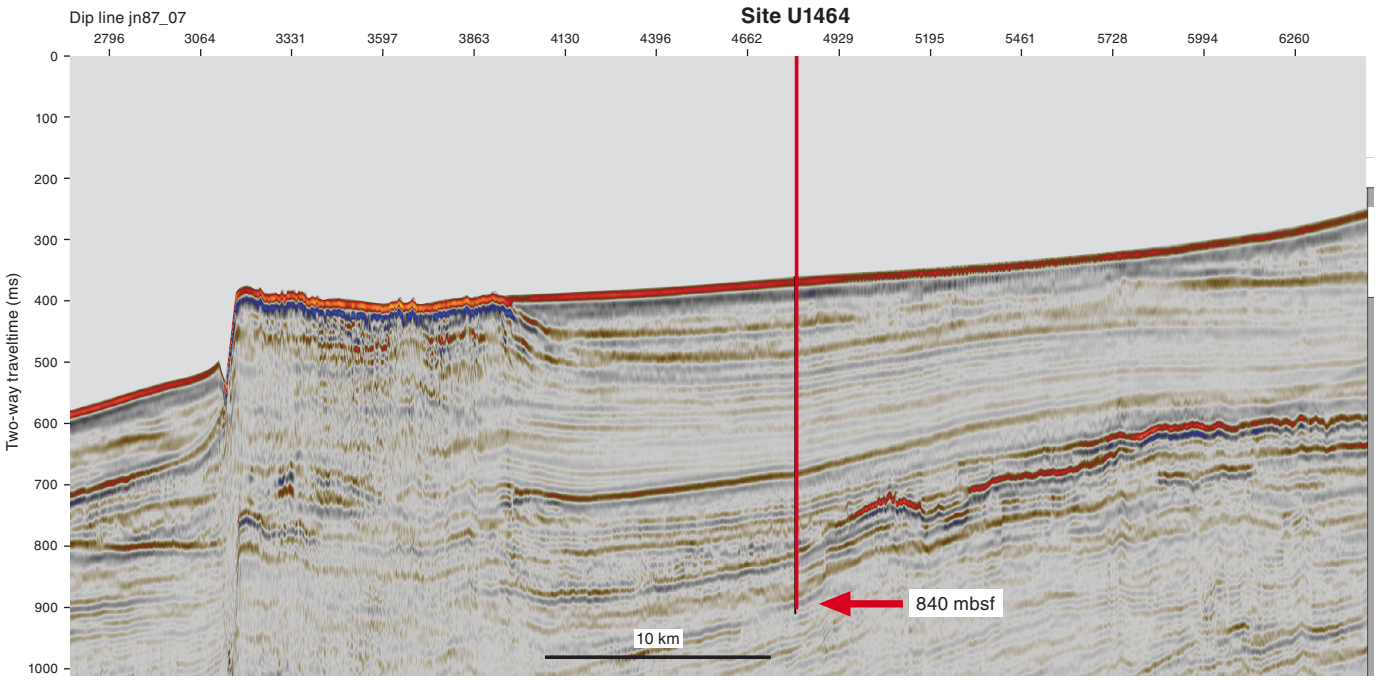

Table T1. Operations summary, Site U1464. mbsl = meters below sea level. **Download table in .csv format.**

Hole	Latitude	Longitude	Water depth (mbsl)	Penetration DSF (m)	Cored interval (m)	Recovered length (m)	Recovery (%)	Drilled interval (m)	Drilled interval (*N*)	Total cores (*N*)	APC cores (*N*)	HLAPC cores (*N*)	XCB cores (*N*)	RCB cores (*N*)	Time on hole (days)
U1464A	18°03.9125′S	118°37.8824′E	259.96	19.40	19.40		0		0	2	0	0	2	0	0.21
U1464B	18°03.9115′S	118°37.8935′E	264.26	316.90	316.90	292.27	92		0	35	34	1	0	0	0.9
U1464C	18°03.9244′S	118°37.8942′E	264.24	840.00	532.00	94.03	18	308.00	1	55	0	0	0	55	4.09
U1464D	18°03.9230′S	118°37.8836′E	264.43	529.60	529.60	300.74	57		0	58	32	0	26	0	2.52
			Totals:	1705.90	1397.90	687.04		308.00	1	150	66	1	28	55	

Table T2. Site U1464 core summary. DSF = drilling depth below seafloor, CSF = core depth below seafloor. F = half-length advanced piston corer, H = advanced piston corer, R = rotary core barrel, X = extended core barrel, numeric core type = drilled interval. (Continued on next two pages.) **Download table in .csv format.**

Core	Top depth drilled DSF (m)	Bottom depth drilled DSF (m)	Advanced (m)	Recovered length (m)	Curated length (m)	Top depth cored CSF (m)	Bottom depth recovered CSF (m)	Recovery (%)	Date (2015)	Time on deck UTC (h)
356-U1464A-										
1X	0.00	9.70	9.7		0.00	0.00	9.70		18 Sep	2345
2X	9.70	19.40	9.7		0.00	9.70	19.40		19 Sep	0030
356-U1464B-										
1H	0.00	2.20	2.2	2.26	2.26	0.00	2.26	103	19 Sep	0120
2H	2.20	11.70	9.5	9.31	9.31	2.20	11.51	98	19 Sep	0150
3H	11.70	21.20	9.5	9.46	9.46	11.70	21.16	100	19 Sep	0220
4H	21.20	30.70	9.5	9.62	9.62	21.20	30.82	101	19 Sep	0235
5H	30.70	40.20	9.5	9.87	9.87	30.70	40.57	104	19 Sep	0255
6H	40.20	49.70	9.5	9.62	9.62	40.20	49.82	101	19 Sep	0315
7H	49.70	59.20	9.5	9.76	9.76	49.70	59.46	103	19 Sep	0340
8H	59.20	68.70	9.5	9.94	9.94	59.20	69.14	105	19 Sep	0405
9H	68.70	78.20	9.5	9.71	9.71	68.70	78.41	102	19 Sep	0425
10H	78.20	87.70	9.5	9.97	9.97	78.20	88.17	105	19 Sep	0440
11H	87.70	97.20	9.5	9.72	9.72	87.70	97.42	102	19 Sep	0505
12H	97.20	106.70	9.5	9.72	9.72	97.20	106.92	102	19 Sep	0525
13H	106.70	116.20	9.5	9.98	9.98	106.70	116.68	105	19 Sep	0540
14H	116.20	125.70	9.5	10.10	10.10	116.20	126.30	106	19 Sep	0600
15H	125.70	135.20	9.5	9.34	9.34	125.70	135.04	98	19 Sep	0620
16H	135.20	144.70	9.5	9.85	9.85	135.20	145.05	104	19 Sep	0640
17H	144.70	154.20	9.5	9.84	9.84	144.70	154.54	104	19 Sep	0700

Table T2 (continued). (Continued on next page.)

Core	Top depth drilled DSF (m)	Bottom depth drilled DSF (m)	Advanced (m)	Recovered length (m)	Curated length (m)	Top depth cored CSF (m)	Bottom depth recovered CSF (m)	Recovery (%)	Date (2015)	Time on deck UTC (h)
18H	154.20	163.70	9.5	8.80	8.80	154.20	163.00	93	19 Sep	0730
19H	163.70	173.20	9.5	6.53	6.53	163.70	170.23	69	19 Sep	0750
20H	173.20	180.20	7.0	7.00	7.00	173.20	180.20	100	19 Sep	0820
21H	180.20	189.70	9.5	7.12	7.12	180.20	187.32	75	19 Sep	0855
22H	189.70	199.20	9.5	6.95	6.95	189.70	196.65	73	19 Sep	0930
23H	199.20	208.70	9.5	9.47	9.47	199.20	208.67	100	19 Sep	0955
24H	208.70	218.20	9.5	7.00	7.00	208.70	215.70	74	19 Sep	1020
25H	218.20	227.70	9.5	8.23	8.23	218.20	226.43	87	19 Sep	1045
26H	227.70	237.20	9.5	7.55	7.55	227.70	235.25	79	19 Sep	1115
27H	237.20	246.70	9.5	7.66	7.66	237.20	244.86	81	19 Sep	1140
28H	246.70	256.20	9.5	8.03	8.03	246.70	254.73	85	19 Sep	1205
29H	256.20	265.70	9.5	7.32	7.32	256.20	263.52	77	19 Sep	1230
30H	265.70	275.20	9.5	6.92	6.92	265.70	272.62	73	19 Sep	1305
31H	275.20	284.70	9.5	6.34	6.34	275.20	281.54	67	19 Sep	1330
32H	284.70	294.20	9.5	8.45	8.45	284.70	293.15	89	19 Sep	1415
33H	294.20	303.70	9.5	8.03	8.03	294.20	302.23	85	19 Sep	1450
34H	303.70	313.20	9.5	9.05	9.05	303.70	312.75	95	19 Sep	1730
35F	313.20	316.90	3.7	3.75	3.75	313.20	316.95	101	19 Sep	1850
356-U1464C-										
11			***** Drilled interval from 0.00 to 308.00 m DSF *****						20 Sep	0755
2R	308.00	317.70	9.7	5.47	5.47	308.00	313.47	56	20 Sep	0830
3R	317.70	327.40	9.7	1.22	1.22	317.70	318.92	13	20 Sep	0855
4R	327.40	337.10	9.7	0.02	0.02	327.40	327.42	0	20 Sep	0930
5R	337.10	346.80	9.7	0.26	0.26	337.10	337.36	3	20 Sep	1010
6R	346.80	356.50	9.7	0.33	0.33	346.80	347.13	3	20 Sep	1055
7R	356.50	366.20	9.7	0.41	0.41	356.50	356.91	4	20 Sep	1135
8R	366.20	375.90	9.7	0.93	0.93	366.20	367.13	10	20 Sep	1230
9R	375.90	385.60	9.7	0.34	0.34	375.90	376.24	4	20 Sep	1315
10R	385.60	395.30	9.7	0.80	0.80	385.60	386.40	8	20 Sep	1400
11R	395.30	405.00	9.7	0.44	0.44	395.30	395.74	5	20 Sep	1500
12R	405.00	414.70	9.7	0.21	0.21	405.00	405.21	2	20 Sep	1530
13R	414.70	424.40	9.7	0.77	0.77	414.70	415.47	8	20 Sep	1620
14R	424.40	434.10	9.7	0.79	0.79	424.40	425.19	8	20 Sep	1705
15R	434.10	443.80	9.7	0.38	0.38	434.10	434.48	4	20 Sep	1800
16R	443.80	453.50	9.7	1.72	1.72	443.80	445.52	18	20 Sep	1850
17R	453.50	463.20	9.7	0.42	0.42	453.50	453.92	4	20 Sep	1940
18R	463.20	472.90	9.7	1.57	1.57	463.20	464.77	16	20 Sep	2035
19R	472.90	482.60	9.7	3.87	3.87	472.90	476.77	40	20 Sep	2125
20R	482.60	492.30	9.7	2.05	2.05	482.60	484.65	21	20 Sep	2225
21R	492.30	502.00	9.7	4.05	4.05	492.30	496.35	42	20 Sep	2330
22R	502.00	511.70	9.7	6.25	6.25	502.00	508.25	64	21 Sep	0105
23R	511.70	521.40	9.7	1.87	1.87	511.70	513.57	19	21 Sep	0210
24R	521.40	531.10	9.7	2.27	2.27	521.40	523.67	23	21 Sep	0310
25R	531.10	540.80	9.7	6.66	6.66	531.10	537.76	69	21 Sep	0445
26R	540.80	550.50	9.7	0.87	0.87	540.80	541.67	9	21 Sep	0530
27R	550.50	560.20	9.7	3.16	3.16	550.50	553.66	33	21 Sep	0620
28R	560.20	569.90	9.7	2.86	2.86	560.20	563.06	29	21 Sep	0700
29R	569.90	579.60	9.7	1.77	1.77	569.90	571.67	18	21 Sep	0745
30R	579.60	589.30	9.7	0.31	0.31	579.60	579.91	3	21 Sep	0825
31R	589.30	599.00	9.7	1.57	1.57	589.30	590.87	16	21 Sep	0920
32R	599.00	608.70	9.7	1.10	1.10	599.00	600.10	11	21 Sep	1005
33R	608.70	618.40	9.7	2.82	2.82	608.70	611.52	29	21 Sep	1110
34R	618.40	628.10	9.7	2.42	2.42	618.40	620.82	25	21 Sep	1200
35R	628.10	637.80	9.7	0.30	0.30	628.10	628.40	3	21 Sep	1245
36R	637.80	647.50	9.7	0.14	0.14	637.80	637.94	1	21 Sep	1340
37R	647.50	657.20	9.7	2.15	2.15	647.50	649.65	22	21 Sep	1430
38R	657.20	666.90	9.7	2.08	2.08	657.20	659.28	21	21 Sep	1510
39R	666.90	676.60	9.7	0.73	0.73	666.90	667.63	8	21 Sep	1550
40R	676.60	686.30	9.7	2.00	2.00	676.60	678.60	21	21 Sep	1650
41R	686.30	696.00	9.7	0.77	0.77	686.30	687.07	8	21 Sep	1740
42R	696.00	705.70	9.7	0.43	0.43	696.00	696.43	4	21 Sep	1835
43R	705.70	715.40	9.7	1.87	1.87	705.70	707.57	19	21 Sep	1930
44R	715.40	725.10	9.7	0.60	0.60	715.40	716.00	6	21 Sep	2020
45R	725.10	734.80	9.7	3.04	3.04	725.10	728.14	31	21 Sep	2105
46R	734.80	744.50	9.7	3.33	3.33	734.80	738.13	34	21 Sep	2205
47R	744.50	754.20	9.7	0.88	0.88	744.50	745.38	9	21 Sep	2255
48R	754.20	763.90	9.7	0.67	0.67	754.20	754.87	7	21 Sep	2345

Table T2 (continued).

Core	Top depth drilled DSF (m)	Bottom depth drilled DSF (m)	Advanced (m)	Recovered length (m)	Curated length (m)	Top depth cored CSF (m)	Bottom depth recovered CSF (m)	Recovery (%)	Date (2015)	Time on deck UTC (h)
49R	763.90	773.60	9.7	2.82	2.82	763.90	766.72	29	22 Sep	0050
50R	773.60	783.30	9.7	3.07	3.07	773.60	776.67	32	22 Sep	0150
51R	783.30	793.00	9.7	0.79	0.79	783.30	784.09	8	22 Sep	0245
52R	793.00	802.70	9.7	1.75	1.75	793.00	794.75	18	22 Sep	0350
53R	802.70	812.40	9.7	3.13	3.13	802.70	805.83	32	22 Sep	0440
54R	812.40	822.10	9.7	0.92	0.92	812.40	813.32	9	22 Sep	0530
55R	822.10	831.80	9.7	1.48	1.48	822.10	823.58	15	22 Sep	0620
56R	831.80	840.00	8.2	1.10	1.10	831.80	832.90	13	22 Sep	0730
356-U1464D-										
1H	0.00	3.50	3.5	3.55	3.55	0.00	3.55	101	24 Sep	0610
2H	3.50	13.00	9.5	9.66	9.66	3.50	13.16	102	24 Sep	0655
3H	13.00	22.50	9.5	9.40	9.40	13.00	22.40	99	24 Sep	0725
4H	22.50	32.00	9.5	9.71	9.71	22.50	32.21	102	24 Sep	0755
5H	32.00	41.50	9.5	9.85	9.85	32.00	41.85	104	24 Sep	0830
6H	41.50	51.00	9.5	9.83	9.83	41.50	51.33	103	24 Sep	0855
7H	51.00	60.50	9.5	9.89	9.89	51.00	60.89	104	24 Sep	0925
8H	60.50	70.00	9.5	10.08	10.08	60.50	70.58	106	24 Sep	1000
9H	70.00	79.50	9.5	9.88	9.88	70.00	79.88	104	24 Sep	1030
10H	79.50	89.00	9.5	9.90	9.90	79.50	89.40	104	24 Sep	1100
11H	89.00	98.50	9.5	9.98	9.98	89.00	98.98	105	24 Sep	1125
12H	98.50	108.00	9.5	9.79	9.79	98.50	108.29	103	24 Sep	1200
13H	108.00	117.50	9.5	9.89	9.89	108.00	117.89	104	24 Sep	1230
14H	117.50	127.00	9.5	9.97	9.97	117.50	127.47	105	24 Sep	1255
15H	127.00	136.50	9.5	9.92	9.92	127.00	136.92	104	24 Sep	1325
16H	136.50	146.00	9.5	10.03	10.03	136.50	146.53	106	24 Sep	1405
17H	146.00	155.50	9.5	9.90	9.90	146.00	155.90	104	24 Sep	1435
18H	155.50	165.00	9.5	8.13	8.13	155.50	163.63	86	24 Sep	1505
19H	165.00	173.20	8.2	8.23	8.23	165.00	173.23	100	24 Sep	1525
20H	173.20	182.70	9.5	8.91	8.91	173.20	182.11	94	24 Sep	1620
21H	182.70	192.20	9.5	7.00	7.00	182.70	189.70	74	24 Sep	1700
22H	192.20	201.70	9.5	7.97	7.97	192.20	200.17	84	24 Sep	1755
23H	201.70	211.20	9.5	9.81	9.81	201.70	211.51	103	24 Sep	1835
24H	211.20	220.70	9.5	6.32	6.32	211.20	217.52	67	24 Sep	1910
25H	220.70	230.20	9.5	7.70	7.70	220.70	228.40	81	24 Sep	1950
26H	230.20	239.70	9.5	6.57	6.57	230.20	236.77	69	24 Sep	2030
27H	239.70	249.20	9.5	5.99	5.99	239.70	245.69	63	24 Sep	2105
28H	249.20	258.70	9.5	7.41	7.41	249.20	256.61	78	24 Sep	2205
29H	258.70	268.20	9.5	5.95	5.95	258.70	264.65	63	24 Sep	2250
30H	268.20	277.70	9.5	4.64	4.64	268.20	272.84	49	24 Sep	2335
31H	277.70	287.20	9.5	3.69	3.69	277.70	281.39	39	25 Sep	0025
32H	287.20	293.50	6.3	6.34	6.34	287.20	293.54	101	25 Sep	0105
33X	293.50	299.30	5.8	9.00	9.00	293.50	302.50	155	25 Sep	0240
34X	299.30	309.00	9.7	9.80	9.80	299.30	309.10	101	25 Sep	0405
35X	309.00	318.70	9.7	0.59	0.59	309.00	309.59	6	25 Sep	0500
36X	318.70	328.40	9.7	0.75	0.75	318.70	319.45	8	25 Sep	0620
37X	328.40	338.10	9.7	0.12	0.12	328.40	328.52	1	25 Sep	0710
38X	338.10	347.80	9.7	0.89	0.89	338.10	338.99	9	25 Sep	0800
39X	347.80	357.50	9.7	0.39	0.39	347.80	348.19	4	25 Sep	0850
40X	357.50	367.20	9.7	0.00	0.00	357.50	357.50	0	25 Sep	0945
41X	367.20	376.90	9.7	0.06	0.06	367.20	367.26	1	25 Sep	1045
42X	376.90	386.60	9.7	0.08	0.08	376.90	376.98	1	25 Sep	1140
43X	386.60	396.30	9.7	0.21	0.21	386.60	386.81	2	25 Sep	1245
44X	396.30	406.00	9.7	0.13	0.13	396.30	396.43	1	25 Sep	1340
45X	406.00	415.70	9.7	0.30	0.30	406.00	406.30	3	25 Sep	1430
46X	415.70	425.40	9.7	0.15	0.15	415.70	415.85	2	25 Sep	1530
47X	425.40	435.10	9.7	0.10	0.10	425.40	425.50	1	25 Sep	1630
48X	435.10	444.80	9.7	0.27	0.27	435.10	435.37	3	25 Sep	1730
49X	444.80	454.50	9.7	0.53	0.53	444.80	445.33	5	25 Sep	1830
50X	454.50	464.20	9.7	0.10	0.10	454.50	454.60	1	25 Sep	1925
51X	464.20	473.90	9.7	0.46	0.46	464.20	464.66	5	25 Sep	2040
52X	473.90	483.60	9.7	0.95	0.95	473.90	474.85	10	25 Sep	2145
53X	483.60	493.30	9.7	0.08	0.08	483.60	483.68	1	25 Sep	2250
54X	493.30	503.00	9.7	0.63	0.63	493.30	493.93	6	25 Sep	0000
55X	503.00	507.80	4.8	3.91	3.91	503.00	506.91	81	26 Sep	0130
56X	507.80	512.70	4.9	3.15	3.15	507.80	510.95	64	26 Sep	0310
57X	512.70	522.40	9.7	0.63	0.63	512.70	513.33	6	26 Sep	0435
58X	522.40	529.60	7.2	1.57	1.57	522.40	523.97	22	26 Sep	0610

lated to be 264.3 mbsl. Coring continued through Core 34H to 313.2 m DSF with the APC system. The HLAPC system was then deployed and we recovered Cores 33F through 35F to 316.9 m DSF by advancing by recovery. Two of these HLAPC cores (33F and 35F) required drillover to release the core barrel from the formation, indicating that piston coring refusal was reached at 0240 h on 20 September. At the conclusion of coring, the drill string was recovered and Hole U1464B ended at 0615 h. Overall, the APC system advanced 313.2 m and recovered 288.52 m of core (92%), whereas the HLAPC system advanced 3.7 m and recovered 3.75 m of core (101%). The total time spent on Hole U1464B was 21.5 h (0.9 days).

Hole U1464C

After offsetting the vessel 20 m south of Hole U1464B, the RCB coring system was assembled and Hole U1464C (18°03.9244′S, 118°37.8942′E) was started at 0940 h on 20 September. After drilling without coring 308.0 m, the center bit was pulled. A nonmagnetic RCB core barrel was dressed, dropped, and coring began with recovery of Core 2R from 308.0 m DSF. We recovered Cores 3R through 56R to 840.0 m DSF by 1435 h on 22 September. A total of 55 RCB cores were taken over a 532.0 m interval with a total recovery of 94.03 m of core. Total recovery for Hole U1464C was 17.7%.

The hole was circulated with high-viscosity mud to clean the hole of cuttings before the RCB coring bit was released to the bottom of the hole. After releasing the bit, the drill string was pulled up to 800.3 m DSF and heavy mud was pumped to prevent backflow from the drill string. The drill string was pulled up to 567.3 m DSF and the continued backflow from the hole became excessive, so the hole was circulated out and another two high-viscosity mud sweeps were pumped to clean the annulus. After cleaning the hole, the drill string was pulled back to 363.1 m DSF and the circulating head was installed. The upper 363.1 m of the hole was displaced with heavy mud, and the end of the pipe was set at 86.9 m DSF in preparation for logging after this upper part of the hole was displaced again with heavy mud. The triple combo tool string was assembled at 0015 h on 23 September and contained the following tools: magnetic susceptibility sonde, Hostile Environment Natural Gamma Ray Sonde, Hostile Environment Litho-Density Tool, Enhanced Digital Telemetry Cartridge, and logging equipment head-q tension. The tool string was deployed at 0115 h. After the tool string exited the drill pipe, the active heave compensator was turned on. A downlog was performed from just above seafloor to a bridge at 783.7 m WSF. The hole was logged up with the triple combo tool string to ~619.1 m WSF where the tool string became stuck. After trying to free the logging tools, we decided to strip in with drill pipe over the logging line in an attempt to recover the tool string while washing over the wireline. The tool string was eventually recovered after stripping over the wireline from 86.9 to 579 m DSF. The tools pulled up into the drill string with the pipe at 625.6 m DSF. The logging wireline was pulled up to the rig floor using T-bars until reaching the top of the drill string then secured in the tool rack. At 0030 h on 24 September, all logging tools were disassembled and the logging wireline was secured. No damage was found to any of the logging tools. However, while pulling the tool string from the hole, the drill pipe became stuck and was finally freed from the formation by using a combination of overpull, rotation, and pumping. The drill pipe was then pulled back to the rig floor by 0830 h on 24 September, ending Hole U1464C. The total time spent on Hole U1464C was 98.25 h (4.1 days).

Hole U1464D

After offsetting the vessel 20 m west of Hole U1464C, we prepared to begin coring Hole U1464D (18°03.9230′S, 118°37.8836′E) with the piston coring and XCB systems. A nonmagnetic APC core barrel was dressed, and Hole U1464D was started at 1400 h on 24 September. Based on the recovery of the mudline core (3.55 m), the seafloor depth was calculated to be 264.7 mbsl. We recovered Cores 356-U1464D-2H through 32H to 293.5 m DSF, at which depth APC refusal was reached. In situ formation temperature measurements with the advanced piston corer temperature tool (APCT-3) were taken on Cores 5H, 8H, 12H, 16H, 22H, and 28H with excellent results. The Icefield MI-5 orientation tool was removed after the last full APC core. After recovering Core 32H, the XCB system was deployed. Coring continued from 293.5 m DSF, and we recovered Cores 33X through 58X to 529.6 m DSF. We cored 293.5 m with the APC system and recovered 265.89 m of core, whereas the XCB system was used to core 236.1 m and recovered 34.85 m of core. Total recovery for Hole U1464D was 57%. After the completion of coring, the drill string was pulled back to the rig floor, which was then secured for transit. The seafloor positioning beacon was recovered at 1820 h on 26 September and Site U1464 ended. At 2100 h, the vessel was underway to Darwin. The total time spent on Hole U1464D was 60.50 h (2.5 days). The total time spent on Site U1464 was 185.25 h (7.7 days).

Transit to Darwin, Australia

At 2100 h on 26 September 2015, we were under way to Darwin, Australia. Expedition 356 ended at 1013 h on 30 September.

Lithostratigraphy

Lithostratigraphy of Site U1464 is divided into five lithostratigraphic units. The units and their boundaries are defined by changes in lithology (identified by visual core description and smear slide observations), physical properties, color reflectance (L*, a*, and b*), petrographic thin section analyses, and X-ray diffraction (XRD). The lithologic descriptions are based on sediments recovered from Hole U1464B (0.00–316.95 m core depth below seafloor [CSF-A]) for Units I–III and from Hole U1464C (308.00–832.90 m CSF-A) for Units IV and V. The holes were correlated based on drilling depth and the correlation of lithologic boundaries (Table **T3**; Figure **F4**). All thin section samples are listed in Table **T4** and XRD analyses are summarized in Table **T5**.

Unit I

Intervals: 356-U1464B-1H-1, 0 cm, through 6H-3, 90 cm; 356-U1464D-1H-1, 0 cm, through 6H-2, 0 cm
Depths: Hole U1464B = 0.00–44.10 m CSF-A (44.10 m thick); Hole U1464D = 0.00–43.00 m CSF-A (43.00 m thick)
Age: recent–Middle Pleistocene
Lithology: unlithified mudstone and skeletal grainstone with peloids
Core quality: slight to moderate drilling disturbance causing soupiness

Unit I consists of unlithified creamy-gray sediments with peloids in varying abundances, with the last occurrence of peloids defining the base of the unit. The sediments are mainly skeletal grainstone and mudstone with minor intervals of packstone and wackestone. The upper part (0–13.20 m CSF-A in Hole U1464B) is

Table T3. Lithostratigraphic unit summary, Site U1464. **Download table in .csv format.**

Lith. unit	Hole U1464B				Hole U1464C				Hole U1464D			
	Core, section, interval (cm)		Depth CSF-A (m)		Core, section, interval (cm)		Depth CSF-A (m)		Core, section, interval (cm)		Depth CSF-A (m)	
	Top	Bottom	Top	Bottom	Top	Bottom	Top	Bottom	Top	Bottom	Top	Bottom
	356-U1464B-	356-U1464B-			356-U1464C-	356-U1464C-			356-U1464D-	356-U1464D-		
I	1H-1, 0	6H-3, 90	0.00	44.10					1H-1, 0	6H-2, 0	0.00	43.00
II	6H-3, 90	16H-3, 0	44.10	138.20					6H-2, 0	16H-3, 89	43.00	140.39
III	16H-3, 0	34H-4, 66	138.20	308.86					16H-3, 89	34X-CC, 0	140.39	308.74
IV	34H-4, 66	35F-CC, 6	308.86	316.95	2R-1, 0	24R-1, 0	308.00	521.40	34X-CC, 0	58X-CC, 5	308.74	523.97
V					24R-1, 0	56R-1, 110	521.40	832.90				

Figure F4. Lithostratigraphic summary, Site U1464 (composite record from Holes U1464B and U1464C). L* and NGR: red = Hole U1464B, black = Hole U1464C. See Figures **F6** and **F7** in the Expedition 356 methods chapter (Gallagher et al., 2017a) for lithology, boundary, structure, and diagenesis keys. cps = counts per second.

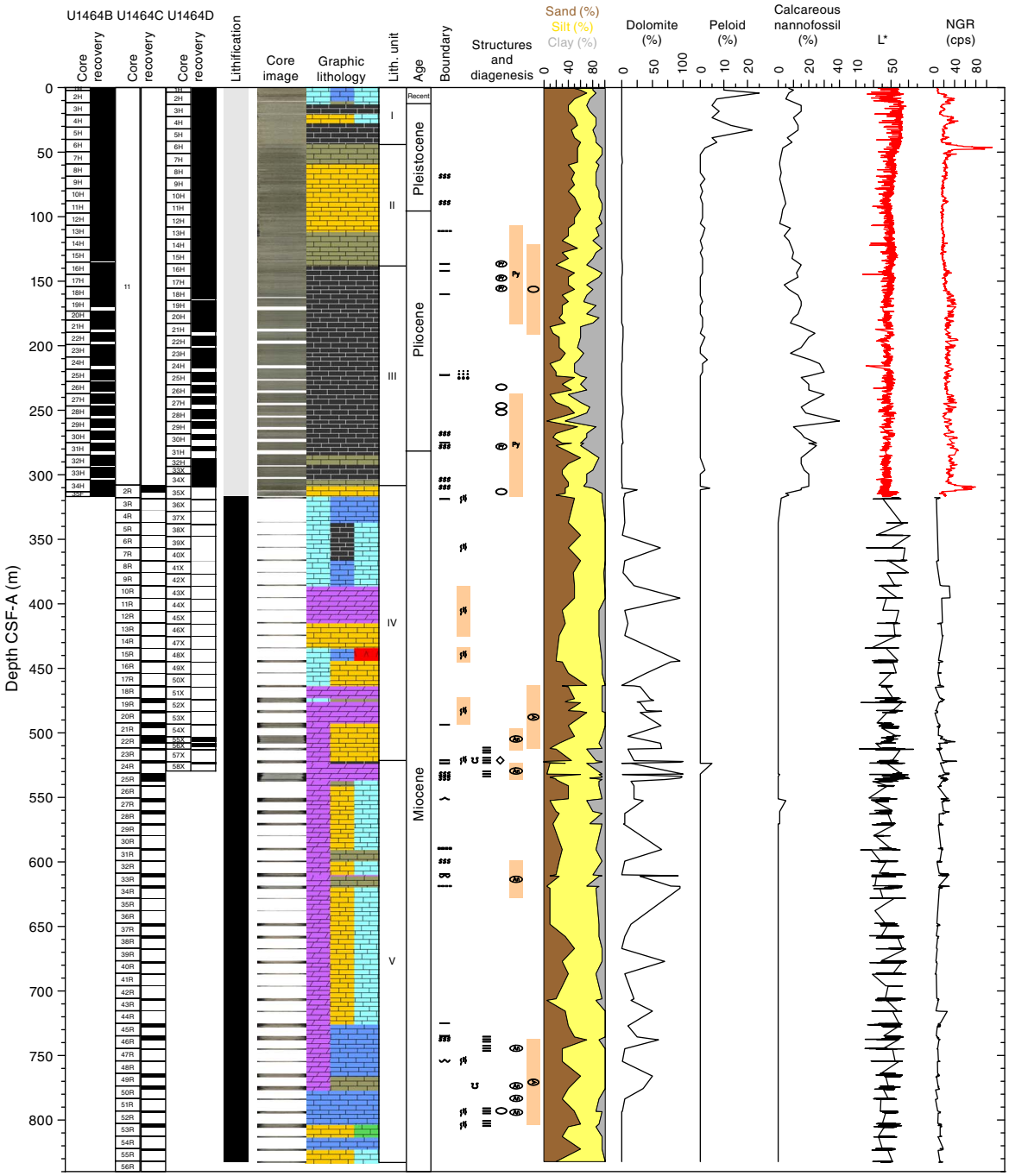

composed mainly of unlithified light brown skeletal grainstone containing fine to coarse sand–sized grains with occasional macrofossils, bioclasts, peloids, and glauconite grains. The middle of the unit (13.20–21.09 m CSF-A in Hole U1464B) consists of unlithified homogeneous cream mudstone overlying unlithified homogeneous creamy-gray wackestone with fine sand–sized grains and packstone with sand- to granule-sized grains (21.09–27.85 m CSF-A in Hole U1464B). Both lithologies have abundant foraminifers and some macrofossils (e.g., scaphopods, bivalves, and solitary corals). The lowest part of the unit (27.85–44.1 m CSF-A in Hole U1464B) is cream to creamy-gray mudstone containing very fine to fine sand–sized grains, common small benthic foraminifers, and occasional macrofossils (e.g., scaphopods, bivalves, and solitary corals).

Unit I has relatively high color reflectance L* and high calcium carbonate content (87–90 wt%) (Figure **F5**). Grain density and porosity gradually decrease through this unit, whereas natural gamma radiation (NGR) is highly variable with two peaks.

Smear slides

Unit I consists of bioclastic sands containing a diverse microfossil assemblage and common peloids and mica. The last occurrence of peloids (Figures **F6**, **F7A**) marks the base of the unit. The peloids are mostly coarse silt to fine sand sized, with rare larger peloids throughout the unit. Grains are generally bimodal with larger sand-sized microfossils in a fine silt– to clay-sized matrix containing common nannofossils (Figure **F6**). Well-preserved planktonic foraminifers and shell fragments dominate the assemblage with fewer benthic foraminifers. Echinoid spine fragments and ascidian and sponge spicules are minor components throughout the unit. Pristine pteropods and small (~300 µm) mollusk shells are common at the top of the unit but decrease sharply with depth. Fine sand–sized detrital glauconite is common throughout the unit, and authigenic glauconite is a rare accessory in some isolated samples, but glauconitization is absent. The generally low siliciclastic content is dominated by mica and quartz.

Table T4. Thin section samples, Site U1464. All thin sections are from working-half sections. **Download table in .csv format.**

Lith. unit	Core, section, interval (cm)	Top depth CSF-A (m)	Bottom depth CSF-A (m)
	356-U1464B-		
II	15H-2, 15–17	127.35	127.37
IV	35F-1, 3–5	313.23	313.25
	356-U1464C-		
IV	2R-2, 51–53	309.99	310.01
IV	3R-1, 43–48	318.13	318.18
IV	5R-1, 7–10	337.17	337.20
IV	11R-1, 19–20	395.49	395.50
IV	13R-1, 67–70	415.37	415.40
IV	14R-1, 40–43	424.80	424.83
IV	15R-CC, 8–9	434.18	434.19
IV	15R-CC, 32–33	434.42	434.43
IV	16R-2, 41–44	445.21	445.24
IV	18R-2, 17–20	464.07	464.10
IV	21R-2, 105–108	494.79	494.82
IV	23R-1, 70–73	512.40	512.43
V	24R-2, 49–54	523.14	523.19
V	25R-3, 127–132	534.69	534.74
V	28R-1, 0–2	560.20	560.22
V	28R-1, 59–60	560.79	560.81
V	28R-2, 69–71	562.38	562.40
V	43R-2, 77–81	707.47	707.51
V	55R-1, 72–75	822.82	822.85
V	56R-1, 75–78	832.55	832.58

Unit II

Intervals: 356-U1464B-6H-3, 90 cm, through 16H-3, 0 cm; 356-U1464D-6H-2, 0 cm, through 16H-3, 89 cm
Depths: Hole U1464B = 44.10–138.20 m CSF-A (94.10 m thick); Hole U1464D = 43.00–140.39 m CSF-A (97.39 m thick)
Age: Middle Pleistocene–early Pliocene
Lithology: unlithified homogeneous wackestone and packstone
Core quality: drilling disturbance consists of slight to moderate soupiness in upper parts of the unit and is rare in lower parts

The Unit I/II boundary is defined by the downhole change from mudstone to wackestone and by the loss of peloids as a common component. Unit II consists mainly of unlithified homogeneous wackestone that includes a packstone interval with relatively high glauconite abundance (Figure **F4**). The uppermost part of the unit (44.10–59.62 m CSF-A in Hole U1464B) is composed predominantly of greenish-gray wackestone containing fine to coarse sand–sized grains, abundant glauconite, common small benthic foraminifers, and sparse bioclasts (bivalves and echinoderms). The middle part of the unit (59.62–112.06 m CSF-A in Hole U1464B) is unlithified homogeneous greenish-gray packstone with fine sand–sized grains and includes occasional wackestone intervals. The packstone contains small benthic foraminifers and rare bioclasts (mainly bivalve, echinoderm, and scaphopod fragments). Bioturbation is slight throughout the middle section. The lower part of Unit II (112.06–138.20 m CSF-A in Hole U1464B) consists of unlithified homogeneous light greenish to greenish-gray wackestone with very fine to fine sand–sized grains and few macrofossils. Disseminated grains of pyrite are common with occasional pyrite nodules and celestite concretions.

Calcium carbonate (73–84 wt%) and quartz contents increase downhole in Unit II, whereas porosity decreases slightly (Figure **F5**). NGR is relatively stable and low (Figure **F4**).

Table T5. Semiquantitative XRD analysis of dominant mineral phases, Site U1464. LMC = low-Mg calcite, HMC = high-Mg calcite. $MgCO_3$ of dolomite was calculated based on the d-value of the [104] peak (Lumsden, 1979). **Download table in .csv format.**

Lith. unit	Core, section, interval (cm)	Depth CSF-A (m)	Clay mineral group	Relative (%)								Mg content (mol%)
				Celestite	Anhydrite	Quartz	Aragonite	LMC	HMC	Dolomite	Gypsum	
	356-U1464B-											
II	7H-3, 70	53.40	Illite	0	0	36	7	52	0	5	0	42
III	18H-3, 70	157.90	Kaolinite/Illite	3	0	24	6	62	0	5	0	43
III	19H-2, 77	165.97	Kaolinite/Illite	59	0	9	14	17	0	0	0	
III	26H-3, 70	231.40	Kaolinite/Illite	0	0	16	0	69	0	3	0	44

Figure F5. Summary of synthetized correlation of lithostratigraphy at Site U1464 with data from smear slides (quartz content and grain size), geochemistry (calcium carbonate), physical properties (MS, NGR, grain density, *P*-wave velocity, and porosity), and biostratigraphy. See Figure **F7** in the Expedition 356 methods chapter (Gallagher et al., 2017a) for lithology key. SHMSL = Section Half Multisensor Logger, MSP = point magnetic susceptibility.

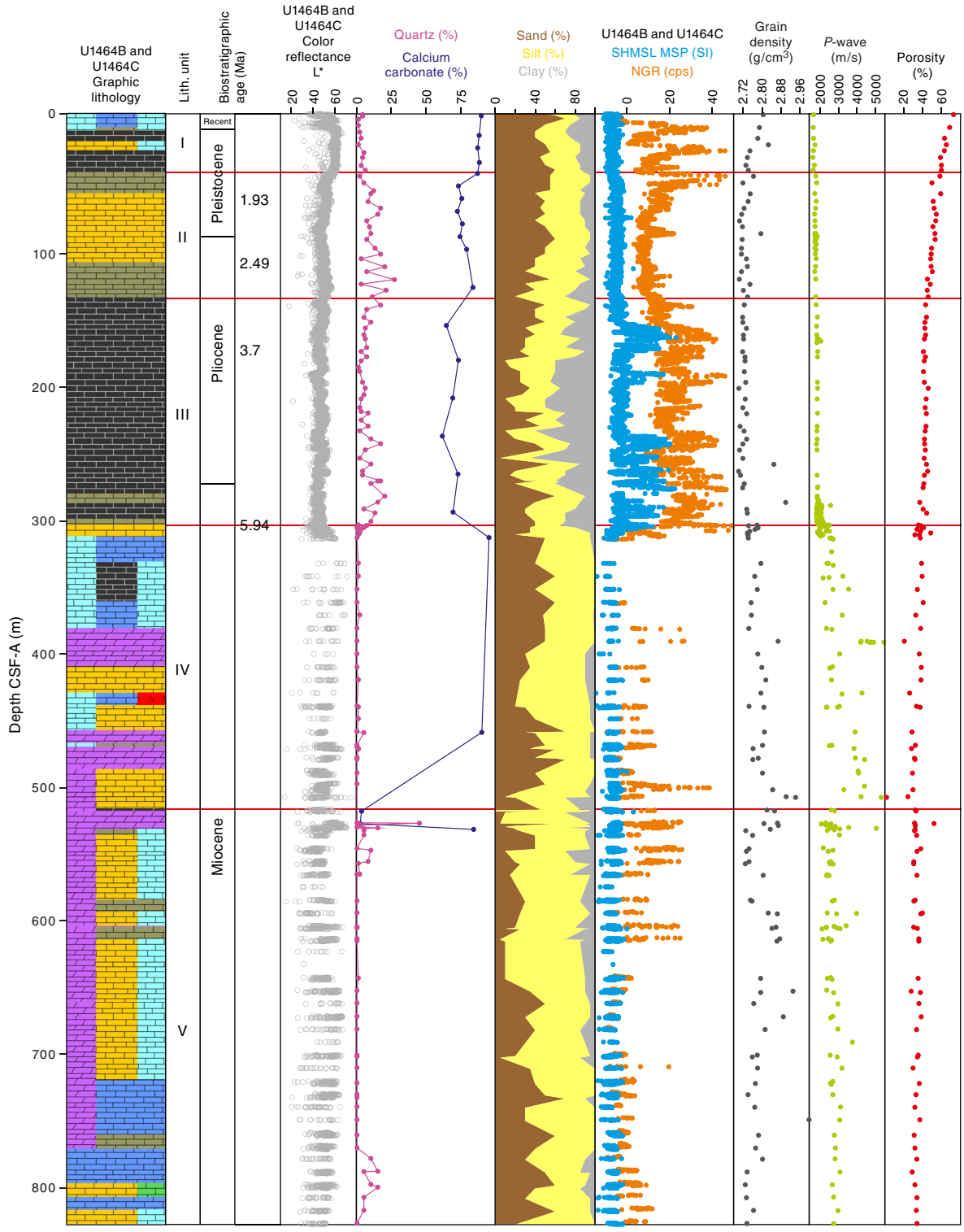

Smear slides

The top of Unit II is marked by a decrease in peloids and shell fragments with a concurrent increase in siliciclastic components, as well as planktonic and benthic foraminifers (Figure **F6**). Following the sharp increase in foraminifers at the top of the unit, abundance decreases continuously toward the base of Unit II. Shell and rare echinoderm spine fragments are rare throughout the unit (Figure **F7B**). Ascidian and sponge spicules are rare at the top of the unit and disappear completely in the lower half. Authigenic glauconite and glauconitization of microfossils are more abundant than in Unit I and co-occur with common fine sand– to silt-sized detrital glauconite grains. Despite glauconitization, overall microfossil preserva-

Figure F6. Smear slide summary, Holes U1464B and U1464C (composite record from Holes U1464B and U1464C). See Figure **F7** in the Expedition 356 methods chapter (Gallagher et al., 2017a) for lithology key.

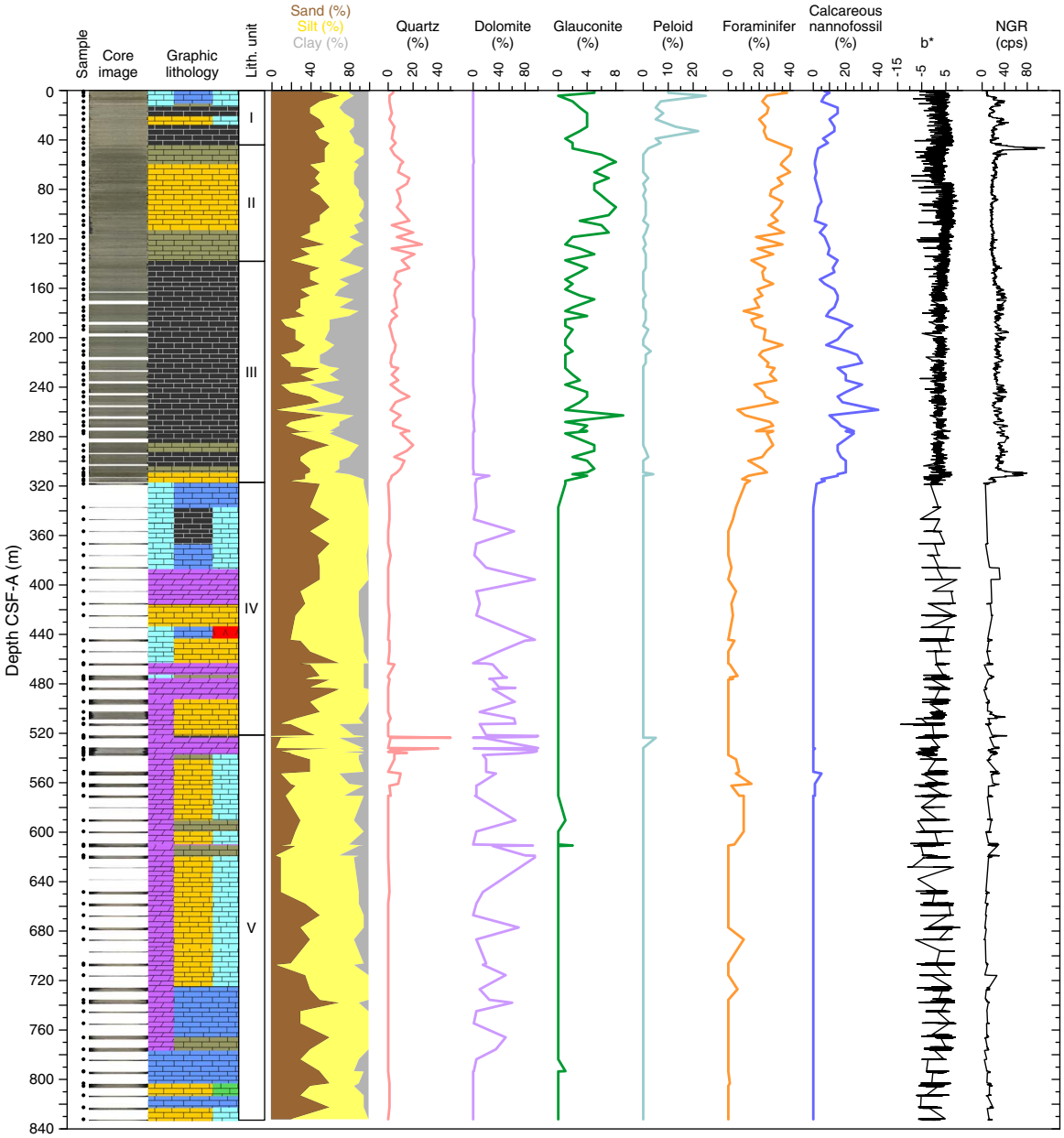

tion remains moderate to good with frequent preservation of aragonitic ultrastructures in shell fragments and only slight calcite overgrowth on foraminifers (Figure **F7B**). Siliciclastics at the top of Unit II are mainly common to abundant quartz with highly variable concentrations, particularly in the lower half of the unit (Figure **F6**). Feldspar and mica are minor components, with rare occurrences of heavy minerals (e.g., zircon and apatite). Grain sizes of siliciclastic components vary from silt to medium sand sized.

Thin sections

The only thin section from Unit II (Table **T4**; Figure **F8A**) is a foraminifer-rich packstone to grainstone with abundant benthic (e.g., *Amphistegina, Cibicidoides, Bolivina*, and *Textularia*) and common planktonic (*Globigerinoides*) foraminifers. Pore spaces are completely filled with celestite that forms large single crystals with grayish to bluish interference colors under cross-polarized light (XPL). Bivalve fragments and echinoderm fragments are rare. Glauconite is common, mainly in foraminiferal chambers. Angular silt-sized quartz grains are rare.

XRD

The only sample from Unit II is dominated by low-Mg calcite (52%) and quartz (36%) with minor amounts of aragonite (7%) and dolomite (5%) (Table **T5**). The only clay mineral present is illite. The Mg content of the dolomite is 42%.

Unit III

Intervals: 356-U1464B-16H-3, 0 cm, through 34H-4, 66 cm; 356-U1464D-16H-3, 89 cm, through 34X-CC, 0 cm

Figure F7. Representative smear slide photomicrographs for units, Site U1464. A. Unit I: well-preserved microfossils, including foraminifers (f), pteropods (pt), mollusk shell fragments (m), echinoderm fragments (e), sponge spicules (s), and common peloids (p) (356-U1464B-2H-2, 71 cm). B. Unit II: sediment rich in authigenic and detrital glauconite (arrows) with abundant microfossils, including planktonic and benthic foraminifers (f), mollusk shell fragments (m), and echinoid spine fragments (e), in a fine micritic matrix (7H-6, 71 cm). C. Unit III: moderately to well-preserved microfossils, including foraminifers (f) and mollusk shell fragments (m), in a fine micrite matrix (17H-6, 71 cm). D. Unit IV: large crystalline anhydrite (a) in a matrix of silt-sized anhydrite containing euhedral dolomite (black arrow); note accessory gypsum (white arrows) (356-U1464C-20R-1, 14 cm); XPL. E. Unit IV: dark layer composed of dolomite (white arrows), plant fragments (pl), common silt-sized quartz grains (q), framboidal pyrite (black arrows), rare benthic foraminifers (f), and common brown aggregates of organic matter (gray arrows) (25R-2, 51 cm). F. Unit V: altered foraminifers (f) and various unidentifiable bioclasts (b) in a coarse matrix with sparite (arrows) (53R-1, 71 cm).

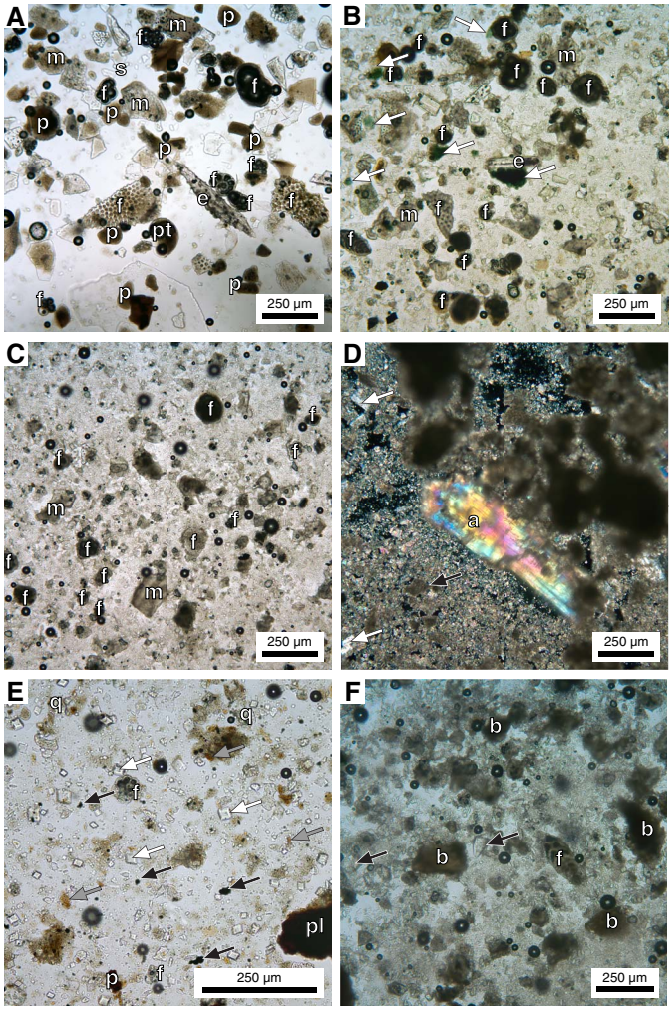

Figure F8. Thin section photomicrographs, Site U1464. A. Unit II: celestite-cemented foraminifer-rich packstone to grainstone with abundant LBFs (f) and common planktonic foraminifers (p); pore space is filled with large single crystals of celestite showing orthogonal cleavage and grayish to bluish interference colors (arrows) (356-U1464B-15H-2, 15–17 cm); XPL. B. Unit IV: parallel polarized image of foraminifer-rich packstone with small benthic foraminifers and LBFs (f) and echinoderm fragments (e) (35F-1, 3–5 cm). C. Unit IV: coral fragment (c) partly covered by laminae of encrusting algae (a); original coral skeleton completely dissolved except for an enigmatic part of exterior wall (arrow); before dissolution, pore space was filled with micrite that is partly recrystallized to sparite (356-U1464C-13R-1, 67–70 cm); XPL. D. Unit IV: dolomitized coral fragment (d) with dissolved parts of corals filled with celestite/gypsum (arrows) (356-U1464B-15R-CC, 32–33 cm); XPL. E. Unit IV: parallel polarized image of dolomitized packstone with recrystallized bioclasts, mainly benthic foraminifers (f), echinoderm fragments (e), and low amounts of disseminated pyrite (356-U1464C-18R-2, 17–20 cm). F. Unit V: skeletal packstone with abundant benthic foraminifers (f) and common echinoderm fragments (e); silt-sized quartz is a minor component and micritic matrix is partly dolomitized; some bioclasts overgrown with gypsum cement (arrows); remaining pore space filled with radial gypsum (g) (28R-2, 69–71 cm); XPL.

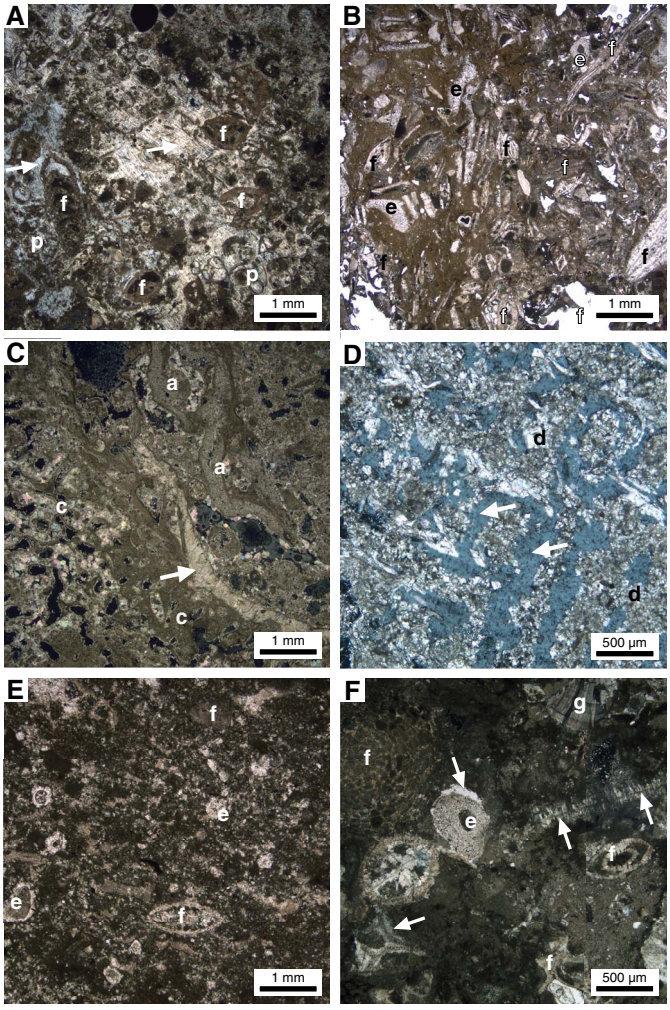

Depths: Hole U1464B = 138.20–308.86 m CSF-A (170.66 m thick);
Hole U1464D = 140.39–308.74 m CSF-A (168.35 m thick)
Age: early Pliocene–late Miocene
Lithology: unlithified mudstone
Core quality: drilling disturbance is rare, except for slight to complete mixing and biscuits in lower parts of the unit

The top of Unit III is marked by a transition from wackestone to mudstone and by an increase in calcareous nannofossils (visible in smear slides). The unit consists mainly of unlithified grayish-green to greenish-gray homogeneous mudstone with moderate bioturbation. Pyrite grains are disseminated sparsely but are often concentrated in burrows. Pyrite also forms nodules up to 3 cm in diameter, and celestite forms concretions as large as 2 cm. Bioclasts are very rare and mainly sand-sized fragments of bivalves, bryo-

zoans, and echinoid spines. Benthic foraminifers are concentrated in burrows. In the lowest part of the unit (284.83–316.95 m CSF-A in Hole U1464B), the mudstone grades into grayish-green wackestone with fine sand–sized grains and then into light gray packstones with medium sand–sized grains. Both lithologies contain small benthic foraminifers.

Unit III has fluctuating calcium carbonate values between 62 and 73 wt% (see **Geochemistry**) and highly variable magnetic susceptibility (MS) and NGR (see **Physical properties**).

Smear slides

Unit III is characterized by decreasing sand-sized siliciclastic contents and increasing clay-sized sediment (Figure **F6**). The microfossil assemblage is similar to those in Units I and II. The most abundant component consists of planktonic foraminifers with common benthic foraminifers and shell fragments (Figure **F7C**). Although abundances of these three components are variable, there are no clear trends in abundance through the unit. In contrast, nannofossils increase markedly to become a major component toward the middle of Unit III, coinciding with an overall increase in fine silt– and clay-sized components. Other bioclasts include fragments of echinoderm spines and occasional sponge spicules. Glauconitization of fossils is less abundant than in Unit II but remains common in the lower part of Unit III. Authigenic glauconite exhibits a similar trend, whereas detrital glauconite is present in only a few samples, where it is also rare.

XRD

Three XRD samples were analyzed from Unit III (Table **T5**). Two samples from the matrix sediment average 66% low-Mg calcite, 20% quartz, and 4% dolomite; one sample also has 6% aragonite and 3% celestite. The Mg content of the dolomite is 44%. The third sample, from a concretion, consists mainly of celestite (59%) with low-Mg calcite (17%), aragonite (14%), and quartz (9%) as minor components.

Unit IV

Intervals: 356-U1464B-34H-4, 66 cm, through 35F-CC, 6 cm; 356-U1464C-2R-1, 0 cm, through 24R-1, 0 cm; 356-U1464D-34X-CC, 0 cm, through 58X-CC, 5 cm
Depths: Hole U1464B = 308.86–316.95 m CSF-A (8.09 m thick); Hole U1464C = 308.00–521.40 m CSF-A (213.40 m thick); Hole U1464D = 308.74–523.97 m CSF-A (215.23 m thick)
Age: late Miocene
Lithology: lithified dolomitic packstone, grainstone, and dolostone with gypsum and anhydrite nodules
Core quality: moderate drilling disturbance as fragmentation

Unit IV is marked by a transition from wackestone to packstone associated with the first occurrence of dolomite in Holes U1464B and U1464C. The unit consists of three main intervals of dolomitic limestone separated by two intervals of skeletal limestones. The dolomitic limestones include mudstone, wackestone, packstone, and one dolostone interval, and the skeletal limestones include wackestone, packstone, and grainstone. Gypsum nodules are common in the dolomitic intervals and commonly co-occur with anhydrite nodules in the lower 46 m of the unit. Solution cavities and moldic porosity are also common, especially in the skeletal limestones. Macrofossils are present and diverse in both lithologies, often occurring as molds, and include benthic foraminifers, bivalve and gastropod fragments, scaphopods, bryozoans, echinoid spines, and sand dollars. Bioclasts include many organisms typical of shallow habitats, such as larger benthic foraminifers (e.g., *Cycloclypeus*), some zooxanthellate corals (*Porites, Acropora, Montipora*, and Faviidae), and crustose coralline algae. Fossils often occur as molds and some are replaced with gypsum and/or dolomite (Figure **F9**). Bioturbation is common in the upper half of the unit, and burrows often contain concentrations of benthic foraminifers and glauconite grains or may be filled with gypsum or anhydrite. Diagenetic features, including chickenwire anhydrite and replacement of macrofossils by gypsum or dolomite, increase with depth in the unit.

Figure F9. Unit IV macrofossil preservation, Hole U1464C. A. Branching coral mold (14R-1A, 13–19 cm). B. Solitary and branching corals with gypsum recrystallization (17R-CC, 6–12 cm). C. Massive coral with gypsum recrystallization (15R-CC, 6–10 cm). D. Bioclasts (bivalve, gastropod, echinoderm, and branching coral) with recrystallization and dolomitization (19R-3, 19–30 cm).

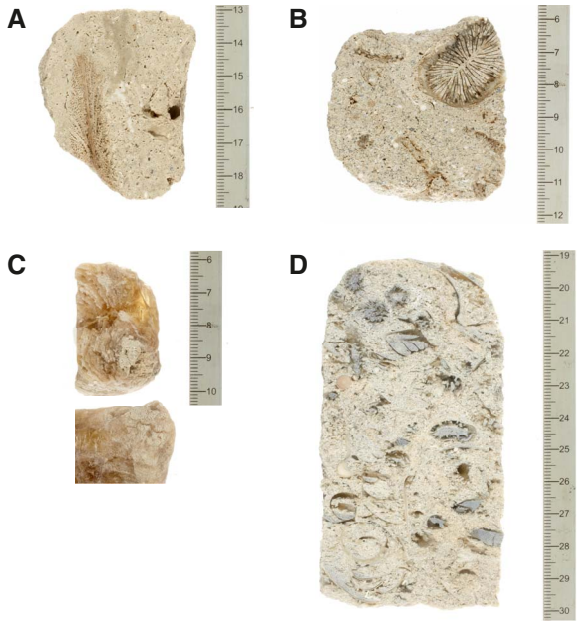

Although this unit has only two values for calcium carbonate content, both are very high (95.5% at 318 m CSF-A and 90.3% at 464 m CSF-A). Unit IV has relatively high but variable grain density and *P*-wave velocity (see **Physical properties**). Because of low recovery, MS and NGR data are limited, but overall values are low (Figure **F5**).

Smear slides

Because sediments in Unit IV were fully lithified, smear slides were mainly prepared using a spatula. Although this method can skew data on both fossil content and lithology, smear slides from this interval remain useful for characterizing the mineral composition of the cement and for distinguishing gypsum and anhydrite nodules. Euhedral to subhedral dolomite and dolomitized intervals occur throughout Unit IV. Siliciclastic material is absent to rare with occasional samples containing rare quartz. Microfossil abundance decreases sharply below the Unit III/IV boundary, and planktonic foraminifers and nannofossils are absent below the uppermost part of Unit IV (Figure **F6**). Most nondolomitized samples contain poorly preserved benthic foraminifers and often heavily recrystallized shell fragments (Figure **F7D**). Anhydrite and gypsum are common components of the matrix in samples taken close to anhydrite nodules.

Thin sections

Twelve thin sections were prepared for Unit IV (Table **T4**; Figure **F8B–F8D**). Skeletal packstones with abundant small benthic foraminifers and large benthic foraminifers (LBFs) are common in the upper part of the unit, with dolomitized limestones containing gypsum-replaced corals. The middle and lower parts of the unit are mainly dolomitized skeletal packstones.

Small benthic foraminifers and LBFs (e.g., *Amphistegina, Lepidocyclina*, and *Cibicidoides*) are common in the upper skeletal packstones, along with abundant sand-sized bivalve and echinoderm fragments. Planktonic foraminifers are rare to absent. The skeletal fragments are cemented by sparitic calcite in the upper part, and gypsum fills pores in the lower parts where the matrix is partially dolomitized. Glauconite and angular silt-sized quartz grains are rare (<3%).

Skeletal packstone containing coral fragments and wavy laminae of encrusting algae are abundant in the middle of Unit IV. Most coral skeletons are largely dissolved, dolomitized, or replaced with gypsum, although rare intact fragments of original coral remain. Sediments containing corals are skeletal packstones with abundant LBFs and scarce fragments of coralline algae. The micritic matrix is partly dolomitized and pore space is filled with gypsum crystals.

The lower part of Unit IV transitions from skeletal packstone to strongly dolomitized skeletal packstone. Small benthic foraminifers and LBFs (e.g., *Flosculinella* and *Sorites*) are dominant bioclastic components. Planktonic foraminifers and fragments of echinoderm, coralline algae, and coral skeletons are rare. Rare glauconite and silt-sized angular quartz grains are disseminated throughout the interval.

Unit V

Interval: 356-U1464C-24R-1, 0 cm, through 56R-1, 110 cm
Depth: Hole U1464C = 521.40–832.90 m CSF-A (311.50 m thick)
Age: late–middle Miocene
Lithology: lithified dolomitic limestones and dolostone with gypsum and anhydrite nodules
Core quality: moderate to severe drilling disturbance causing fragmentation

The top of Unit V is defined by the first occurrence of sediments that contain very well preserved features, such as load casts, ball-and-pillow, and parallel laminations, and are interpreted as a littoral facies. The unit consists primarily of dolomitic limestones (mudstone, wackestone, packstone, and grainstone) and dolostone. The uppermost part of the unit (521.40–619.23 m CSF-A in Hole U1464C) consists mainly of lithified light brown to brown and light gray to gray dolomitic wackestone, packstone, grainstone, and dolostone. Mottling and bioturbation are common in the light greenish-gray dolostone. There are also three thin (<10 cm) layers consisting of dark brown to black mud overlying partially lithified light greenish-gray to cream mudstone. Anhydrite is present and often abundant throughout the upper part as nodules (≤10 cm × 5 cm) that either displaced the sediment as they grew or appear to be infilling burrows. The nodules often have chickenwire textures. Other dolostone intervals have moldic porosity and solution cavities and/or have been filled with translucent to transparent brown material (likely gypsum). Bioclasts include fragments of bivalves, gastropods, echinoid spines, and bryozoans. Benthic foraminifers are common, including large (>3 cm) *Cycloclypeus*.

The middle part of Unit V (619.23–775.08 m CSF-A in Hole U1464C) is composed of lithified light brown dolomitic wackestone, packstone, and grainstone with intervals of largely unidentifiable skeletal limestone. The grainstone generally has very fine sand–sized grains with layers of coarse sand–sized to granule-sized grains. Many grains are green/black and appear to be glauconitized bioclasts or authigenic glauconite. Common fossils in these layers include benthic foraminifers, bryozoan fragments, and echinoid spines. Medium-sized (1–5 cm) burrows infilled with brown dolomite or gypsum are common. Moldic porosity is less common than in the upper interval, whereas anhydrite nodules are smaller and sparse.

The lowest interval of Unit V (775.08–832.9 m CSF-A in Hole U1464C) transitions from dolomitic to more calcite-rich lithologies. It is composed of lithified light greenish gray, light brown, and gray wackestones, packstones, and grainstones with increasingly coarser sand-sized grains and glauconite. Macrofossils initially are abundant and include small benthic foraminifers, LBFs (mainly *Cycloclypeus*), and bivalves. Overall fossil abundance decreases toward the base of the unit, except for bryozoans, which increase in abundance and become the dominant macrofossil in the lowermost 10 m.

Unit V has low and variable MS and NGR values and relatively high and variable grain density (Figure **F5**). The unit also has lower and less variable *P*-wave velocities than Unit IV (see **Physical properties**) and stable porosity values.

Smear slides

The fine sediment is similar to that in Unit IV. Repeated heavily dolomitized intervals become less frequent toward the base of the unit, where they are replaced by bioclast-rich sediment deeper than 738 m CSF-A. Microfossil abundances, especially poorly preserved shell fragments, increase in the lower half of the unit associated with bioclastic grainstones and packstones with a coarse sparitic matrix. In the lowermost part of Unit V, microfossil preservation increases again with moderately well preserved benthic foraminifers (Figure **F7E**). Anhydrite and gypsum are accessories in many samples.

Two thin laminated organic-rich layers (Samples 356-U1464C-24R-CC, 23 cm, and 25R-2, 23 cm) have high concentrations of disseminated organic particles that coat angular to subangular fine sand– to silt-sized gypsum and rare quartz grains and also coat the abundant framboidal pyrite. Larger organic particles within these layers include unidentified cystlike structures and fibrous aggregates. Spot samples from several thinner dark brown to black laminae in Cores 27R and 29R contain fine crystalline euhedral dolomite with dark brown fibrous organic matter and large amounts of disseminated organic matter coating silt-sized quartz and gypsum grains (Figure **F7F**).

Thin sections

Eight thin sections were prepared for Unit V (Table **T4**; Figure **F8**). The upper part is dolomitized skeletal packstone composed mainly of small benthic foraminifers with scarce silt-sized angular quartz grains. Anhydrite replacement is common, and anhydrite veins and scattered patches of gypsum are abundant. The lower part of Unit V consists of skeletal packstone to grainstone with abundant LBFs (e.g., *Operculina, Lepidocyclina, Quinqueloculina,* and agglutinated foraminifers). Planktonic foraminifers and fragments of echinoderms, bivalves, corals, and red algae are rare. Angular silt-sized quartz grains are present but rare. Grains are usually cemented with sparitic calcite cement and infrequently with gypsum. There is occasional iron oxide staining.

Biostratigraphy and micropaleontology

Core catcher (CC) samples from Site U1464 were processed at 20 m resolution. Nannofossil analyses were done at 10 m resolution in selected intervals to better constrain biostratigraphic datums between Holes U1464B, U1464C, and U1464D, and extra benthic foraminiferal samples were taken from selected intervals when specific assemblages were absent from core catcher samples.

Site U1464 yielded a complete stratigraphic succession from the early Pleistocene to middle Miocene, with common to abundant calcareous nannofossils in the late Miocene–Pleistocene section and (very) rare to few in the middle Miocene section. Calcareous nannofossil preservation was moderate to good throughout the section. (Figure **F10**). The Pliocene/Pleistocene boundary (2.58 Ma; within Biozone NN16) is between 97.42 and 108.29 m CSF-A, and the Miocene/Pliocene boundary (5.33 Ma; within Biozone NN12) is between 228.4 and 293.15 m CSF-A. Planktonic foraminiferal abundance and preservation at Site U1464 was moderate to good for the Pliocene–Pleistocene section with common to abundant planktonic foraminifers between 2.26 and 293.2 m CSF-A. Biostratigraphic marker species were identified for the Middle Pleistocene (0.61 Ma; top of *Globorotalia tosaensis*) at 11.51 m CSF-A, the Pliocene/Pleistocene boundary below the top of *Globorotalia limbata* (2.39 Ma; 88.17 m CSF-A), *Dentoglobigerina altispira* (3.47 Ma; 126.3 m CSF-A) for the middle Pliocene, and *Sphaeroidinellopsis kochi* (top at 4.53 Ma; 272.57 m CSF-A) for the early Pliocene. An extended interval that was barren, or contained heavily recrystallized foraminifers and very rare nannofossils, occurs deeper than 347.08 m CSF-A to the bottom of Hole U1464C (832.8 m CSF-A) and corresponds to the barren interval from 328.52 m CSF-A to the bottom of Hole

Figure F10. Nannofossil preservation (1 = poor [P], 2 = moderate, 3 = good [G], 4 = very good) and abundance (0 = barren [B], 1 = rare, 2 = few, 3 = common, 4 = abundant, 5 = dominant [D]) data, Holes U1464B–U1464D. See **Biostratigraphy and micropaleontology** in the Expedition 356 methods chapter (Gallagher et al., 2017a) for preservation and abundance definitions. Biozonation scheme is that of Martini (1971), see Figure **F11** for details on biostratigraphic datums.

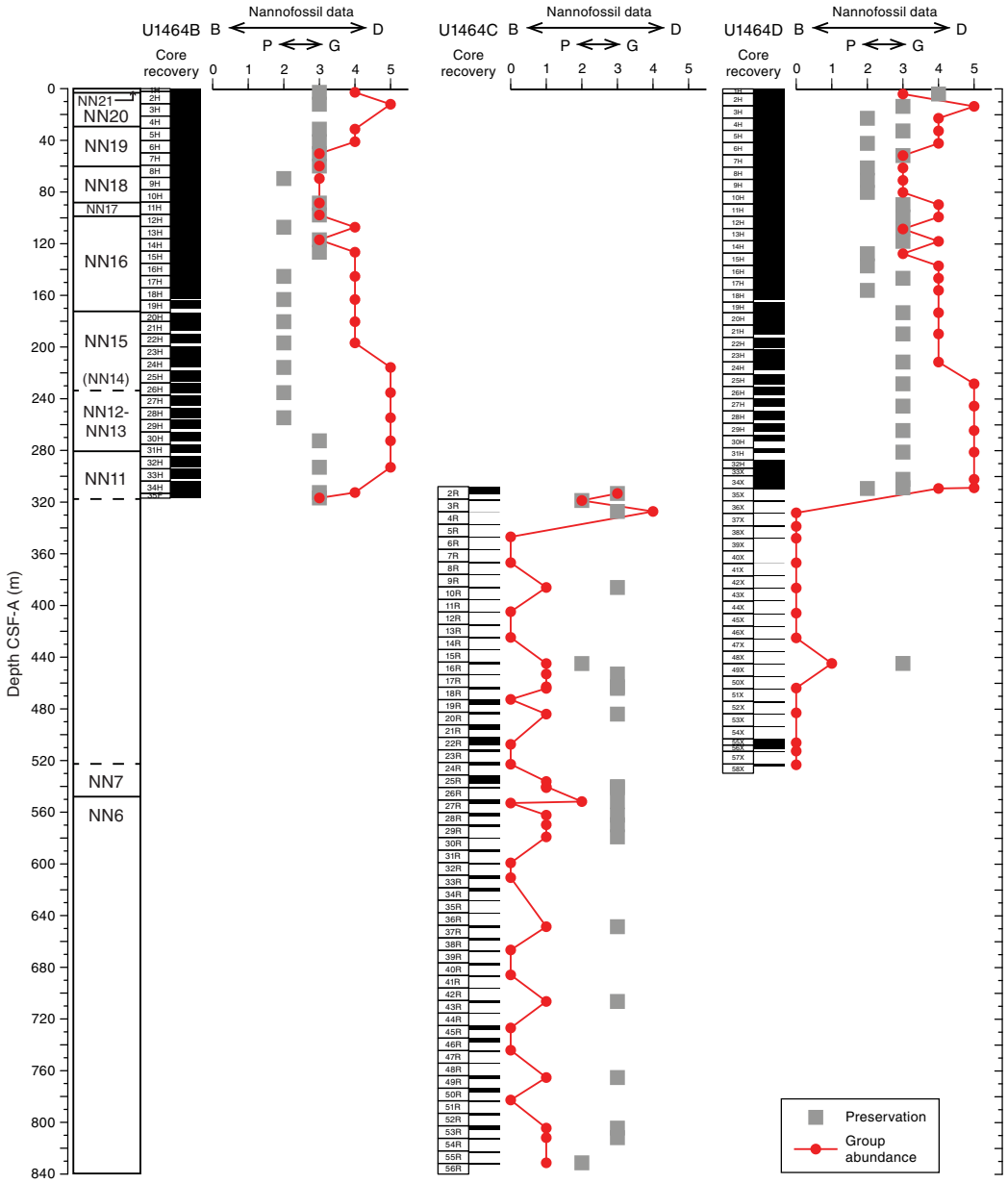

U1464D (523.97 m CSF-A). The final biostratigraphic datum suggests the material in Section 356-U1464C-43R-2 (707.57 m CSF-A) is older than 12.8 Ma (top of *Nephrolepidina ferreroi* TF1–2; Renema, 2007; Marshall et al., 2015).

Samples from Site U1464 contain between 6% and 100% benthic foraminifers, with *Cibicidoides* spp. as the most common taxa. Four assemblages can be identified based on the abundance of *Textularia* spp. (Assemblage 1); *Lenticulina* spp., *Clavulina subangularis, Neoeponides* spp., and *Pseudorotalia* spp. (Assemblage 2); *Amphistegina* spp., *Elphidium* spp., and *Operculina* spp. (Assemblage 3); and *Cibicidoides* spp. (Assemblage 4). One to 43 species were present in the samples, and the assemblages suggest paleodepths that start moderately deep (inner to outer shelf: Assemblage 1) and then rapidly become deeper (outer shelf to upper bathyal: Assemblage 2) until around 300–310 m CSF-A. At this horizon, the paleodepth shallows (inner to middle shelf: Assemblage 3) and then deepens again (inner to outer shelf: Assemblage 4). Preservation was affected by fragmentation, abrasion, encrustation, and infilling and varied from very good to poor throughout the site but was most frequently good for Assemblages 1 and 2 and poor for Assemblages 3 and 4.

Calcareous nannofossils

A total of 101 smear slides were examined for biostratigraphic marker species and common taxa. Calcareous nannofossils recovered at Site U1464 were common to very abundant with moderate to good preservation in samples from the late Miocene–Pleistocene section in Holes U1464B–U1464D and were (very) rare to few with moderate to good preservation in samples from the middle Miocene section in Holes U1464C and U1464D (Table **T6**; Figures **F10**, **F11**).

Pleistocene

Samples 356-U1464B-1H-CC (2.26 m CSF-A) and 356-U1464D-1H-CC (3.55 m CSF-A) contain common *Emiliania huxleyi* (Figure **F12A**) and are of latest Pleistocene age (<0.29 Ma; Biozone NN21). The top of *Pseudoemiliania lacunosa* (Figure **F12B**), which defines the Biozone NN19/NN20 boundary (0.44 Ma), is present in Samples 356-U1464B-4H-CC (30.82 m CSF-A) and 356-U1464D-4H-CC (32.21 m CSF-A). The top occurrence of *Calcidiscus macintyrei* (1.6 Ma; Figure **F12C**) in Samples 356-U1464B-6H-CC (49.82 m CSF-A) and 356-U1464D-6H-CC (51.33 m CSF-A) indicates the basal part of Biozone NN19. The top of *Discoaster brouweri*, recorded in Samples 356-U1464B-7H-CC (59.46 m CSF-A) and 356-U1464D-7H-CC (60.89 m CSF-A), represents the upper boundary of Biozone NN18 (1.93 Ma; Figure **F12D**). The Biozone NN18/NN17 boundary (2.39 Ma) is defined by the top occurrence of *Discoaster pentaradiatus* (Figure **F12E**) in Samples 356-U1464B-10H-CC (88.17 m CSF-A) and 356-U1464D-10H-CC (89.4 m CSF-A).

The Pleistocene assemblages are characterized by different (size defined) morphotypes of *Gephyrocapsa* spp. (Figure **F12F**), *P. lacunosa*, and *Reticulofenestra* spp. Small placoliths (<3 µm) are common to abundant in most samples and are dominated by small *Gephyrocapsa*. Other common taxa include *Calcidiscus leptoporus, Umbilicosphaera sibogae* (Figure **F12G**), *Syracosphaera pulchra, Pontosphaera japonica*, and *Helicosphaera* spp. (Table **T6**).

Table T6. Calcareous nannofossil abundance and range charts, Site U1464. **Download table in .csv format.**

Pliocene

The top of Biozone NN16, which includes the Pliocene/Pleistocene boundary, is marked by the presence of *Discoaster surculus* (2.49 Ma; Figure **F12H**) at 97.42 m CSF-A in Hole U1464B (Sample 11H-CC) and 108.29 m CSF-A in Hole U1464D (Sample 12H-CC). The top occurrence of *Discoaster tamalis* (2.8 Ma, within Biozone NN16; Figure **F12I**) is present in Sample 356-U1464B-14H-CC (126.3 m CSF-A) but was not observed in core catcher samples from Hole U1464D. The top of *Sphenolithus* spp. (3.54 Ma; Figure **F12J**), within the basal part of Biozone NN16, is placed at 163 m CSF-A in Hole U1464B (Sample 18H-6) and 173.23 m CSF-A in Hole U1464D (Sample 19H-6). The NN16/NN15 boundary (3.7 Ma) is defined by the top occurrence of *Reticulofenestra pseudoumbilicus* (Figure **F12K**) in Sample 356-U1464B-20H-CC (180.2 m CSF-A) and Section 356-U1464D-19H-6 (173.23 m CSF-A). Reworked early Pliocene taxa (e.g., *R. pseudoumbilicus* and *Sphenolithus* spp.) are rare to few between ~60 and 150 m CSF-A (Samples 356-U1464B-7H-CC through 16H-CC and 356-U1464D-7H-CC through 17H-CC).

The Pliocene nannofossil assemblages mainly consist of different (size defined) morphotypes of *Reticulofenestra* spp. and *P. lacunosa*. Small placoliths (2–3 and 3–5 µm) are common to very abundant in most samples and dominated by *Reticulofenestra minuta*. Other typical contributors to the assemblage include rare *Discoaster* spp. (Figure **F12L**), *Sphenolithus* spp., *Calcidiscus* spp., *Helicosphaera carteri* (Figure **F12M**), *Pontosphaera* spp., *Umbilicosphaera* spp., *Scyphosphaera* spp. (Figure **F12N**), and *S. pulchra* (Table **T6**).

Middle–late Miocene (barren and very rare nannofossils)

The Miocene/Pliocene boundary falls within Biozone NN12, which was difficult to constrain because of the absence of the marker species (e.g., *Ceratolithus* spp. and *Amaurolithus* spp.), and is tentatively placed between 235.25 (base of *P. lacunosa*, 4.2 Ma; Sample 356-U1464B-26H-CC) and 293.15 m CSF-A (>5.94 Ma; presence of *Nicklithus amplificus* in Section 32H-6; Figure **F12O**) in Hole U1464B and between 228.4 (base of *P. lacunosa*, 4.2 Ma; Sample 356-U1464D-25H-CC) and 281.39 m CSF-A (>5.59 Ma; top occurrence of *Discoaster quinqueramus* in Sample 31H-CC, Figure **F12P**) in Hole U1464D. The late Miocene marker species *Reticulofenestra rotaria* (short range within Biozone NN11B, >6.252 Ma; Young, 1998; Figure **F12Q**) and *N. amplificus* (>5.94 Ma) were observed at the bottom of Hole U1464B (316.95 m CSF-A) and above the barren intervals in Holes U1464C and U1464D.

The marker species *Cyclicargolithus floridanus* (>11.85 Ma, top occurrence indicates the basal part of Biozone NN7; Figure **F12R**) in Section 356-U1464C-26R-1 (541.67 m CSF-A) and *Coronocyclus nitescens* (>12.12 Ma, top occurrence indicates the upper part of Biozone NN6; Figure **F12S**) in Sample 27R-2, 51 cm (552.5 m CSF-A), were found within the otherwise barren intervals in Hole U1464C. Therefore, the Biozone NN7/NN6 boundary is tentatively placed between 541.67 and 552.5 m CSF-A. One specimen of *C. macintyrei* is present in Section 356-U1464B-30R-1 (579.91 m CSF-A), indicating a maximum age of 13.36 Ma (Biozone NN6). The downhole extension of Biozone NN6 within Hole U1464C is not further constrained, as calcareous nannofossil marker taxa are absent deeper than ~600 m CSF-A.

The Miocene "assemblages" were rare to abundant small-sized (2–5 µm) *Reticulofenestra* spp. with rare *R. pseudoumbilicus* (<7 and >7 µm) (Figure **F12T**), *C. floridanus, Coccolithus pelagicus* (Figure

Figure F11. Depth ranges of middle Miocene to Late Pleistocene calcareous nannofossil age markers, as recorded between Holes U1464B, U1464C, and U1464D. Green bars = age-depth tie points and robust correlations between holes. Pliocene/Pleistocene boundary (2.58 Ma) lies within Biozone NN16, approximated by the top of *Discoaster surculus* (2.49 Ma). Early Pliocene/late Pliocene boundary lies between the top of *Sphenolithus* spp. (3.54 Ma) and top of *Reticulofenestra pseudoumbilicus* (3.7 Ma). The base of *Pseudoemiliania lacunosa* (4.2 Ma) is used to denote the base of early Pliocene Biozone NN14. Miocene/Pliocene boundary (5.33 Ma) lies within Biozone NN12 but is difficult to constrain because of the lack of marker species. The top of *Discoaster quinqueramus* indicates late Miocene (Messinian) age (Biozone NN11). Occurrences of *Cyclicargolithus floridanus* and *Coronocyclus nitescens* indicate middle Miocene age (Biozones NN7–NN6).

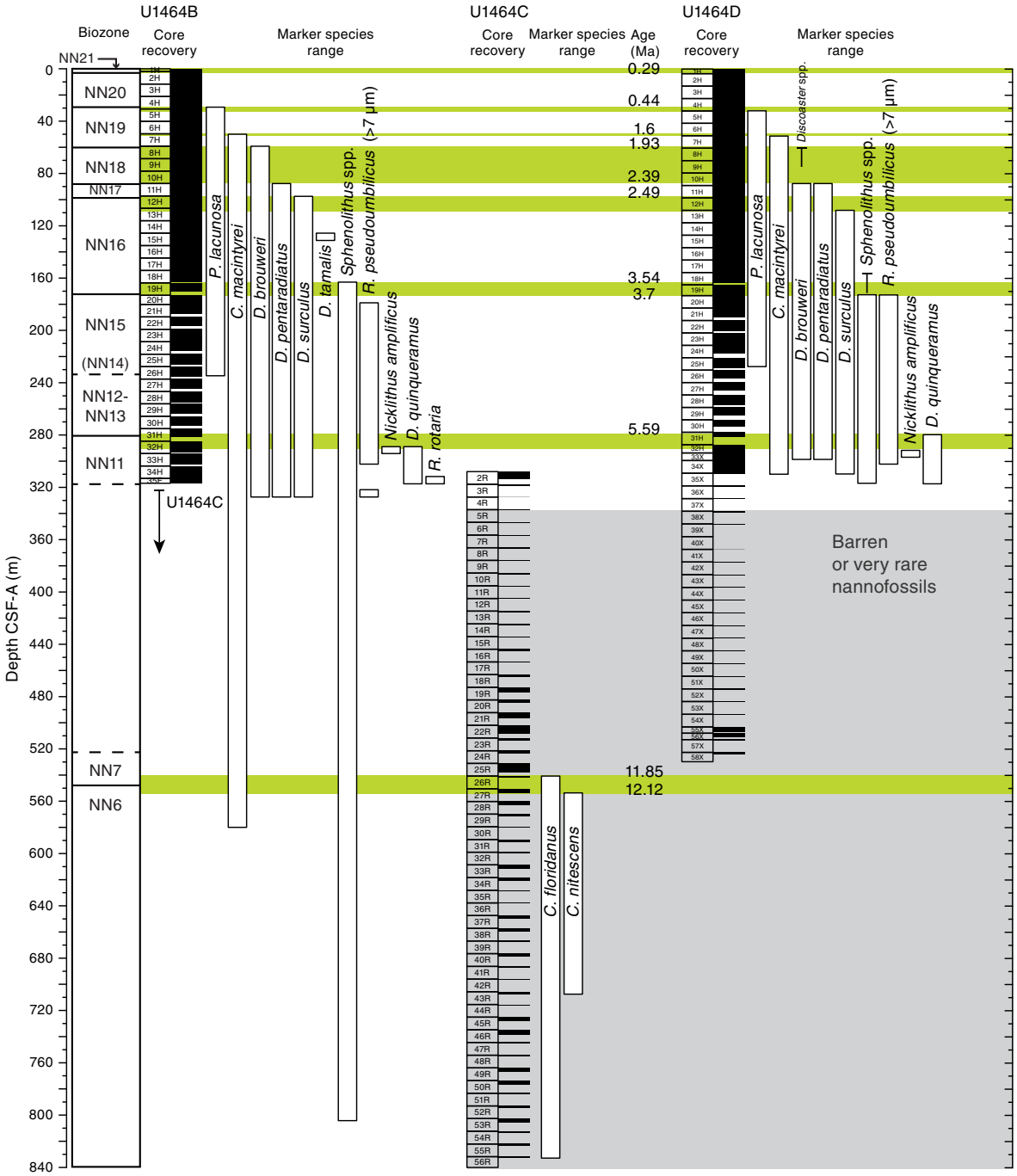

F12U), *H. carteri, Pontosphaera* spp., *Scyphosphaera apsteinii*, and *Umbilicosphaera* spp. (Table **T6**).

Planktonic foraminifers

A total of 19 samples were examined from Hole U1464B, 27 from Hole U1464C, and 37 from Hole U1464D. Planktonic foraminifers recovered at Site U1464 represent a stratigraphic succession from the early Pliocene to recent (Table **T7**). Preservation ranged from moderate to very good in Holes U1464B and U1464D (to ~293.2 m CSF-A and 302.49 m CSF-A, respectively), encompassed 8–17 species per sample (Table **T8**; Figure **F13**), and up to 80% planktonic foraminifers relative to benthic foraminifers. From

Figure F12. Plane-polarized light (PPL) photomicrographs of calcareous nannofossils, Site U1464. A. *Emiliania huxleyi*. B. *Pseudoemiliania lacunosa*. C. *Calcidiscus macintyrei*. D. *Discoaster brouweri*. E. *Discoaster pentaradiatus*. F. *Gephyrocapsa* spp. G. *Umbilicosphaera sibogae*. H. *Discoaster surculus*. I. *Discoaster tamalis*. J. *Sphenolithus* spp. K. *Reticulofenestra pseudoumbilicus*. L. *Discoaster* spp. M. *Helicosphaera carteri*. N. *Scyphosphaera apsteinii*. O. *Nicklithus amplificus*. P. *Discoaster quinqueramus*. Q. *Reticulofenestra rotaria*. R. *Cyclicargolithus floridanus*. S. *Coronocyclus nitescens*. T. *Reticulofenestra pseudoumbilicus*. U. *Coccolithus pelagicus*.

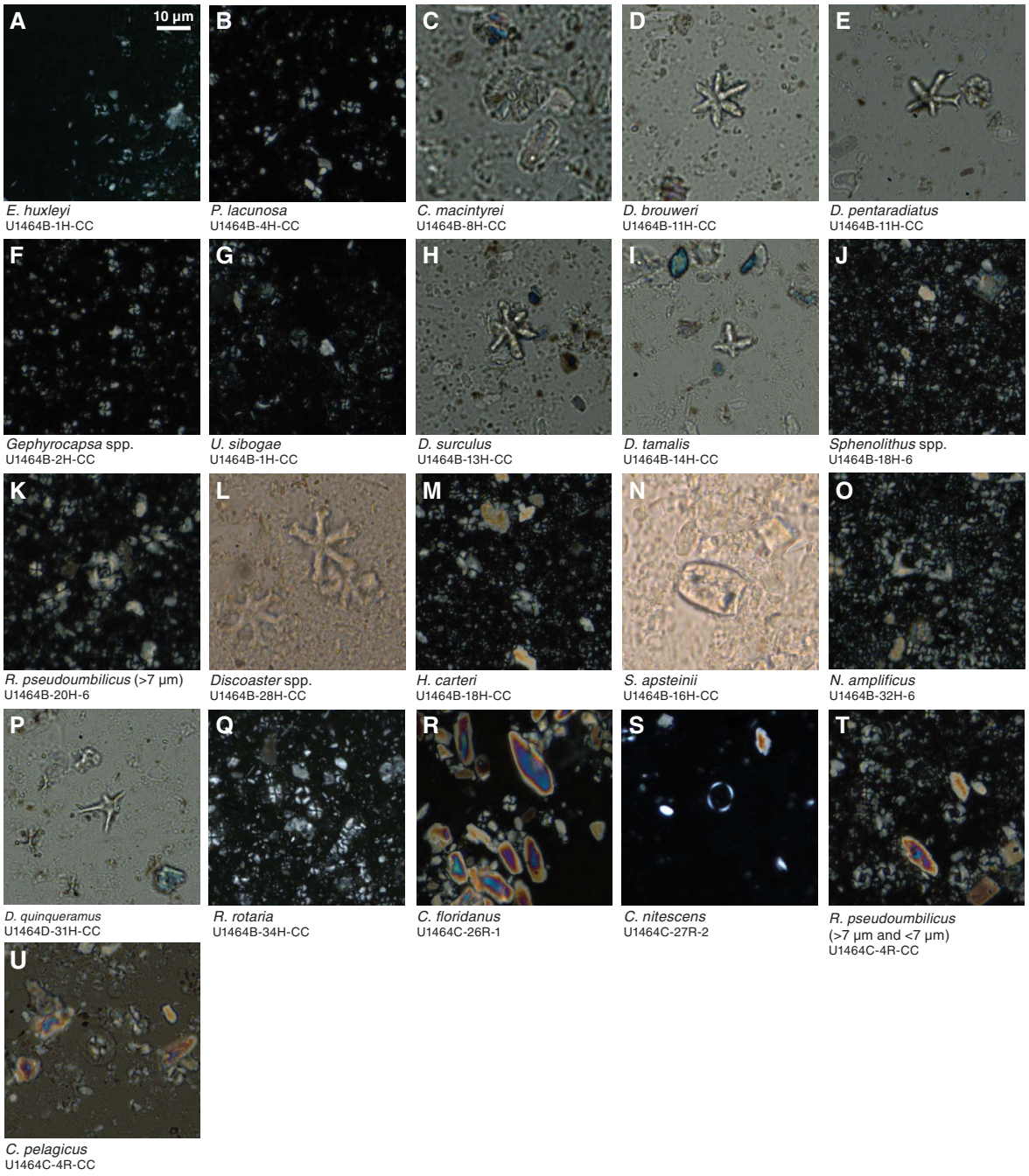

~309.1 m CSF-A (early Pliocene) downhole, preservation was generally poor (poor to barren) and accordingly, the abundance of planktonic foraminifers decreased (Figure **F14**; Table **T9**). An extended barren interval occurs in the bottom part of Hole U1464C from 347.13 to 832.76 m CSF-A (Sections 6R-1 through 56R-1), corresponding to the deepest sections of the site.

The general preservation for the Pleistocene–Pliocene section is good at Site U1464 and comparable to Site U1463 (Figure **F13**). Accordingly, the biostratigraphy is well constrained down to the early Pliocene (Tables **T7**, **T8**; Figure **F15**). The Middle Pleistocene (transition Biozone Pt1a–Pt1b) at 0.61 Ma, marked by the top of *G. tosaensis*, is in Sample 356-U1464B-2H-CC (11.51 m CSF-A). The early Pleistocene is characterized by the base of *Globorotalia truncatulinoides* (base of Biozone Pt1a, 1.93 Ma) in Sample 6H-CC (49.82 m CSF-A), followed by the transition into the Pliocene below the top of *G. limbata* (Biozone PL5, 2.39 Ma) in Sample 10H-CC (88.17 m CSF-A). Pliocene marker species, such as *D. altispira* (3.47 Ma, top of Biozone PL4), *Pulleniatina primalis* (3.66 Ma, top of Bio-

Table T7. Calcareous nannofossil (CN) and planktonic foraminifer (PF) datums, Site U1464. * = datums likely out of position. X = change in coiling direction. BF = benthic foraminifer datum. Ages are based on Gradstein et al. (2012). Table is based on all core catcher samples from all holes, indicating only the highest/lowest depth for each top/base event. **Download table in .csv format.**

Hole, core, section	Depth CSF-A (m)	Marker species	Type (CN/PF)	Zone name	Age (Ma)	Reference
356-						
U1464D-1H-CC	3.55	Base *E. huxleyi*	CN	NN21	0.29	Gradstein et al., 2012
U1464B-2H-CC	11.51	Top *G. tosaensis*	PF	Pt1a	0.61	Gradstein et al., 2012
U1464B-4H-CC	30.82	Top *P. lacunosa*	CN	NN19	0.44	Gradstein et al., 2012
U1464B-6H-CC	49.82	Top *C. macintyrei*	CN	NN19	1.60	Gradstein et al., 2012
U1464B-6H-CC	49.82	Top *G. fistulosus*	PF	Pt1a	1.88	Gradstein et al., 2012
U1464B-6H-CC	49.82	Base *G. truncatulinoides*	PF	Pt1a	1.93	Gradstein et al., 2012
U1464D-6H-CC	51.33	Top *C. macintyrei*	CN	NN19	1.60	Gradstein et al., 2012
U1464B-7H-CC	59.46	Top *D. brouweri*	CN	NN18	1.93	Gradstein et al., 2012
U1464D-7H-CC	60.84	Top *G. extremus*	PF	PL6	1.99	Gradstein et al., 2012
U1464B-8H-CC	69.09	Top *G. apertura*	PF	Pt1a	1.64	Gradstein et al., 2012
U1464D-9H-CC	79.83	Top *G. limbata*	PF	PL5	2.39	Gradstein et al., 2012
U1464B-10H-CC	88.17	Top *D. pentaradiatus*	CN	NN17	2.39	Gradstein et al., 2012
U1464B-11H-CC	97.42	Top *D. surculus*	CN	NN16	2.49	Gradstein et al., 2012
U1464B-14H-CC	126.30	Top *D. tamalis*	CN	NN16	2.80	Gradstein et al., 2012
U1464B-14H-CC	126.30	Base *G. fistulosus*	PF	PL5	3.33	Gradstein et al., 2012
U1464B-14H-CC	126.30	Base *G. tosaensis*	PF	PL5	3.35	Gradstein et al., 2012
U1464B-14H-CC	126.30	Top *D. altispira*	PF	PL4	3.47	Gradstein et al., 2012
U1464D-15H-CC	136.87	Top *P. primalis*	PF	PL3	3.66	Gradstein et al., 2012
U1464B-18H-6	163.00	Top *Sphenolithus* spp.	CN	NN16 (basal part)	3.54	Gradstein et al., 2012
U1464B-18H-6	163.00	Top *G. margaritae*	PF	PL2	3.85	Gradstein et al., 2012
U1464D-19H-CC	173.23	Top *R. pseudoumbilicus*	CN	NN15	3.7	Gradstein et al., 2012
U1464B-20H-CC	180.20	Top *S. seminulina**	PF	PL3	3.58	Gradstein et al., 2012
U1464D-21H-CC	189.65	X *Pulleniatina* sin to dex	PF	PL2	4.08	Gradstein et al., 2012
U1464D-25H-CC	228.35	Top *S. kochi*	PF	PL1	4.53	Gradstein et al., 2012
U1464D-31H-CC	281.39	Top *D. quinqueramus*	CN	NN11	5.59	Gradstein et al., 2012
U1464B-32H-6	293.15	Top *N. amplificus*	CN	NN11	5.94	Gradstein et al., 2012
U1464B-34H-CC	312.75	Top *R. rotaria*	CN	NN11	6.25	Young, 1998
U1464C-26R-1	541.67	Top *C. floridanus*	CN	NN7	11.85	Gradstein et al., 2012
U1464C-27R-2	552.50	Top *C. nitescens*	CN	NN6	12.12	Gradstein et al., 2012
U1464C-30R-1	579.91	Above base *C. macintyrei*	CN	NN6	13.36	Gradstein et al., 2012
U1464C-43R-2	707.57	Top *N. ferreroi*	BF	TF1-2	12.8	Renema, 2007; Marshall et al., 2015

Table T8. Planktonic foraminifer presence, abundance, and preservation at Site U1464, including characteristic mineral and other bioclast occurrences. **Download table in .csv format.**

zone PL3), and *Globorotalia margaritae* (3.85 Ma, top of Biozone PL2), are in the same intervals in Holes U1464B and U1464D (Table **T7**; Figure **F15**) and additionally, early Pliocene Biozone PL1 could be identified at Site U1464 by the top of *S. kochi* (top at 4.53 Ma) in Section 356-U1464C-30H-5 (272.57 m CSF-A). The well-preserved samples also allowed determination of the dominant coiling direction in the genus *Pulleniatina* spp. (Table **T10**; Figure **F16**) (Saito, 1976; Pearson, 1995). One well-recorded change from sinistral to 100% dextral coiling can be used as a stratigraphic marker for the early Pliocene (4.08 Ma), identified at ~196.6 m CSF-A.

Benthic foraminifers

Because of poor recovery, no core catcher samples were investigated from Hole U1464A. A total of 22 samples were examined from Hole U1464B, 29 from Hole U1464C, and 17 from Hole U1464D. Spot samples were taken from Sections 356-U1464B-34H-3 and 34H-6 (306–312 m CSF-A) in order to constrain the interval of rapid change between Assemblages 2 and 3 (see below). Overall, the number of species present per sample ranged from 1 (Sample 356-U1464C-24R-CC; 523.52 m CSF-A) to 43 (Samples 356-U1464B-1H-CC and 2H-CC; 2.26–7.88 m CSF-A) with an average of 14 per sample. The benthic foraminiferal percentage ranged from 6% (e.g., Section 356-U1464B-34H-3; 306.88 m CSF-A) to 100% (e.g., Sample 356-U1464C-6R-CC; 347.13 m CSF-A to the base of the hole) (Tables **T11**, **T12**). Section 356-U1464C-22R-4 (508.2 m CSF-A) and Samples 356-U1464D-55X-CC through 58X-CC (506.85–523.97 m CSF-A) were barren of benthic foraminifers.

Preservation in Hole U1464B ranged from very good to poor with the majority of samples being good (10 out of 22) (Table **T11**). In Hole U1464C, all samples showed poor preservation, and preservation of samples from Hole U1464D ranged from good to poor. Preservation was affected by abrasion and fragmentation (breakage), as well as occasional cementation and infilling (coating in secondary crystals) with glauconite and pyrite. Secondary crystal coating and clay clumps were partially removed by ultrasonication.

Cibicidoides spp. was almost always present throughout this site, but four foraminiferal assemblages were defined by varying dominant taxa. Except for Assemblage 3, all assemblages overlapped without clear boundaries (Table **T12**; Figure **F17**).

The first benthic foraminiferal assemblage is found in Holes U1464B and U1464D from the top to Samples 356-U1464B-6H-CC (49.8 m CSF-A) and 356-U1464D-5H-CC (41.8 m CSF-A). This assemblage contains a wide range of shallow-water (0–50 m) species, such as *Quinqueloculina* spp., but also abundant deeper (50–200 m) species, including *Lenticulina* spp. and *Cibicidoides* spp., with 21–43 species per sample and very good to moderate preservation. Other abundant taxa include *Textularia* spp., *Lagena* spp., and

Figure F13. Scanning electron microscope (SEM) photomicrographs of typical preservation states of planktonic foraminifers, Site U1464. The depicted species is *Globigerinoides sacculifer* (or closely related to *G. sacculifer*). Depths are in CSF-A.

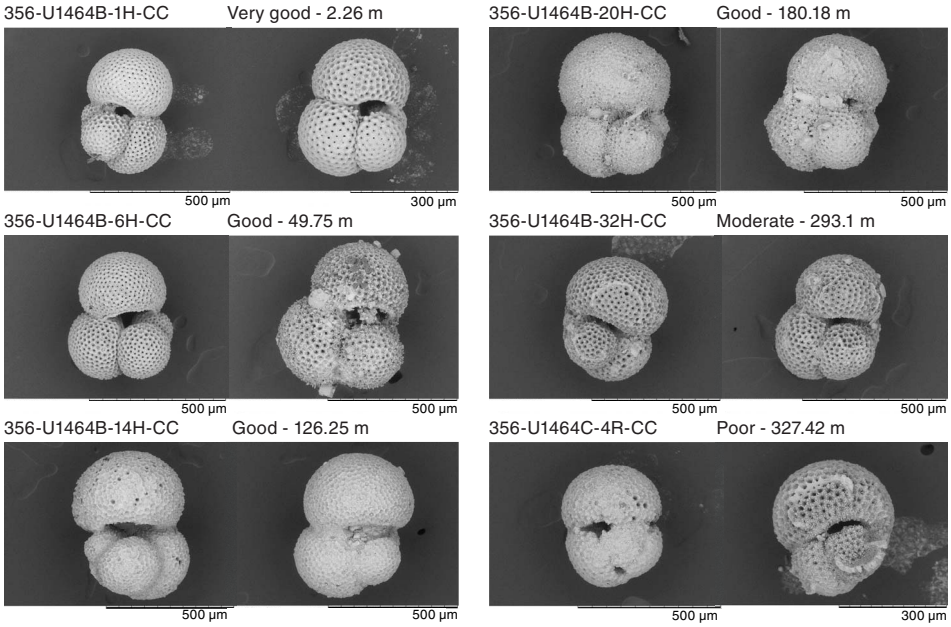

Figure F14. Planktonic foraminifer abundance, Site U1464. 0 = barren, 1 = very rare, 2 = rare, 3 = few, 4 = common, 5 = abundant (see **Biostratigraphy and micropaleontology** in the Expedition 356 methods chapter [Gallagher et al., 2017a] for definitions).

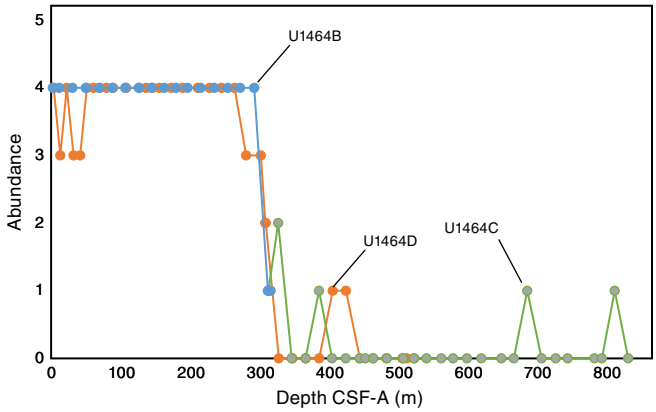

Sagrinella jugosa (Figure **F17**). The wide-ranging species comprising this assemblage suggest an inner to outer shelf environment.

Assemblage 2 is marked by the strong dominance of outer shelf and upper bathyal species, including *Lenticulina* spp., *Cibicidoides* spp., *Uvigerina peregrina*, and *C. subangularis*. This is further supported by the low benthic foraminifer percentage (6%–28%) per sample. Assemblage 2 was encountered in Samples 356-U1464B-8H-CC through Section 34H-3 (69.14–306.9 m CSF-A) and Samples 356-U1464D-6H-CC through 33X-CC. Assemblage 2 is additionally marked by the frequent occurrence of various relatively shallow water taxa (inner to middle shelf), including *Planorbulinella larvata, Pseudorotalia* spp., and *Neoeponides* spp., that have likely been transported downslope (Table **T11**; Figure **F17**).

Assemblage 3 is present in Section 356-U1464B-34H-6 through Sample 356-U1464C-24R-CC (310.8–523.5 m CSF-A) and Samples 356-U1464D-34X-CC through 53X-CC (309.1–483.65 m CSF-A) (Figure **F17**). With 1–15 species per sample and poor preservation, Assemblage 3 is dominated by inner to middle shelf taxa, including *Quinqueloculina* spp. and *Elphidium* spp., and LBFs, including *Amphistegina* spp., *P. larvata*, *Sphaerogypsina globulus*, and *Operculina* spp. Of additional note is the presence of the unusually large LBF *Cycloclypeus* spp. found in high abundance in Sections 356-U1464C-2R-3 through 3R-CC (313.42–327.4 m CSF-A). Specimens were well preserved and clearly visible within the core (see **Lithostratigraphy**). Because of their photosynthesizing endosymbionts and fragile test, *Cycloclypeus* is a genus of foraminifer indicative of environments within the photic zone but beneath the wave base (Hallock and Glenn, 1986).

Assemblage 4 is present from Section 356-U1464C-26R-1 to the base of the hole (541.7–832.76 m CSF-A). The assemblage has 3–12 species per sample with poor preservation. Assemblage 4 is dominated by *Cibicidoides* spp. in combination with normally only one or two other shallow and LBF taxa, including *Elphidium* spp., *Amphistegina* spp., *Operculina* spp., and *Eulepidina* spp. (Figure **F17**; Table **T11**). Of note is the abundance of *N. ferreroi* in Section 43R-2 (707.6 m CSF-A), an LBF species that was extinct by 12.8 Ma (Renema et al., 2007; Marshall et al., 2015). Specimens of the LBF genera *Sorites, Amphisorus, Miogypsina*, and *Lepidosemicyclina* were found in Sections 28R-1 through 32R-1 (563.01–600.05 m CSF-A) but were not removed because of their large sizes and fragile tests. Soritid genera *Sorites* and *Amphisorus* live attached to macroalgae, commonly *Halimeda* spp. (Debenay and Payri, 2010), which were found in thin sections from this section (see **Lithostratigraphy**).

Overall paleodepth estimates based on the planktonic/benthic foraminifer ratio (%P) range between 30 (100% benthic in Sample 356-U1464C-6R-CC to the base of the site through Assemblages 3 and 4; 347.1–832.9 m CSF-A) and >1000 m (6% benthic in Section 356-U1464B-34H-3; 306.9 m CSF-A in Assemblage 2) (Table **T11**). The shallowest paleodepths (30 m) are suggested by Assemblage 4; however, the poor preservation and large drop in planktonic abun-

Table T9. Planktonic foraminifer abundance, Site U1464. 0 = barren, 1 = very rare, 2 = rare, 3 = few, 4 = common, 5 = abundant (see the **Expedition 356 methods** chapter [Gallagher et al., 2017a] for definitions). **Download table in .csv format.**

Core, section	Depth CSF-A (m)	Abundance
356-U1464B-		
1H-CC	2.21	4
2H-CC	11.46	4
4H-CC	30.77	4
6H-CC	49.75	4
8H-CC	69.09	4
10H-CC	88.12	4
12H-CC	106.87	4
14H-CC	126.25	4
16H-CC	145.00	4
18H-6	162.95	4
20H-CC	180.13	4
22H-CC	196.60	4
24H-CC	215.64	4
26H-CC	235.20	4
28H-CC	254.68	4
30H-5	272.57	4
32H-6	293.10	4
34H-CC	312.70	1
35F-CC	316.89	1
356-U1464C-		
2R-CC	313.42	1
4R-CC	327.40	2
6R-1	347.08	0
8R-1	367.08	0
10R-1	386.35	1
12R-CC	405.16	0
14R-1	425.08	0
16R-2	445.38	0
17R-CC	453.50	0
18R-2	464.63	0
20R-2	484.60	0
22R-5	508.10	0
24R-CC	523.47	0
26R-1	541.62	0
28R-CC	563.01	0
30R-1	579.86	0
32R-1	600.05	0
33R-CC	611.47	
34R-2	620.77	0
37R-2	649.53	0
39R-2	667.58	0
41R-1	686.91	1
43R-2	707.52	0
45R-3	728.10	0
47R-1	745.35	0
51R-1	783.98	0
52R-2	794.72	0
54R-1	813.21	1
56R-1	832.71	0
356-U1464D-		
1H-CC	3.50	4
2H-CC	13.11	3
3H-CC	22.35	4
4H-CC	32.16	3
5H-CC	41.80	3
6H-CC	51.28	4
7H-CC	60.84	4
8H-CC	70.53	4
9H-CC	79.83	4
10H-CC	89.35	4
12H-CC	108.24	4
14H-CC	127.42	4
15H-CC	136.87	4
16H-CC	146.48	4
17H-CC	155.85	4
19H-6	173.18	4
21H-CC	189.65	4
23H-CC	211.46	4
25H-CC	228.35	4
27H-CC	245.64	4
29H-4	264.60	4
31H-CC	281.36	3
33X-CC	302.44	3
34X-CC	309.05	2
35X-CC	309.53	2
37X-CC	328.47	0
39X-CC	348.14	0
41X-CC	367.20	0
43X-CC	386.76	0
45X-CC	406.25	1
47X-CC	425.40	1
49X-CC	445.30	0
51X-CC	464.41	0
53X-CC	483.60	0
55X-CC	506.80	0
57X-CC	513.30	0
58X-CC	523.92	0

dance makes it likely that the %P of this assemblage is not representative and therefore unreliable for paleodepth reconstructions. The overall paleodepth pattern for this site based on a combination of %P and assemblage composition indicates an inner to outer shelf assemblage (1) that deepens to an outer shelf to upper bathyal assemblage (2). At Assemblage 3, the water depth becomes immediately shallower with an inner to middle shelf setting and then becomes slightly deeper again in Assemblage 4 with a middle to outer shelf setting.

Investigated benthic foraminifer percentage and diversity for Site U1464 are illustrated in Figure **F18**.

Figure F15. Planktonic foraminiferal marker species ranges, Holes U1464B and U1464D. Ages are based on published values (Gradstein et al., 2012) and placed halfway between the respective base or top of each species in both holes. X marks change in coiling direction in *Pulleniatina* spp.

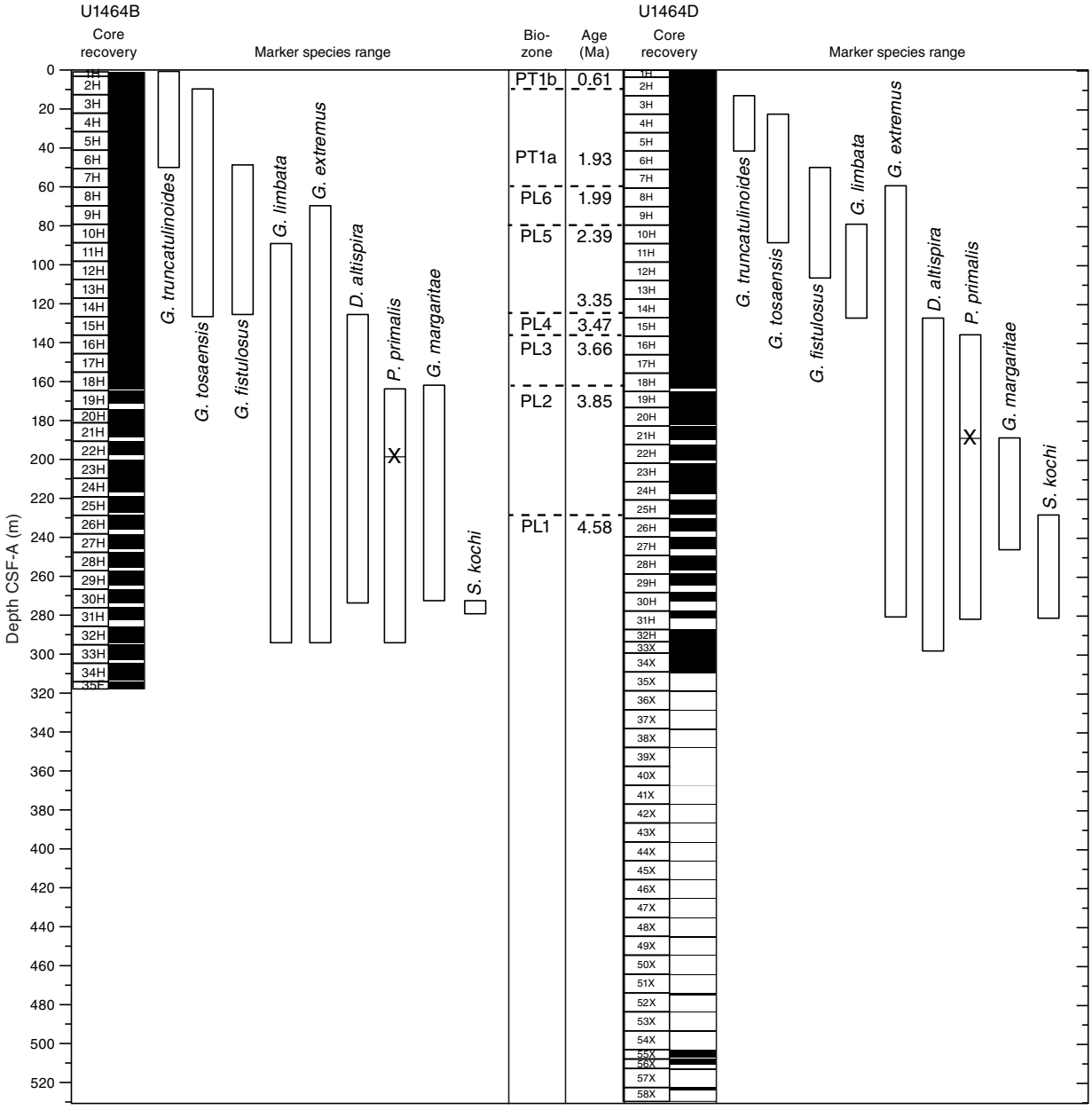

Table T10. Coiling direction for *Pulleniatina* spp. at Site U1464 including specific species per sample. Estimated age based on Table **T7** and Saito (1976). **Download table in .csv format.**

Hole, core, section	Top depth CSF-A (m)	Bottom depth CSF-A (m)	Species	Dextral	Sinistral	Total	% dextral	Estimated age	Coiling age	Saito, 1976 events
356-										
U1464D-1H-CC	3.50	3.55	*P. obliquiloculata*	21	0	21	100			
U1464B-2H-CC	11.46	11.51	*P. obliquiloculata*	15	1	16	94	0.61	0.8?	L1
U1464D-2H-CC	13.11	13.16	*P. obliquiloculata*	6	0	6	100			
U1464D-3H-CC	22.35	22.40	*P. obliquiloculata*	17	1	18	94			
U1464B-4H-CC	30.77	30.82	*P. obliquiloculata*	7	0	7	100			
U1464D-5H-CC	41.80	41.85	*P. obliquiloculata*	5	0	5	100	1.93		
U1464B-6H-CC	49.75	49.80	*P. obliquiloculata*	13	4	17	76	1.93	~1.93	L5/L6
U1464D-6H-CC	51.28	51.33	*P. obliquiloculata*	8	4	12	67			
U1464D-7H-CC	60.84	60.89	*P. obliquiloculata*	1	6	7	14	1.99		
U1464B-8H-CC	69.09	69.14	*P. obliquiloculata*	9	2	11	82	1.99		
U1464D-8H-CC	70.53	70.58	*P. obliquiloculata*	10	0	10	100	2.39		
U1464D-9H-CC	79.83	79.88	*P. obliquiloculata*	6	0	6	100			
U1464B-10H-CC	88.12	88.17	*P. obliquiloculata*	6	14	20	30			
U1464D-10H-CC	89.35	89.40	*P. obliquiloculata*	5	4	9	56	3.35		
U1464B-12H-CC	106.87	106.92	*P. obliquiloculata*	13	1	14	93			
U1464B-14H-CC	126.25	126.30	*P. obliquiloculata*	15	0	15	100			
U1464D-14H-CC	127.42	127.47	*P. obliquiloculata*	2	0	2	100	3.47		
U1464D-15H-CC	136.87	136.92	*P. obliquiloculata/P. primalis*	5	0	5	100	3.66		
U1464B-16H-CC	145.00	145.05	*P. obliquiloculata*	8	0	8	100			
U1464D-16H-CC	146.48	146.53	*P. obliquiloculata/P. primalis*	3	0	3	100			
U1464B-18H-CC	162.95	163.00	*P. obliquiloculata/P. primalis*	7	0	7	100			
U1464D-19H-6	173.18	173.23	*P. obliquiloculata/P. primalis*	7	0	7	100			
U1464B-20H-CC	180.13	180.18	*P. obliquiloculata/P. primalis*	10	0	10	100			
U1464D-21H-CC	189.65	189.70	*P. primalis*	2	7	9	22	3.85		
U1464B-22H-CC	196.60	196.65	*P. primalis*	0	10	10	0		4.08	L9
U1464B-24H-CC	215.64	215.69	*P. primalis*	0	3	3	0			
U1464D-27H-CC	245.64	245.69	*P. primalis*	0	2	2	0			
U1464D-29H-6	264.60	264.65	*P. primalis*	0	6	6	0			
U1464B-32H-6	293.10	293.15	*P. primalis*	0	5	5	0			

Figure F16. Variation in the coiling direction of planktonic foraminiferal genus *Pulleniatina*, Site U1464. Samples to 127 m CSF-A are *P. obliquiloculata*, samples deeper than 189 m CSF-A are *P. primalis*, and samples in between are a mixture of both species. Note that specimens of *P. finalis* were included with *P. obliquiloculata* (Kennett and Srinivasan, 1983). Ages are based on Saito (1976) and Pearson (1995) and recalibrated following Wade et al. (2011).

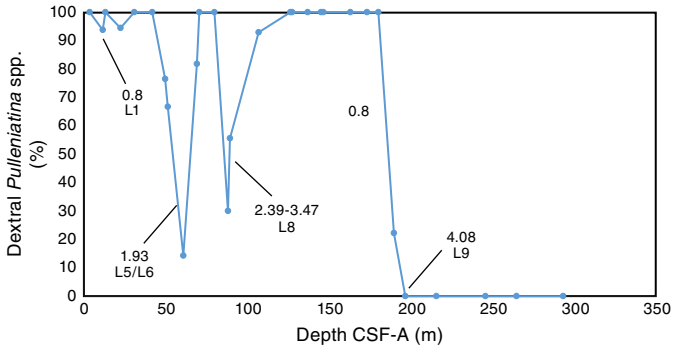

Table T11. Occurrence of the main genera and species of benthic and planktonic foraminifers and additional bioclasts and minerals, Site U1464. Preservation: M = moderate, G = good, VG = very good. Paleodepth estimates are based on calculations from van Hinsbergen et al. (2005). Bathymetric zones: IS = inner shelf, MS = middle shelf, OS = outer shelf, UB = upper bathyal. Abundance: C = common, P = present, R = rare. (Only a portion of this table appears here. The complete table is available in **.csv format**.)

			Benthic foraminifers							Planktonic foraminifers				Other							
Core, section	Top depth CSF-A (m)	Bottom depth CSF-A (m)	Preservation	Benthic foraminifers/total foraminifers (%)	Planktonic foraminifers/total foraminifers (%)	Paleodepth estimate %P (m)	Total number of benthic species	Bathymetric zone	Most abundant benthic foraminifer species (descending order)	Preservation	Total number of planktonic species	Most frequent planktonic foraminifer species	Biozone (Gradstein et al., 2012)	Glauconite	Pyrite	Sponge spicules	Ostracods	Pteropods	Fish teeth	Bryozoans	Comment
356-U1464A-																					
1X	No recovery																				
356-U1464B-																					
1H-CC	2.21	2.26	VG	37	63	419	43	IS/MS/OS	*Textularia* spp., *Bulimina* spp., *Cibicidoides* spp., *Discorbinella* spp.	VG	14	*C. nitida, G. rubescens, G. calida, G. siphonifera, G. glutinata, G. ruber, G. sacculifer, G. hirsuta, G. menardii, G. truncatulinoides, N. dutertrei, O. universa*					X	X			Ostracods (R); pteropods (P); scaphopods (C); mollusk
2H-CC	11.46	11.51	G	18	82	924	43	IS/MS/OS	*Cassidulina carinata, Cibicides* spp., *Cibicidoides* spp., *Lenticulina* spp., *Quinqueloculina* spp., *Sagrinella jugosa, Textularia* spp.	G	12	*G. siphonifera, G. ruber, G. sacculifer, G. crassaformis, G. menardii, G. truncatulinoides, N. dutertrei, O. universa, P. obliquiloculata*									Glauconite; 94% dex *Pulleniatina* (15 dex, 1 sin)
4H-CC	30.77	30.82	M	16	84	1005	25	OS/UB	*Cibicidoides* spp., *Cibicides* spp., *Lagena* spp.	M	12	*G. siphonifera, G. ruber, G. sacculifer, G. menardii, N. dutertrei, O. universa, P. obliquiloculata*					X				Peloids; ostracod (P); 100% dex *Pulleniatina* (7 dex, 0 sin)
6H-CC	49.75	49.80	M	10	90	1290	21	OS/UB	*Cibicidoides* spp., *Lagena* spp., *Lenticulina* spp., *Brizalina semilineata, Cibicides* spp., *Sphaeroidina bulloides, Textularia* spp.	G	13	*G. siphonifera, G. ruber, G. sacculifer, G. trilobus, G. crassaformis, G. menardii, G. tosaensis, G. truncatulinoides, N. dutertrei, O. universa, P. obliquiloculata*									Glauconitized pteropods; 76% dex *Pulleniatina* (13 dex, sin 4)

Table T12. Benthic foraminifer abundance, Site U1464. **Download table in .csv format.**

Figure F17. Optical and SEM photomicrographs of dominant benthic foraminiferal species and assemblages at Site U1464 with paleodepth based on planktonic/benthic ratio (%P) and bathymetric zone interpretation. Assemblage bathymetric zones were smoothed to generate a synthesis, resulting in slight differences from hole summary data. For raw bathymetric zonation see Table **T11**. This figure is available in an **oversized format**.

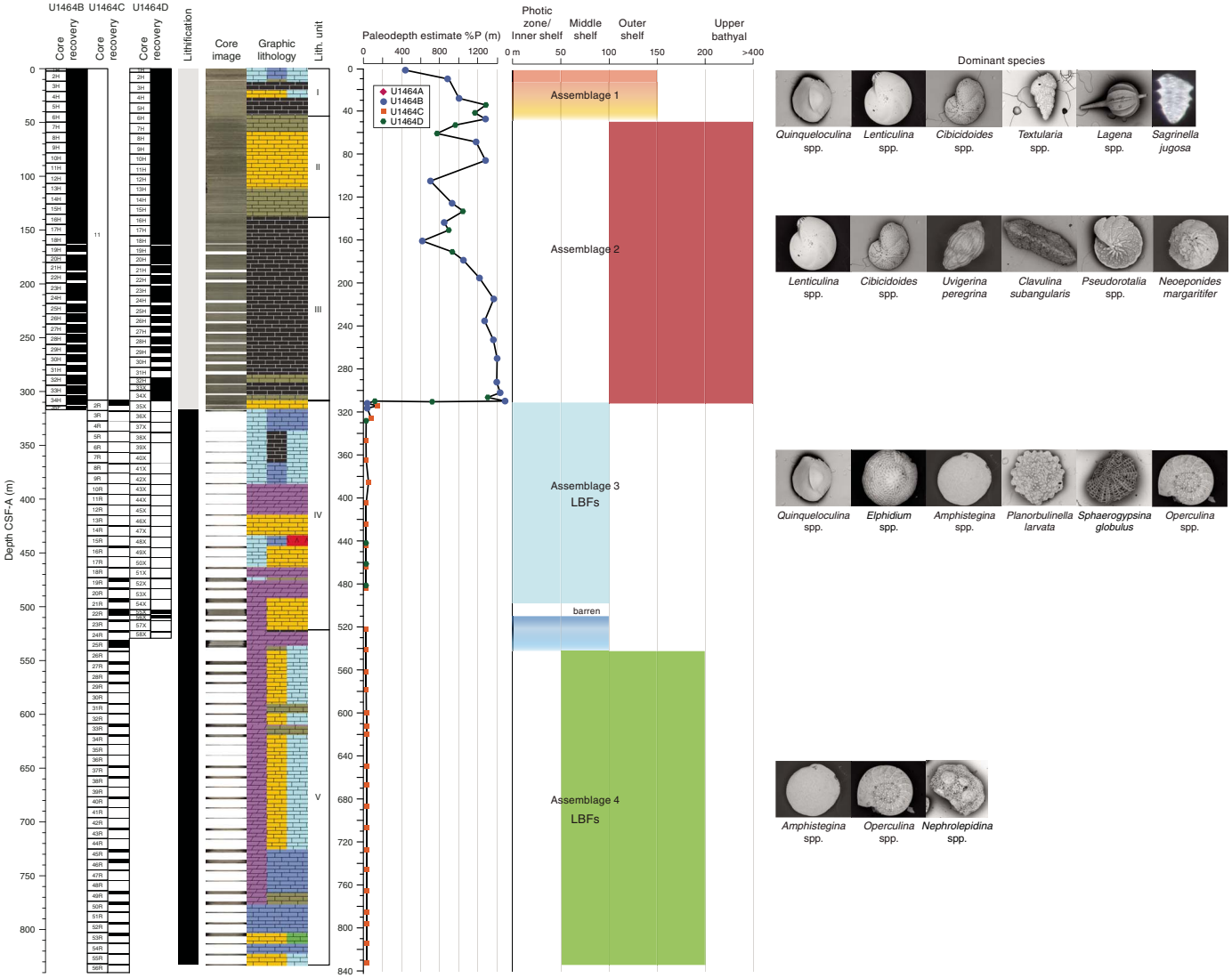

Figure F18. Benthic foraminifer diversity (number of species) and benthic percentage of total foraminifers, Site U1464. Analyzed samples from Holes U1464B–U1464D are combined by CSF-A.

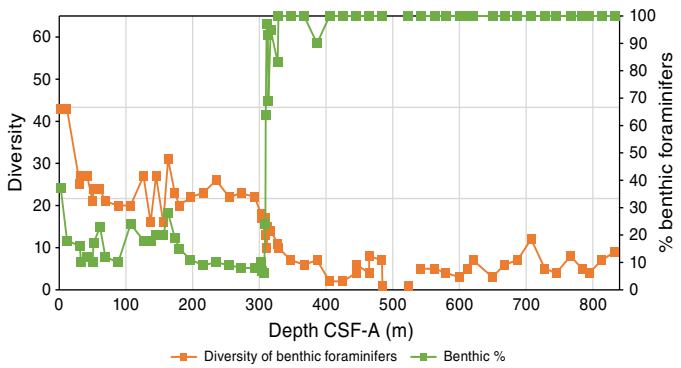

Geochemistry

At Site U1464, 85 samples were analyzed for headspace gas content, 20 samples (5–15 cm whole rounds) for interstitial water (IW) geochemistry measurements, and 23 samples for bulk sediment geochemistry (total organic carbon [TOC], calcium carbonate, and total nitrogen [TN]). In general, Site U1464 is characterized by the lowest headspace gas concentrations of all of the Expedition 356 sites, with methane concentrations ranging from 0 to 3.2 parts per million by volume (ppmv) and almost no detection of higher molecular weight hydrocarbons. Elevated salinity characterizes the site, with a value of 35 at the top, increasing gradually with depth to a value of 105 at ~300 m CSF-A (mean = 68). Deeper than ~300 m CSF-A, one sample at ~318 m CSF-A (Section 356-U1464C-3R-1) has a lower salinity value of 87. Similar to IODP Sites U1462 and U1463, high salinity at Site U1464 and a number of elemental trends

noted in the IW samples appear to be related to the presence and dissolution of anhydrite, which was observed in lithostratigraphic Units IV and V. A number of elements exhibit increasing concentrations with depth, including sodium, chloride, barium, bromine, calcium, potassium, and sulfate. The majority of samples at this site are characterized by high calcium carbonate content (mean = 78.8 wt%) and low TOC (mean = 0.6 wt%) and TN (mean = 0.018 wt%). However, two samples from black layers in Sections 356-U1464C-24R-2 and 25R-2 have low calcium carbonate content (3.6 and 2.7 wt%, respectively) but exhibit different characteristics in TOC and TN values. The sample at 523 m CSF-A (Section 24R-2) contains low TOC (0.77 wt%) and TN (0.034 wt%) values, similar to samples from other depths. In contrast, the slightly deeper sample at 532 m CSF-A (Section 25R-2) has much higher TOC (1.94 wt%) and TN (0.079 wt%) values, suggesting that, despite appearing visually similar, these black layers may represent different depositional environments.

Headspace gases

Headspace gas analysis for routine safety monitoring revealed the presence of methane in very low concentrations, the lowest of the Expedition 356 sites. One of the 85 samples analyzed did not contain methane (Section 356-U1464B-15H-4). For the remaining 84 samples, methane concentrations range from 1.4 to 3.2 ppmv with an average of 1.9 ppmv (Figure **F19**; Table **T13**). Only one sample at 580 m CSF-A (Section 356-U1464C-30R-1) was found to contain a trace amount of ethene (0.4 ppmv). No higher molecular weight hydrocarbons were detected.

Interstitial water geochemistry

Geochemical measurements of IW samples were not possible deeper than 318 m CSF-A because of low core recovery and insufficient IW quantities in lithified sediments from Hole U1464C. Therefore, "bottom" in this geochemistry section refers to ~318 m CSF-A (Section 356-U1464D-3R-1).

Salinity ranges from 35 to 105 (Figure **F20**). From 0 to ~40 m CSF-A, salinity values remain constant with values between 35 and 39. Deeper than 40 m CSF-A, a trend of increasing salinity values with depth is noted until ~300 m CSF-A. Similar to Sites U1462 and U1463, the unusually high salinity at this site may be related to the dissolution of anhydrite ($CaSO_4$), which is observed in Unit V (see **Lithostratigraphy**). Deeper than ~300 m CSF-A, one sample (from Section 356-U1464C-3R-1) at ~318 m CSF-A has a lower salinity value of 87. Overall, alkalinity at Site U1464 is low, with values ranging from 0.92 to 3.23 mM (Figure **F20**). From 0 to 83 m CSF-A, alkalinity displays decreasing values (3.23 to 1.21 mM) with depth, followed by relatively constant values (0.92–1.32 mM) to 318 m CSF-A. pH decreases from 7.8 to 7.1 from the surface to ~270 m CSF-A and subsequently increases toward 318 m CSF-A.

Sodium, chloride, bromide, calcium, magnesium, sulfate, and potassium display relatively constant values shallower than ~40 m CSF-A, followed by gradually increasing values until ~300 m CSF-A; the deepest IW sample at 318 m CSF-A has slightly lower concentrations of all these elements (Figures **F20**, **F21**). These trends are all similar to that of salinity (Figure **F20**).

Phosphate values were mostly below detection limit, except for a single value of 2.9 µM at 1.5 m CSF-A (Section 356-U1464B-1H-1) (Figure **F21**). Deeper than ~50 m CSF-A, calcium and sulfate concentrations slightly increase, which may be related to the dissolution of anhydrite. Variations in sulfate and ammonium concentrations are positively correlated, suggesting that no sulfate reduction zone is present.

Figure F19. Hydrocarbons in headspace gases, Site U1464.

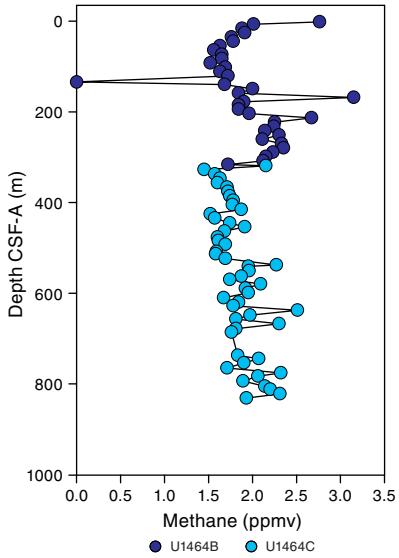

Table T13. Headspace gas contents, Site U1464. **Download table in .csv format.**

Variations in most minor elements show similar trends between Sites U1463 and U1464 (Figure **F20** in the Site U1463 chapter [Gallagher et al., 2017d]; Figure **F22**). Downhole trends of boron and lithium have relatively constant values shallower than ~40 m CSF-A, then gradually increase with depth until ~270 m CSF-A, and then decrease toward 318 m CSF-A (Figure **F22**). Manganese values were below detection limit in the upper ~54 m CSF-A except for the sample at the surface (0.19 µM; Section 356-U1464B-1H-1). Deeper than 50 m CSF-A, manganese gradually increases to 1.6 µM at ~270 m CSF-A and then decreases toward 318 m CSF-A. Barium was not detected at the surface (Section 1H-1) or at 16 (Section 3H-3), 82.65 (Section 10H-3), and 92.15 m CSF-A (Section 11H-3), and the concentration is relatively low (<1.1 µM) throughout the cored interval when detectable. Silicon concentrations are relatively constant in the upper ~270 m CSF-A and then decrease toward 318 m CSF-A. Iron values were mostly below detection limit in the upper ~185 m CSF-A, followed by an increasing trend toward 270 m CSF-A.

Bulk sediment geochemistry

In addition to the residual IW squeeze cake material routinely analyzed for bulk geochemistry during this expedition, three additional sediment samples were analyzed for calcium carbonate, TOC, and TN. Two of these samples were taken in visually detectable black layers (Sections 356-U1464C-24R-2 and 25R-2; see detailed description in **Lithostratigraphy**), and a third was taken in the nearby laminated section (Section 25R-5).

For the samples measured on the squeeze cake material shallower than 318 m CSF-A, calcium carbonate content ranges from 61.9 to 95.5 wt% with a mean of 78.8 wt% (Figure **F23**). From the top of the hole to ~54 m CSF-A, calcium carbonate values are relatively constant at 87–90 wt%. Between 45 and 54 m CSF-A (Sections 356-U1464B-6H-3 and 7H-3), calcium carbonate values drop from 87 to 73 wt% and subsequently a general trend of increasing values is

Figure F20. Alkalinity, pH, salinity, sodium, chloride, and sodium to chloride ratio, Site U1464.

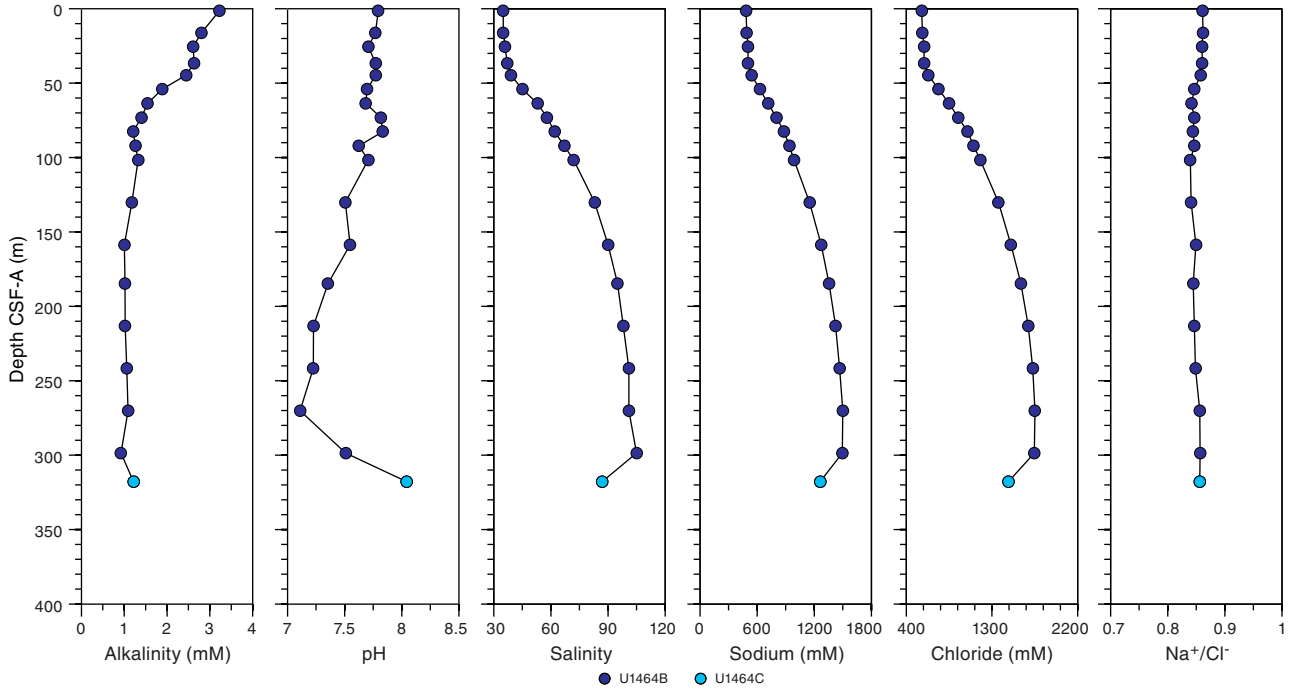

Figure F21. Major element interstitial water geochemistry (bromide, calcium, magnesium, potassium, sulfate, ammonium, and phosphate), Site U1464.

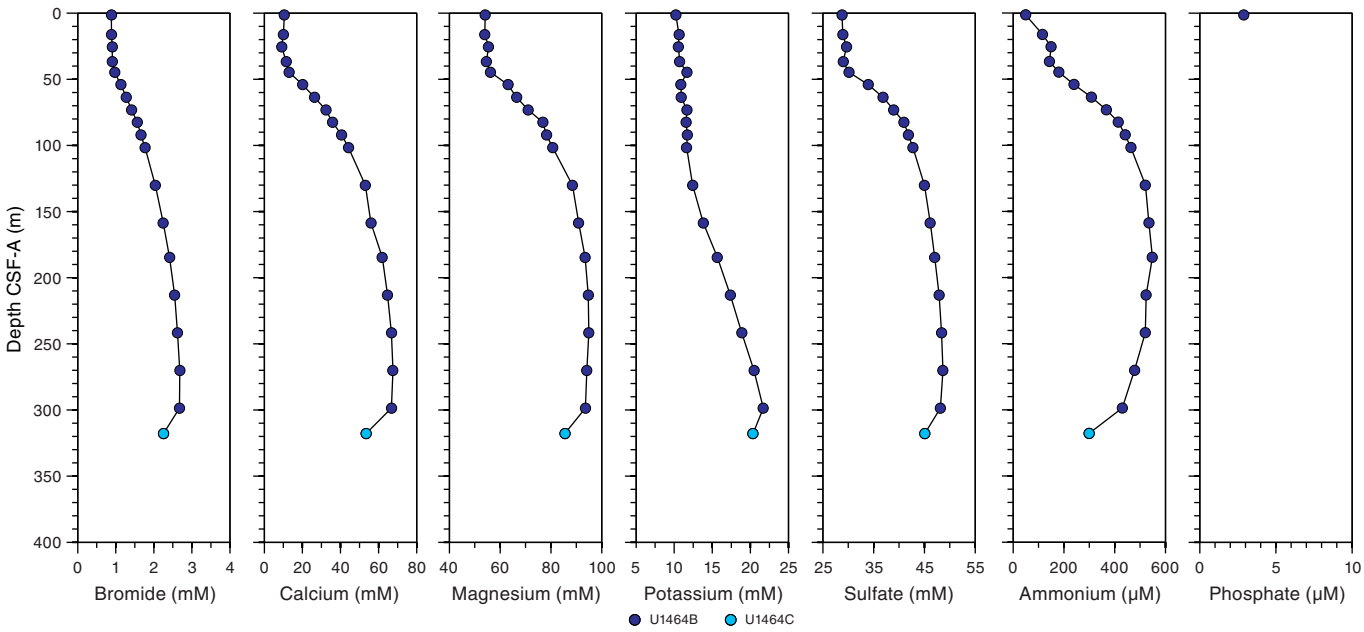

noted until 130 m CSF-A. Between 130 and 159 m CSF-A, another large change in calcium carbonate occurs with values dropping from 84 to 65 wt%. From 159 to 299 m CSF-A, values fluctuate between 62 and 73 wt%. Here, another transition is noted with the samples at 318 (Section 356-U1464C-3R-1) and 464 m CSF-A (Sample 3R-1) having significantly higher calcium carbonate values of 95.5 and 90.3 wt%, respectively. TOC content ranges from 0.3 to 0.82 wt% with a mean of 0.6 wt%. TN values are low, ranging from 0.002 to 0.032 wt% with a mean of 0.018 wt%. One sample at ~37 m CSF-A (Section 5H-4) yielded a negative TOC value (–0.33 wt%) and thus has been excluded from the figures. It is likely that TOC was below the detection level in this sample.

Samples from the black layers have extremely low calcium carbonate contents (3.6 and 2.7 wt%), whereas the sample from the laminated section has a high calcium carbonate content (84.4 wt%) (Figure **F23**). For TOC and TN, the two samples from the black layers show different characteristics. The sample at 523 m CSF-A (Section 356-U1464C-24R-2) contains low TOC (0.77 wt%) and TN

Figure F22. Minor element interstitial water geochemistry (barium, boron, iron, lithium, manganese, silicon, and strontium), Site U1464. Iron and manganese were below detection level in some samples.

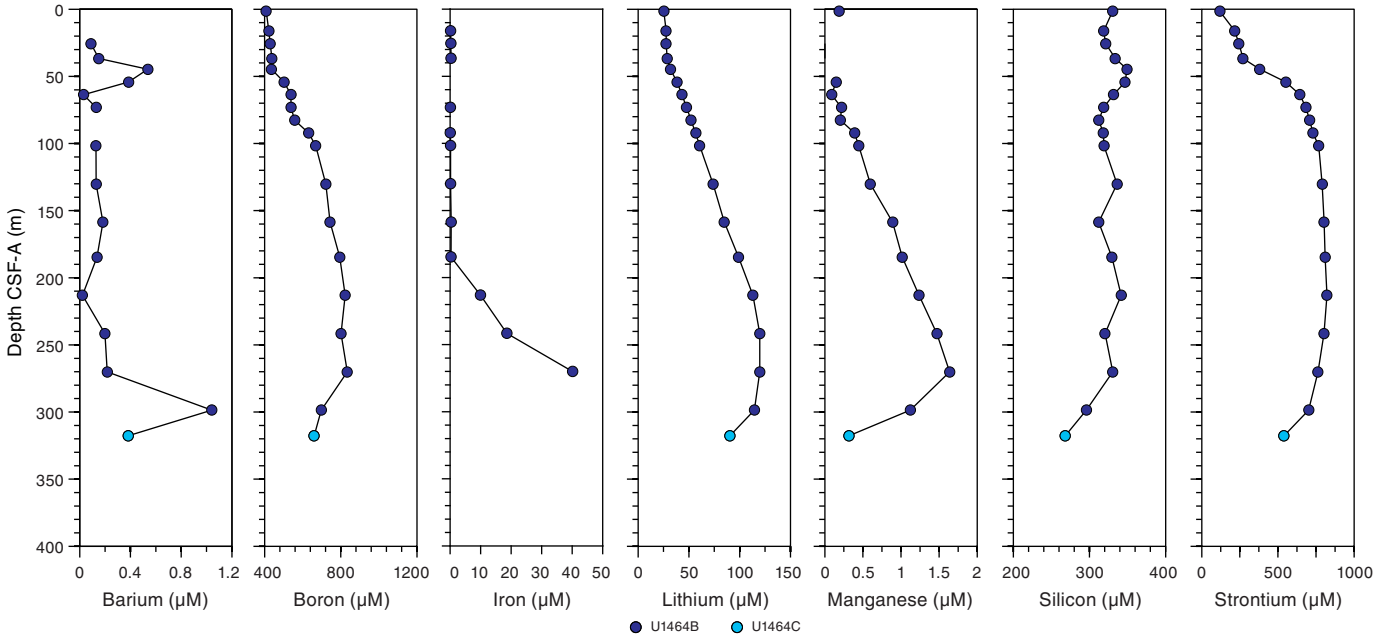

Figure F23. Bulk sediment geochemistry (calcium carbonate, TOC, and TN), Site U1464. Black dashed line around the three lowermost samples denotes that these were taken from discrete black (top and middle samples in the box) and laminated layers (bottom sample); thus, the geochemistry of these individual layers may not be representative of the majority of the sediment.

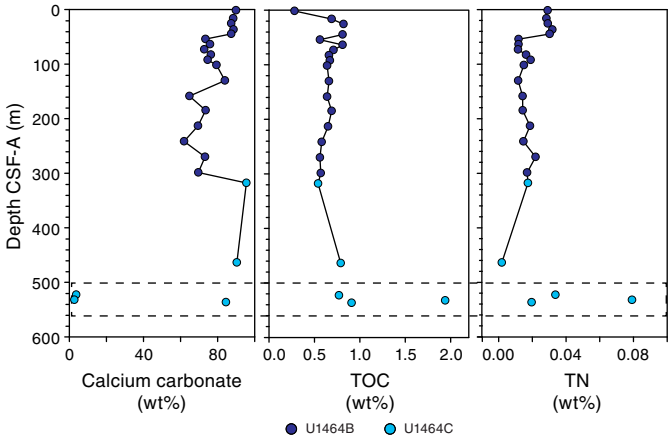

(0.034 wt%) values, similar to samples from the other depths. In contrast, the sample at 532 m CSF-A (Section 25R-2) has higher TOC (1.94 wt%) and TN (0.079 wt%) values.

Paleomagnetism

Paleomagnetism investigations at Site U1464 focused on natural remanent magnetization (NRM) and alternating field (AF) demagnetization measurements. Superconducting rock magnetometer (SRM) results are reported from cores recovered with the APC system in Hole U1464D. Archive-half section cores from Hole U1464D were measured on the SRM to construct the magnetostratigraphy. Resulting intensity values generally ranged from 10^{-5} to -10^{-3} A/m, with exceptions between ~158–180 m CSF-A and ~245–293 m CSF-A, for which intensity values reached ~10^{-1} A/m. Magnetostratigraphic data for Hole U1464D may provide evidence for the Gauss/Gilbert boundary (3.596 Ma; Gradstein et al., 2012) at ~282 m CSF-A. In addition, it is possible that the Chron C3n/C3r boundary (5.235 Ma; Gradstein et al., 2012) occurs between 272.66 and 277.85 m CSF-A, near a 5.59 Ma biostratigraphic datum at 281.39 m CSF-A (see **Biostratigraphy and micropaleontology**).

Rock magnetic measurements were performed on 20 discrete samples taken from Holes U1464B–U1464D. Isothermal remanent magnetization (IRM) acquisition and backfield IRM measurements were performed for four selected discrete samples chosen according to the observed demagnetization behavior from measurements made on archive-half cores. Two samples reached saturation IRM (SIRM) at ~100 mT, and one sample saturated at ~400 mT. Sample 356-U1464B-18H-4, 74–76 cm, did not reach saturation in fields up to 1.2 T, showing a possible correlation to sediments deeper than ~275 m CSF-A in Hole U1463B. Remanent coercivity values of the four samples ranged between 44 and 83 mT.

Archive-half measurements

Archive-half sections from Hole U1464D were measured on the SRM to construct the magnetostratigraphy for Site U1464 (Figure **F24**). The results indicate that intensity values range from 10^{-5} to 10^{-3} A/m for most of the material, with the exception of the intervals between ~158 and 180 m CSF-A (Cores 356-U1464D-18H through 22H), and between ~245 and 293 m CSF-A (Cores 27H through 32H), for which intensity values reached ~10^{-1} A/m. The interval between ~158 and 180 m CSF-A (Core 18H through 22H) is characterized by high MS (see **Physical properties**). Declination values from Cores 2H through 32H (12.37–293.26 m CSF-A) were corrected using data provided by the Icefield MI-5 orientation tool (see the **Expedition 356 methods** chapter [Gallagher et al., 2017a]).

AF cleaning of up to 20 mT revealed a persistent negative inclination trend from the top of the succession to ~210 m CSF-A (Core 356-U1464D-23H), where there is an overall shift toward shallower inclination values and more frequent positive inclination intervals. A possible explanation for this trend is that characteristic remanent

Figure F24. Magnetostratigraphic data, Hole U1464D. Magnetic inclination, declination, and intensity data from archive-half sections measured on the SRM after background and tray correction with polarity (black = normal, white = reversed, gray = unidentified) and biostratigraphic datums. Measurements from the tops and bases of sections were omitted (see the **Expedition 356 methods** chapter [Gallagher et al., 2017a]).

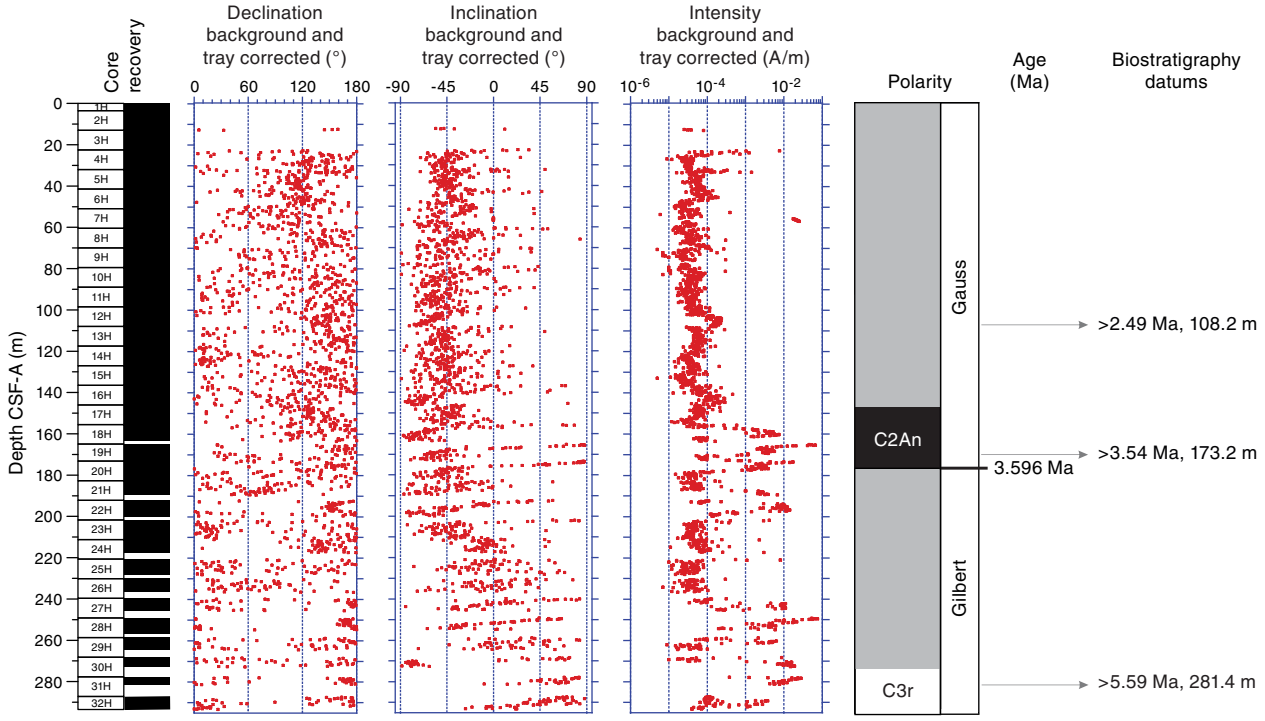

magnetization was better characterized deeper than ~210 m CSF-A by the AF cleaning up to 20 mT because of a change in magnetic mineralogy, similar to the transition at ~275 m CSF-A in magnetic mineralogy characteristics of sediments from Hole U1463B (see the **Site U1463** chapter [Gallagher et al., 2017d]).

Magnetostratigraphy

Magnetostratigraphic data from measurements on archive-half sections from Hole U1464D (Figure **F24**; Table **T14**) may encompass the Gauss/Gilbert boundary. In order to distinguish reversals, we estimated a −33.1° magnetic inclination for the latitude of Hole U1464D (18°3.9230′S) based on the geocentric axial dipole model. The high-intensity interval from Cores 356-U1464D-18H through 20H (155.5–182.11 m CSF-A) and also present in Core 22H (192.2–200.17 m CSF-A), indicates a prominent bias of inclination data toward negative values, corresponding to normal polarity. Correlation with biostratigraphic datums of 2.49 Ma (108.24 m CSF-A) and 3.54 Ma (173.18 m CSF-A) suggest that this interval may represent Chron C2An, the Gauss Chron (2.581–3.596 Ma). Despite the recovery gaps between Cores 29H (~265 m CSF-A) and 32H (270–293.26 m CSF-A), there is a transition from normal polarity at 272.66 m CSF-A (Core 30H) to reversed polarity at 277.85 m CSF-A (Core 31H). The 5.59 Ma biostratigraphic datum at 281.39 m CSF-A (see **Biostratigraphy and micropaleontology**) indicates that the Chron C3n/C3r boundary (5.235 Ma) at the Gilbert Chron and could be associated with the reversal between 272.66 and 277.85 m CSF-A.

Discrete sample measurements

A total of 20 discrete samples from Holes U1464B–U1464D underwent AF demagnetization, of which four (Samples 356-U1464B-18H-4, 74–76 cm [159.42 m CSF-A], 24H-3, 70–72 cm [212.4 m CSF-A], 356-U1464C-22R-4, 50–52 cm [506.7 m CSF-A], and 34R-1, 46–48 cm [618.86 m CSF-A]) were investigated further for magnetic mineralogy using IRM and backfield IRM acquisition measurements, as well as bulk susceptibility (Table **T15**; Figures **F25**, **F26**). IRM acquisition curves (Figure **F25**) indicate that Samples 356-U1464C-22R-4, 50–52 cm (506.7 m CSF-A), and 34R-1, 46–48 cm (618.86 m CSF-A), reached SIRM at low fields (~100–200 mT), which is commonly attributed to the presence of magnetite and/or titanomagnetite (Dunlop and Özdemir, 1997). One sample (356-U1464B-24H-3, 70–72 cm [212.4 m CSF-A]) reached saturation between 300 and 400 mT, indicating the presence of an intermediate-coercivity phase. Sample 356-U1464B-18H-4, 72–74 cm (159.42 m CSF-A), did not reach SIRM within the limit of shipboard analysis (~1.2 T), suggesting the presence of high-coercivity phases. However, examination of all individual IRM curves reveals a possible second distribution after 800 mT related to a high-coercivity phase that cannot be saturated in an impulse peak field of 1.2 T. The difference in magnetization intensity between Sample 18H-4, 72–74 cm, and the other three samples is noteworthy: Sample 18H-4, 72–74 cm, reached an intensity of 1.99 A/m, whereas the next highest intensity value, reached by Sample 24H-3, 70–72 cm (212.4 m CSF-A), was an order of magnitude lower (0.12 A/m). Backfield IRM acquisition measurements yielded a range of values, with Sample 18H-4, 72–74 cm, having the lowest remanent coercivity at about 43 mT, followed by Sample 356-U1464C-34R-1, 46–48 cm, with a value of ~45 mT, whereas Samples 356-U1464C-22R-4, 50–52 cm, and 356-U1464B-24H-3, 70–72 cm, yielded the highest coercivity of remanence values of ~66 and ~84 mT, respectively.

Bulk magnetic susceptibility measurements (Table **T15**) were conducted on all of the discrete samples taken from this site. Results ranged from 4.13×10^{-6} to 110.24×10^{-6} SI units, with the exception of Sample 356-U1464C-18R-2, 15–17 cm, and the three deepest dis-

Table T14. Core or sample intervals and correlative magnetozones, Holes U1464B–U1464D. Polarity and time interval from Gradstein et al. (2012). **Download table in .csv format.**

Core interval	Depth CSF-A (m)	Polarity, age, and chron
Higher confidence		
356-U1464D-		
18H through 20H and 22H	155.5–182.11, 192.2–200.17	Normal; Gauss C2An (2.581–3.596 Ma)
30H through 31H	272.66–277.85	C3n/C3r at Gilbert (5.235 Ma)

Table T15. Results of principal component analysis (PCA), together with NRM intensity and bulk susceptibility, for discrete samples, Site U1464. *D* = declination, *I* = inclination, MAD = maximum angular deviation, χ = bulk susceptibility, χm = mass susceptibility. **Download table in .csv format.**

Core, section	Top depth CSF-A (m)	NRM intensity (10^{-6} A/m)	χ (10^{-6} SI)	χm (10^{-3} SI/kg)	Component 1				Component 2			
					D (°)	*I* (°)	MAD (°)	PCA range (mT)	*D* (°)	*I* (°)	MAD (°)	PCA range (mT)
356-U1464C-												
8H-4	64.31	96.1	10.17	1.81	325.5	15.5	4.7	20–40				
12H-3	100.86	51.2	12.34	1.89	351.4	11.1	5.5	20–40				
15H-4	130.99	27.1	7.20	1.09	137.7	–2.5	8.1	20, 50, 60				
18H-4	159.42	9091.0	78.36	11.64	316.9	–7.7	3.2	NRM, 10, 20	291.6	0.5	7.2	30–60, 120–160
21H-4	185.34	117.0	29.23	5.10	331.6	17.5	15.4	NRM, 10, 20	345.0	4.5	14.1	30–80
24H-3	212.40	145.0	24.31	5.00	65.4	–15.0	15.9	20–40				
27H-2	239.37	176.0	37.36	5.61	177.2	–22.2	31.0	10, 30, 50–140				
30H-2	267.70	8290.0	110.24	15.53	191.7	–20.0	4.5	20–140				
33H-4	299.42	150.0	25.19	4.08	12.5	14.8	19.6	20–60				
35F-2	315.22	65.2	4.13	0.24	331.1	10.9	13.8	30–60				
356-U1464C-												
2R-1	308.27	2020.0	75.97	5.84	140.0	40.2	5.8	20–140				
18R-2	464.05	19.3	–3.36	–0.22	205.4	–21.5	36.2	20–50				
22R-4	506.70	84.4	7.07	0.42	280.7	70.7	14.8	20–40				
25R-3	534.12	34.1	5.08	0.33	349.2	37.8	14.9	20–50				
34R-1	618.86	95.2	25.19	1.63	182.4	–24.6	15.5	NRM to 60				
46R-1	736.00	39.0	–7.95	–0.51	325.2	8.9	13.7	30–50, 70				
49R-2	765.54	36.3	–6.77	–0.40	137.1	8.9	10.7	20, 40, 50, 70				
53R-1	803.90	24.1	–6.77	–0.40	122.1	25.5	19.6	20–50				
356-U1464D-												
5H-3	35.74	96.7	–2.17	–0.14	12.3	–33.4	6.3	10–30	86.2	13.0	7.0	60–80
5H-5	38.74	51.19	–3.41	–0.22	314.1	8.0	8.6	10–50	133.2	23.3	12.9	60–80

Figure F25. IRM acquisition curves for 4 discrete samples from Hole U1464B and their respective backfield curves. Inset shows an enlargement of backfield IRM curves, identifying coercivity of remanence values for each sample.

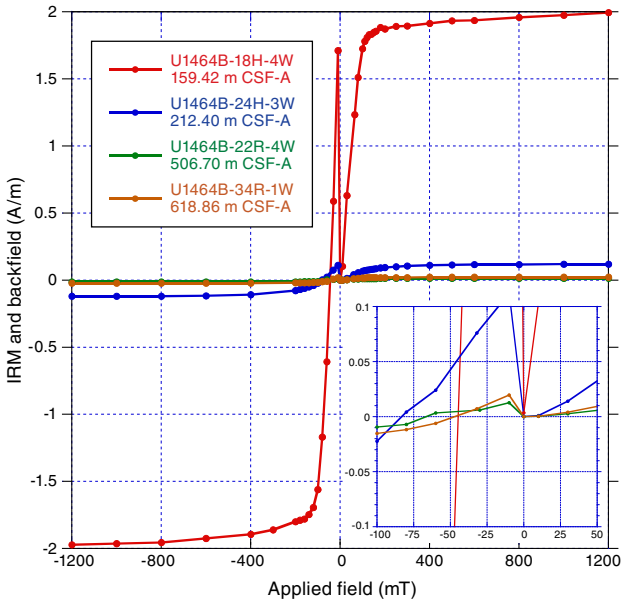

crete samples (46R-1, 120–122 cm [736 m CSF-A], 49R-2, 14–16 cm [765.54 m CSF-A], and 53R-1, 120–122 cm [803.9 m CSF-A]) that exhibited diamagnetic behavior (negative susceptibility values).

The directional data provided by AF demagnetization and subsequent principal component analysis (PCA) of discrete sample measurements (Figure **F26**; Table **T15**) indicate that, for most samples, the viscous remanent magnetization attributed to overprinting was completely removed after demagnetization at 10 mT. Most samples exhibited NRM values ranging from 10^{-6} to 10^{-4} A/m, except for Samples 356-U1464B-18H-4, 72–74 cm, 30H-2, 50–52 cm, and 356-U1464C-2R-1, 27–29 cm, which yielded values an order of magnitude higher (~10^{-3} A/m). These samples also indicate a component of higher stability in demagnetization trends, with ~10%–20% of the NRM still remaining after AF cleaning up to 140 mT. However, considering that the demagnetization behavior of most discrete samples was verified by means of PCA analysis, it is possible that the SRM AF demagnetization sequence (measurements at NRM, 10, and 20 mT) was in fact adequate for the archive-half measurements.

Figure F26. AF demagnetization results for discrete samples from 4 depths, Holes U1464B and U1464C. Orthogonal projections (Zijderveld diagram) and equal area projections of NRM vector measured after each demagnetization treatment. Horizontal = declination, vertical = inclination. Equal area projection: solid circles = positive inclination, open circles = negative inclination. Normalized magnetization behavior plots show highest magnetization intensity (M_{max}) = 1 on *y*-axis with AF demagnetization strengths shown after each measurement on *x*-axis.

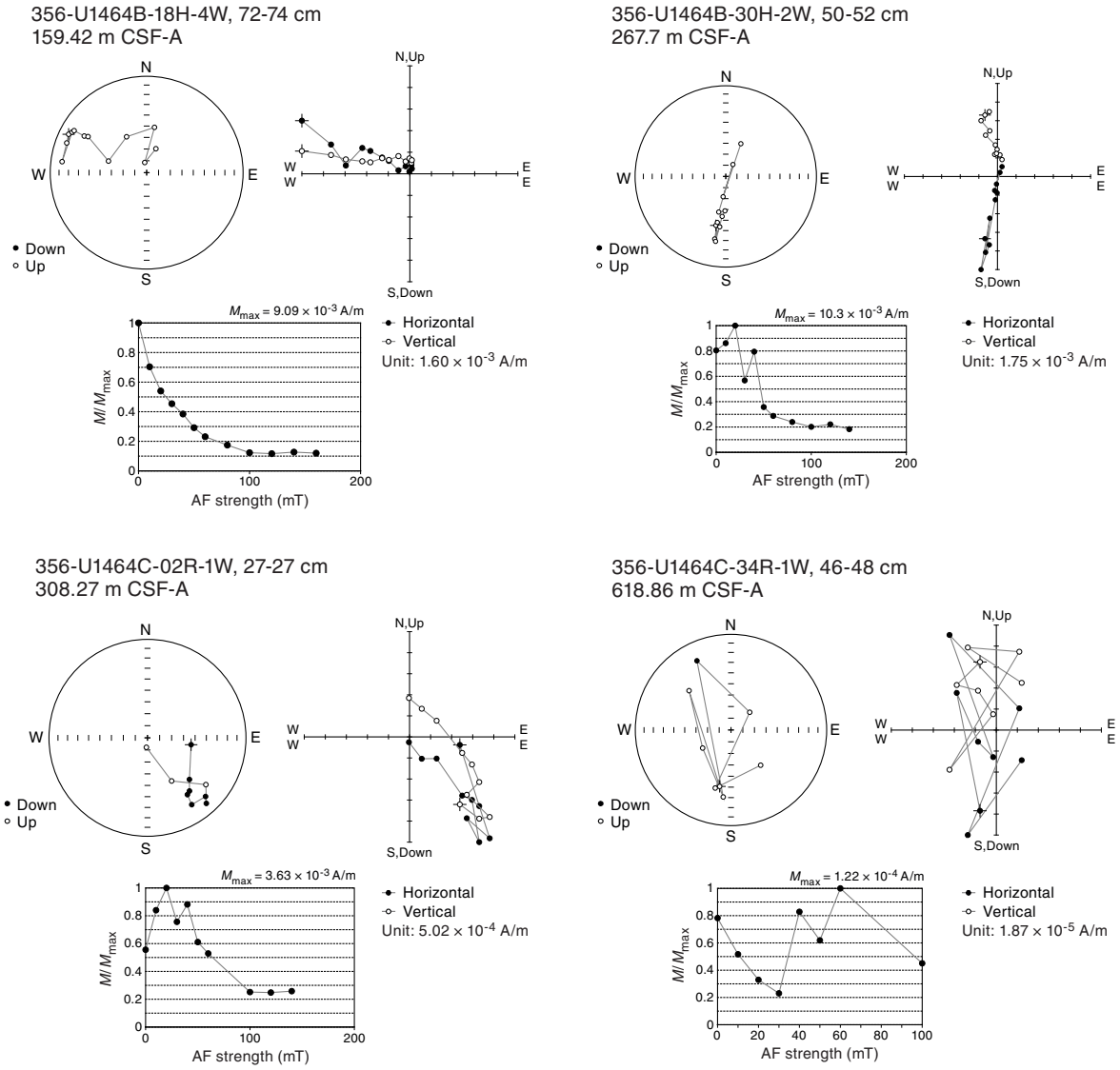

Physical properties

Physical properties measurements were performed using the Whole-Round Multisensor Logger (WRMSL), NGR sensor, and discrete sampling on cores from Site U1464. Stratigraphic overlap between Holes U1464B, U1464C, and U1464D is confirmed by physical properties patterns, including MS, NGR, and moisture and density (MAD) results. Detailed analysis of *P*-wave velocity, as measured in sediments obtained from three different coring techniques (APC, XCB, and RCB) reveal interesting variations. *P*-wave velocities measured on XCB and APC cores define parallel trends versus depth. However, XCB *P*-wave velocities fall within two distinct velocity ranges. The lower range is similar to *P*-wave velocities obtained on APC cores and corresponds to the lower strength (commonly referred to as "gravy") portion of the biscuited XCB core. A second range is ~150 m/s higher and corresponds to the higher strength "biscuits" portion. Sediments obtained during RCB coring tend to have velocities that are 400–650 m/s higher than those obtained during APC coring. Evaluation of differences between MAD bulk densities and gamma ray attenuation (GRA) bulk densities suggests that the source of deviations is a result of mineralogical variations. This is because MAD measurements incorporate mineralogical differences, whereas GRA bulk density estimates assume constant mineralogy throughout. An estimate of the geothermal heat flux of 59.1 mW/m^2 was derived from a combination of the six in situ temperature estimates and core-based thermal conductivity measurements.

Magnetic susceptibility

MS measurements were carried out on the WRMSL at 5.0 cm intervals and on the Section Half Multisensor Logger (SHMSL) at 2.5 cm intervals. SHMSL data were obtained by averaging two mea-

surements per position. WRMSL MS values in the top 150 m increase gradually from –1 to 4 SI with a shift from –1 to 2 SI at ~50 m CSF-A (Figure **F27**). From 160 m CSF-A to the bottom of Hole U1464B at 316.9 m CSF-A, several peaks are observed with ~20 SI amplitude. These trends are matched in the SHMSL data. The topmost cores in Hole U1464C (Cores 356-U1464C-2R and 3R) overlap the bottommost cores in Hole U1464B (Cores 356-U1464B-34H and 35F). This is illustrated by the presence of a prominent peak in MS at 310 m CSF-A in Hole U1464B and one at the same depth in Hole U1464C. Throughout the remainder of Hole U1464C, WRMSL MS values range from –3 to 2 SI with no evident peaks.

Natural gamma radiation

NGR was measured on whole-round cores at 10 cm intervals in Holes U1464B, U1464C, and U1464D (deeper than 287 m CSF-A) and at 20 cm intervals in the upper part of Hole U1464D. Between the seafloor and 50 m CSF-A, three peaks are observed with 40–80 counts/s amplitude (Figure **F27**). From 50 to 160 m CSF-A, NGR values are relatively invariant at about 20 counts/s. However, at ~90, 115–120, and 145 m CSF-A, several small peaks of about 30–35 counts/s are observed. From 160 to 305 m CSF-A, variability increases and values shift upward to about 30 counts/s. At 310 m CSF-A, a peak with 80 counts/s amplitude is observed in Holes U1464B and U1464D, and the bottom half of the peak is seen in Hole U1464C. This again confirms the overlap between the two holes. NGR counts range between 3 and 30 counts/s from 320 to 500 m CSF-A. In general, counts increase with a variability ranging from 10 to 45 counts/s between 500 and 620 m CSF-A. Deeper than 620 m CSF-A, the values decrease and range between 5 and 20 counts/s to the bottom of Hole U1464C (840 m CSF-A).

P-wave sonic velocity

P-wave velocities were measured using two different instruments: the WRMSL (5 cm intervals) in all holes and at least one or two discrete measurements made with the *P*-wave caliper on each core from Holes U1464B and U1464C and selected cores from Hole U1464D. In the top 300 m of Hole U1464B, *P*-wave velocity shows an increasing trend from ~1600 to 1900 m/s (Figure **F28**). From 300 m CSF-A to the bottom of Hole U1464B (317 m CSF-A), *P*-wave velocities increase rapidly with a maximum of 2150 m/s at 316 m CSF-A. In the overlapping portion of Hole U1464C, *P*-wave velocities range between 2303 and 2555 m/s. In Hole U1464D, XCB coring began at 293.5 m CSF-A. *P*-wave velocities between 293.5 and 310 m CSF-A show a velocity range between 1796 and 2261 m/s. The interval between 290 and 390 m CSF-A shows increasing *P*-wave velocities from a low of 1796 m/s to a high of 3545 m/s. This unit is underlain by a higher velocity unit from 390 to 540 m CSF-A. This unit exhibits velocities generally ranging from 2500 to 5581 m/s, with higher velocities tending to occur in the deepest 50 m of this interval. At 540 m CSF-A, there is an apparently abrupt shift to lower and less variable sonic velocities. From 540 m CSF-A to the bottom of Hole U1464C (840 m CSF-A), average velocities increase from ~2550 to 2900 m/s. The high-velocity unit within Hole U1464C (390–540 m CSF-A) is most likely related to a strong reflec-

Figure F27. WRMSL MS, SHMSL MSP, and NGR results, Site U1464. SHMSL data are drift-corrected MS from all holes.

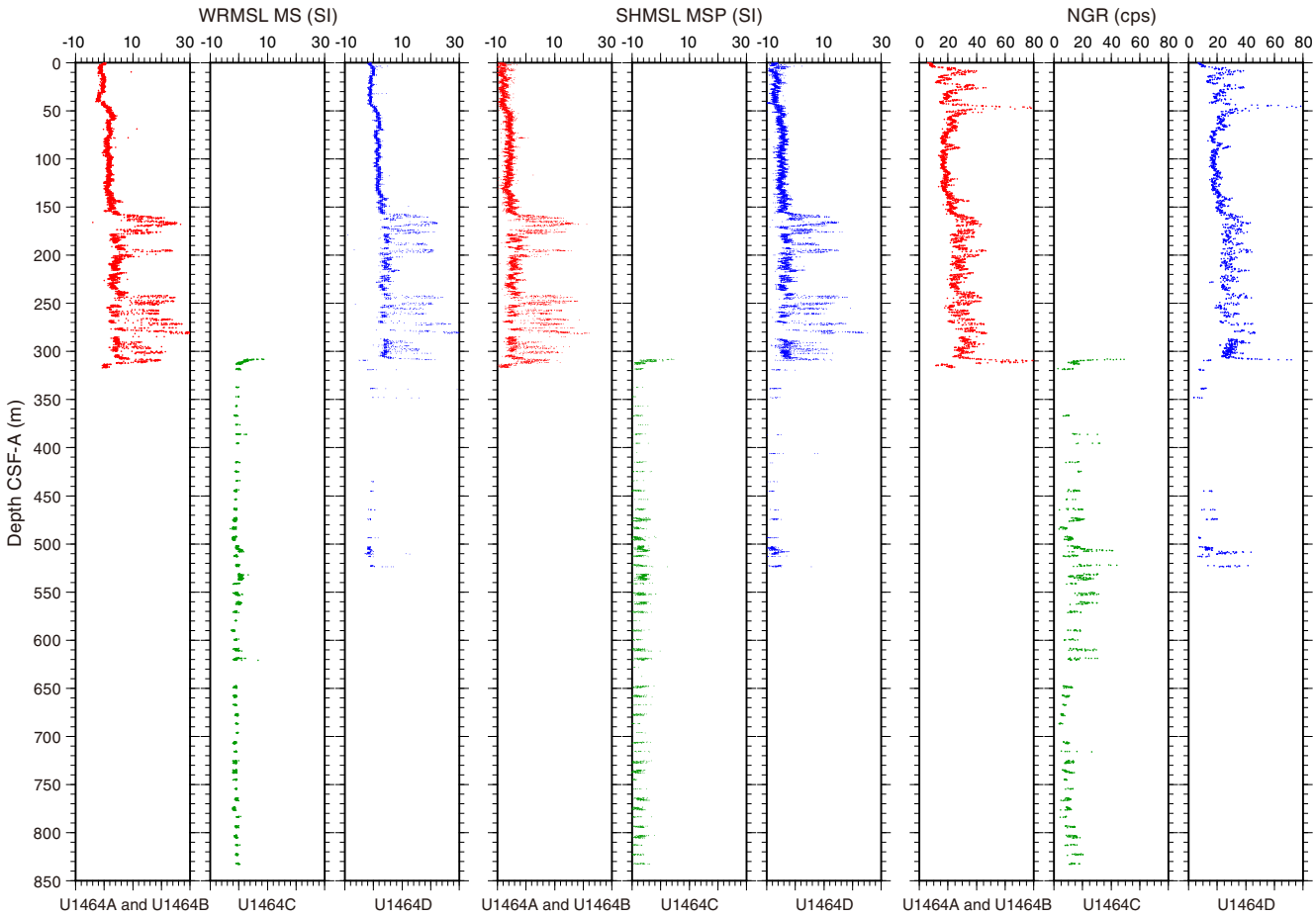

Figure F28. A. *P*-wave velocity, Site U1464 (dots = WRMSL, open circles = measured in liner, triangles = measured without liner; solid circles = MAD cubes with error bars showing ranges of their measurements taken in three orthogonal directions). B. Comparison of *P*-wave velocities measured on Site U1464 cores obtained using different drilling techniques. Red = Hole U1464B (APC), green = Hole U1464C (RCB), blue = Hole U1464D (XCB).

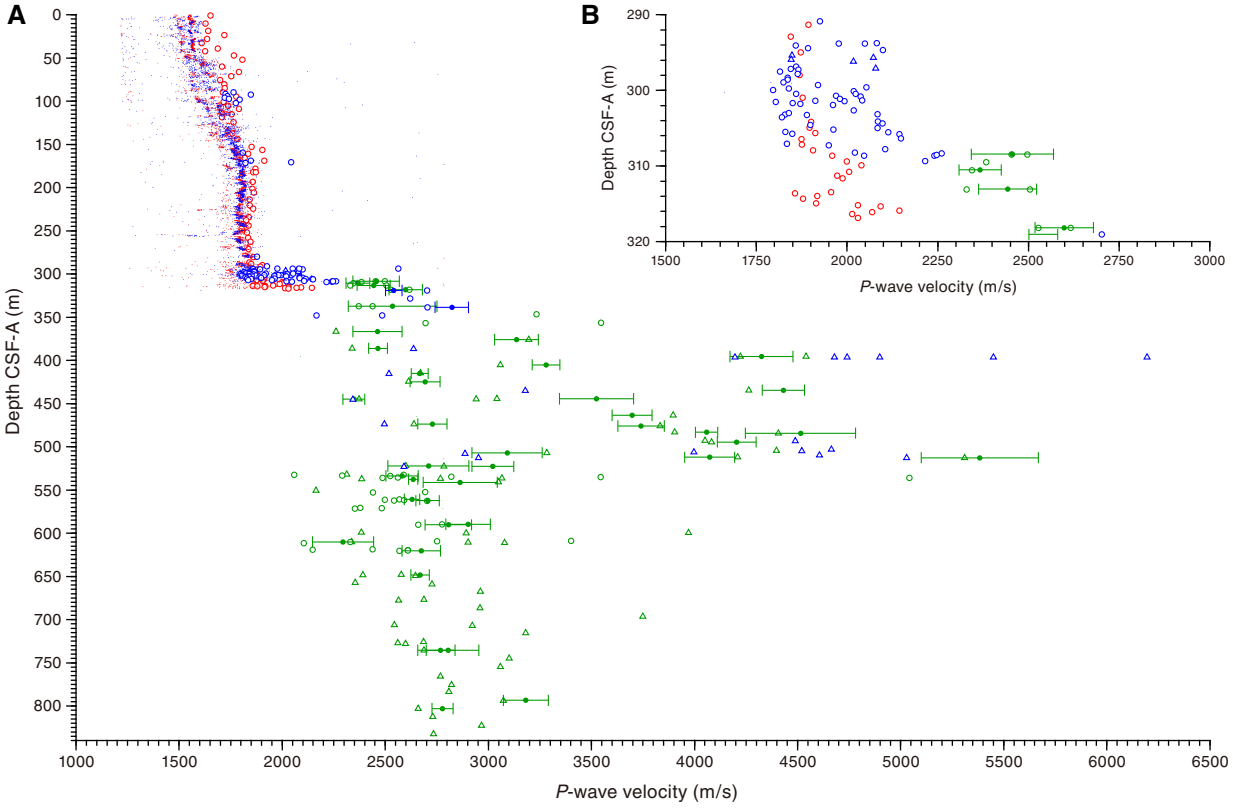

tor on seismic Profile JN87-07 at 0.680 s two-way traveltime (see Figure **F3**).

Overlapping coring with the three different coring techniques (APC, XCB, and RCB) allowed us to examine their impact on *P*-wave velocities (Figure **F28**). From 293.5 to 308 m CSF-A, the *P*-wave velocities in sediments from APC cores range from 1845 to 1897 m/s (11 measurements; Hole U1464B), whereas *P*-wave velocities in sediments from XCB cores in the same interval range between 1796 and 2148 m/s (55 measurements; Hole U1464D). These XCB data tend to fall in two distinct velocity ranges: the lower range corresponding to the velocities observed in APC cores and the higher range is offset by ~150 m/s. Low velocities correspond to fine-grained pseudolaminar material ("gravy") that is taken to be drilling slurry, whereas the higher velocities are from hard, coarser grained semilithified and less disturbed portions of the core ("biscuits"). These parallel data ranges persist to 309 m CSF-A, over which interval the velocities seen in APC cores from Hole U1464B continue to parallel the lower velocities observed in XCB cores from Hole U1464D. In the interval where all three coring methods overlap (308–310 m CSF-A), the highest velocities are obtained in the sediments that were collected using RCB coring (Hole U1464C). The overlap between RCB and APC coring continues beyond 310 m CSF-A to the bottom of Hole U1464B (317 m CSF-A) and suggests an offset of 400–650 m/s between the two coring methods. A similar discrepancy was also noted between APC and XCB coring at Site U1463, where XCB-cored sediments showed higher *P*-wave velocities than APC-cored sediments in an overlapping stratigraphic interval between holes (see **Physical properties** in the Site U1463 chapter [Gallagher et al., 2017d]).

Gamma ray attenuation

GRA was measured to estimate bulk density using the WRMSL at 5.0 cm intervals. Results are reported with those from discrete measurements of bulk density in **Moisture and density** below.

Moisture and density

In Holes U1464B and U1464C, MAD measurements were made on one or two samples per core, synchronizing with smear slides and thin sections. Bulk density increases from 1.5 g/cm^3 at the seafloor to about 2 g/cm^3 at 160 m CSF-A (Figure **F29**). From that depth to 305 m CSF-A in Hole U1464B, bulk density remains fairly constant at 2.05 g/cm^3. From 305 to 317 m CSF-A (the bottom of Hole U1464B), GRA inferred values suggest a shift in bulk density to about 2.25 g/cm^3. This corresponds to a peak in MS as well as in NGR counts. In the portion of Hole U1464C that overlaps with Hole U1464B (308–316.9 m CSF-A), MAD results for bulk density are in good agreement between the two holes. Deeper, bulk density increases from 2.1 to 2.25 g/cm^3 at 530 m CSF-A. Deeper than 530 m CSF-A, bulk density shows no large-scale trend but displays small-scale variability, ranging between 2.1 and 2.3 g/cm^3. A few outliers observed are associated with minor lithologies (see porosity discussion below for more details).

GRA bulk densities (ρ) and MAD bulk densities tend to be indistinguishable for the uppermost 100 m CSF-A. However, as was the case at Site U1463 (see the **Site U1463** chapter [Gallagher et al., 2017d]), bulk densities estimated using MAD methods tend to be lower than those estimated by GRA between 100 and 317 m CSF-A (Figure **F30**). We believe that this is a result of variations in mineral-

Figure F29. Bulk density (dots = GRA, open circles = MAD), grain density, and porosity, Site U1464. Red = Hole U1464B, green = Hole U1464C, blue = Hole U1464D.

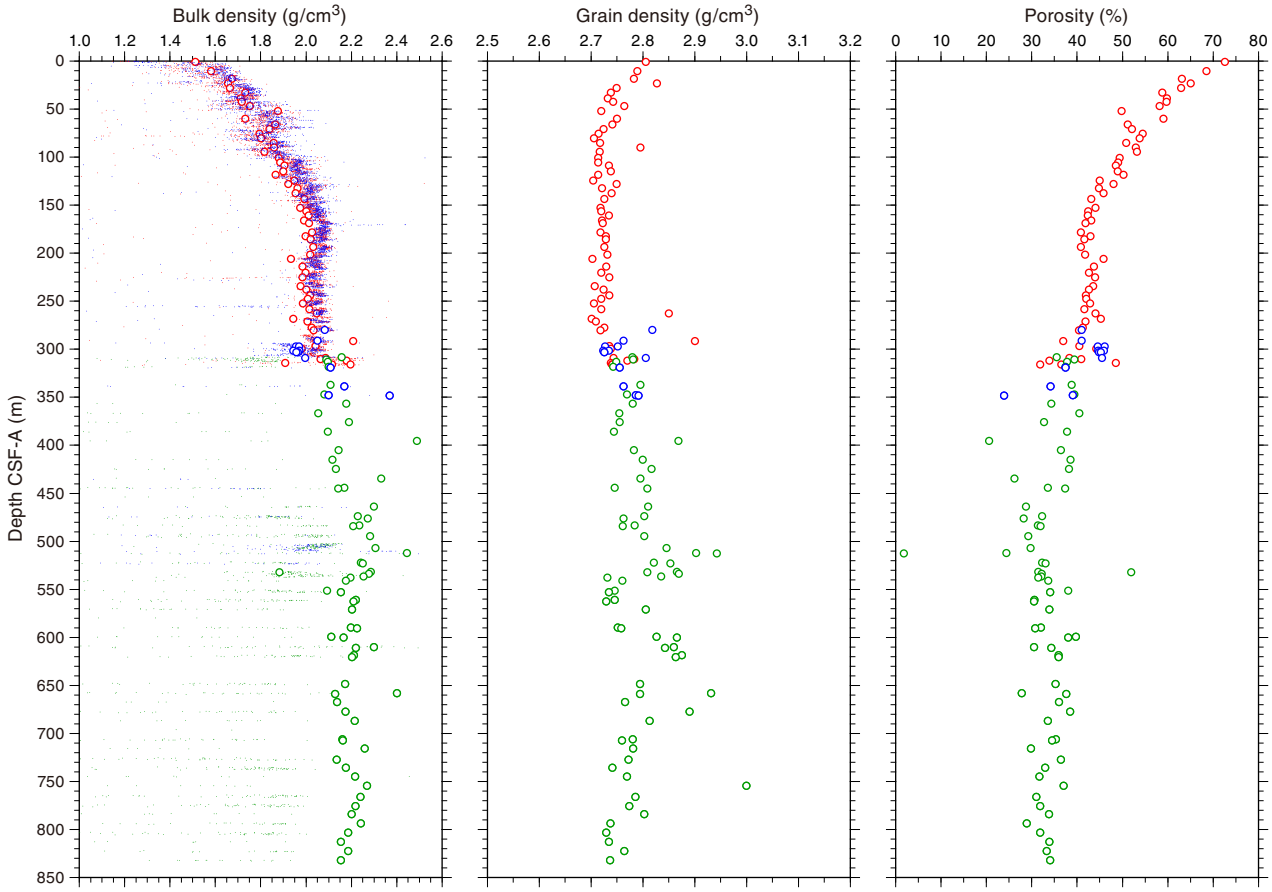

ogy that require application of a range of mineralogy-dependent GRA coefficients (μ):

$$\rho = [\ln(Y_t/Y_i)]/\mu d,$$

where Y_t is the gamma radiation transmitted through the sample, Y_i is the emitted gamma radiation, and d is the thickness of the sample. During shipboard GRA analyses, μ is assumed to be constant. However, μ depends on mineralogy and, therefore, this assumption generates errors up to 5% (Blum, 1997). This is consistent with the percent difference between bulk densities measured by GRA and by MAD methods observed at these two sites. This difference shows a somewhat inverse trend with grain density (Figure **F30A–F30B**), which supports the contention that the mismatch between the two measures of bulk density has its origin in the mineralogy of the sediments. That is, when grain densities are high, GRA underestimates bulk density, whereas for lower grain density material, GRA tends to overestimate bulk density. However, the percent difference in the top 50–100 m at both sites shows that the GRA bulk density estimates are not consistently lower than MAD bulk density values, whereas the grain densities are consistently high in this depth range. This points to the fact that μ is mineral-dependent, and different minerals or mixtures of minerals may have the same grain densities. As a result, there is no correlation between grain density and the difference between GRA and MAD estimates of bulk density. However, there is a correlation between GRA and MAD estimates of bulk density, which is high with a slope of 1.08 (at Site U1464) and a correlation coefficient (R^2) of 0.905 (Figure **F30C**).

The grain density is about 2.8 g/cm³ at the seafloor, decreases to about 2.72 g/cm³ at 80 m CSF-A, and then remains fairly constant at about 2.72 ± 0.01 g/cm³ (Figure **F29**). Between 300 and 317 m CSF-A, grain densities shift to higher values and range from 2.74 to 2.79 g/cm³ in both Holes U1464B and U1464C. Deeper, grain densities remain at higher levels and range between about 2.74 and 2.85 g/cm³ with a few higher values resulting from sampling minor lithologies and ranging up to 2.99 g/cm³.

Porosity at the seafloor was observed to be 72.6%, and it decreases exponentially to about 41% at ~200 m CSF-A. From 200 to 300 m CSF-A, porosity is fairly constant, with a range of about 40%–46% (Figure **F29**). From 300 to 317 m CSF-A, there is a wide range of porosities, although on average porosities are about 35%. Deeper, porosity remains variable with a decreasing trend to 25% at 510 m CSF-A. From that depth to the bottom of Hole U1464C (840 m CSF-A), porosity remains fairly constant, varying between 30% and 40%, although a few outliers are observed. These outliers are related to minor lithologies like anhydrite with 1.8% porosity and a grain density of 2.94 g/cm³ (Sample 356-U1464C-23R-2, 21.0 cm; 312.65 m CSF-A). Another sample at 532 m CSF-A (Sample 25R-2, 31.0 cm) included organic material with high porosity and anhydrite cements resulted in a relatively high grain density of 2.81 g/cm³.

The high variability in grain density, bulk density, and porosity that is observed in Hole U1464C corresponds to the highly variable

Figure F30. (A) MAD grain density compared to (B) the percent difference between bulk density, as measured by GRA and as measured by MAD. C. Correlation between bulk density, as measured by GRA and as measured by MAD (R^2 = 0.905 for Site U1464 data).

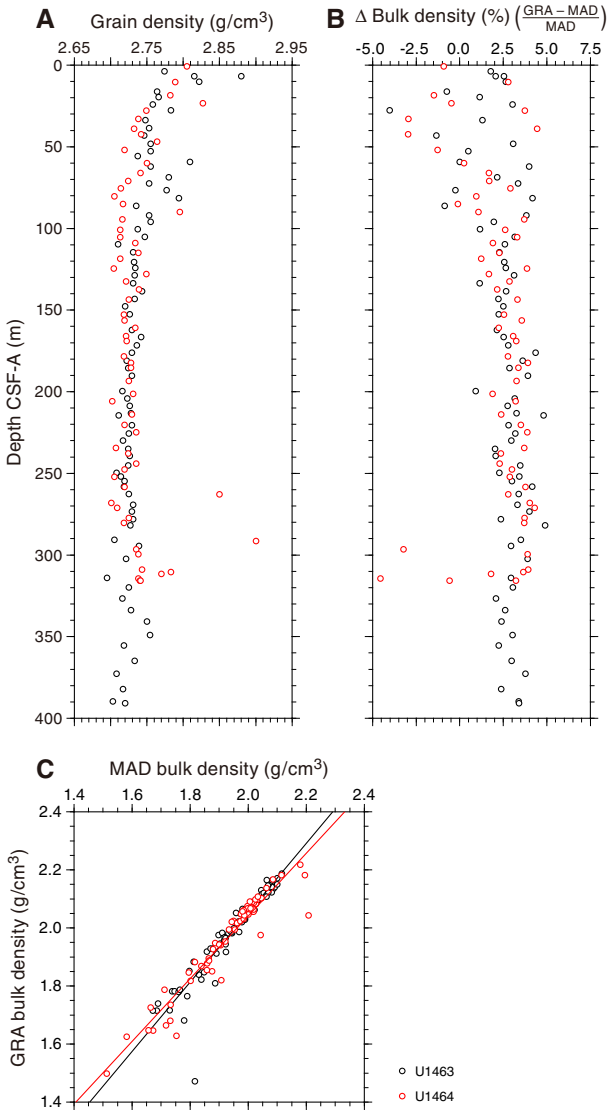

P-wave velocities that are observed at the same depths. In fact, the highest velocity region that runs from 390 to 520 m CSF-A is at the same depth as the lowest porosities observed at this site (~30%). Indeed, this interval contains anhydrite, characterized by porosity as low as 1.8%.

Discrete stress measurement

Discrete measurements of shear and normal stress were taken in Hole U1464B. The measurements were taken at a rate of one per core where the sediments were soft enough to use the handheld Torvane and the pocket penetrometer (0–190 m CSF-A). Normal strength increases up to ~300 N/m² at 190 m CSF-A. Shear strength also increases to ~600 N/m² at 190 m CSF-A (Figure **F31**).

Reflectance spectroscopy and colorimetry

Reflectance spectroscopy and colorimetry was performed on the archive halves of the split core sections at 2.5 cm intervals. Reflectance (L*), red versus green (a*), and blue versus yellow (b*) were measured on all cores. In Holes U1464B and U1464D, a general decrease is observed in both L* and a* from 0 to 200 m CSF-A. From 200 to 317 m CSF-A, L* remains constant at about 45%, whereas a* increases from –0.5 to 0.5 (Figure **F32**). In Holes U1464C and U1464D deeper than 320 m CSF-A, all the colorimetry parameters show high variance in agreement with the lithologic variability observed in these holes.

Figure F31. Penetrometer strength and shear strength results, Hole U1464B.

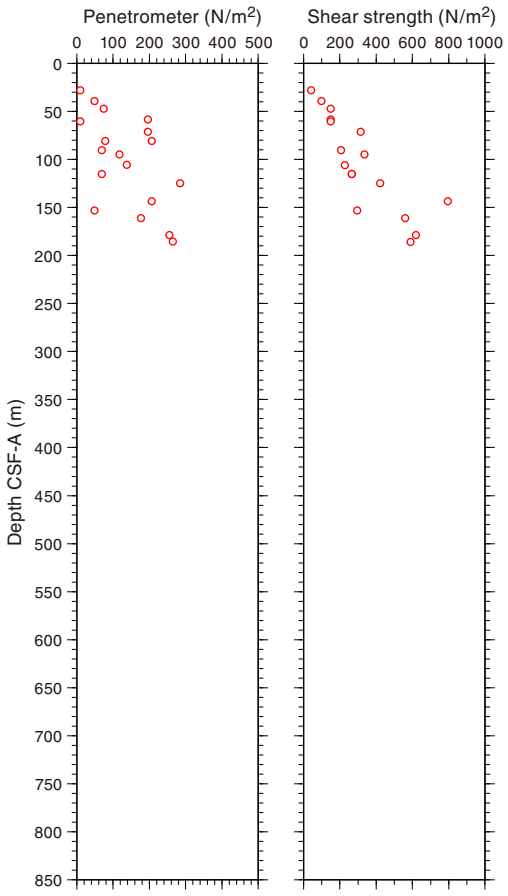

Thermal conductivity, temperature, and heat flow

Thermal conductivity was measured in Holes U1464B–U1464D using two different devices. We used the needle shallower than 160 m CSF-A in Hole U1464B and 232 m CSF-A in Hole U1464D and the minipuck deeper in Holes U1464B–U1464D. Thermal conductivity increases from 0.94 W/(m·K) at the seafloor to 2.4 W/(m·K) at 500 m CSF-A. In the deeper portion of Hole U1464C from 720 to 800 m CSF-A, thermal conductivity ranges from 1.6 to 1.85 W/(m·K) (Figure **F33D**).

We measured in situ temperatures with the APCT-3 during piston coring in Hole U1464D. Measurements were made in Cores 356-U1464D-5H, 8H, 12H, 16H, 22H, and 28H. We were not able to estimate the temperature at the seafloor with confidence from the temperature logs. The shallowest estimate of temperature was at 41.85 m CSF-A (15.97°C). The deepest temperature reading was taken at 256.61 m CSF-A (25.55°C) (Figure **F33A**). Inspection and extrapolation of these temperature records suggest that they are all

Figure F32. Reflectance spectroscopy and colorimetry (L*, a*, and b*), Site U1464.

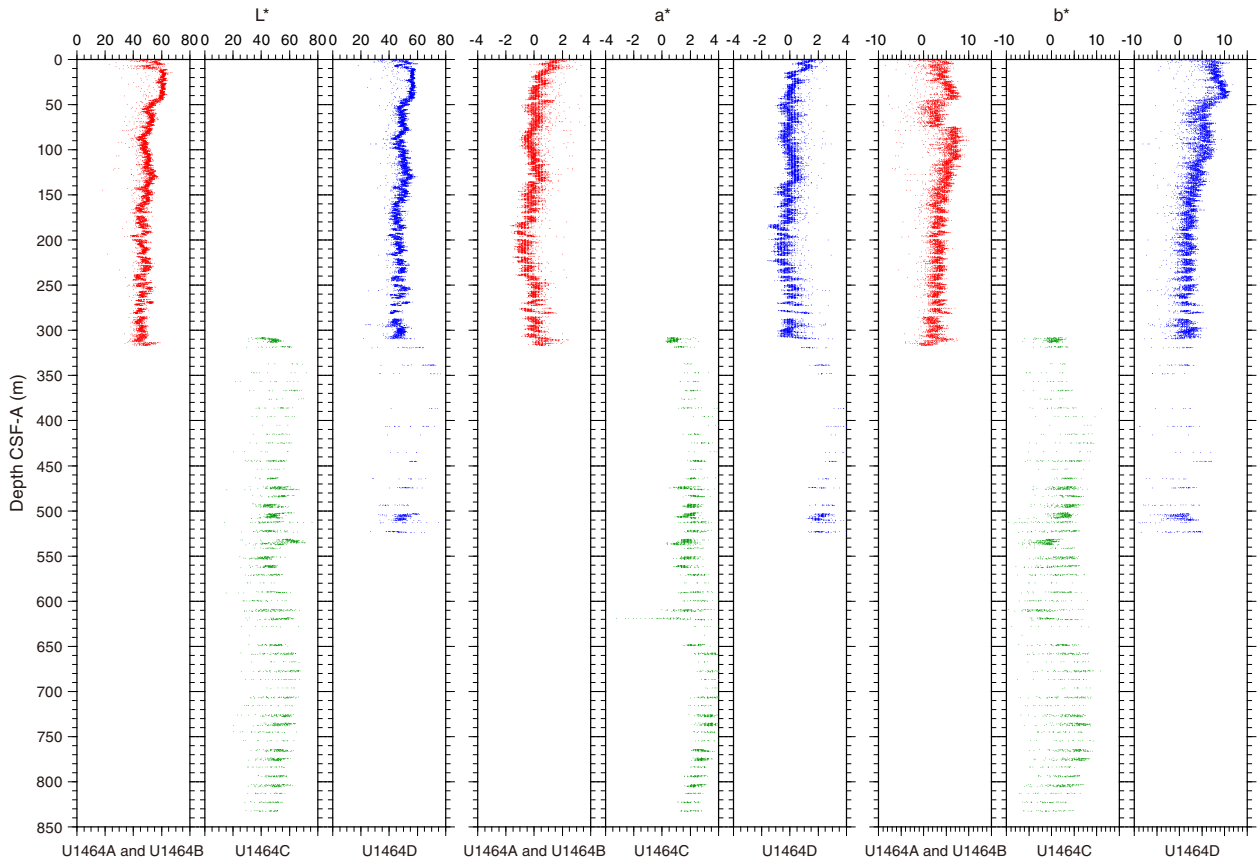

of good to excellent quality. The shallowest temperature estimate in Core 5H (41.85 m CSF-A) showed some heating before the major jump associated with firing of the piston core into the sediments. The temperature measurements define a geothermal gradient with little deviation from linearity. The resulting gradient is 44.9°C/km. From the thermal conductivities measured in cored material (Figure **F33B**), we were able to estimate a geothermal heat flux of 59.1 mW/m^2. The Bullard plot shows a linear relationship between temperature and thermal resistance (Figure **F33C**) (see **Physical properties** in the Expedition 356 methods chapter [Expedition 35 Scientists, 2017a]). Therefore, we are confident that the temperature profile has not been perturbed by fluid flow or internal heat production.

Figure F33. A. In situ temperatures measured with the APCT-3, Hole U1464D. B. Thermal conductivity (*k*) measured on Hole U1464B–U1464D cores and used in heat flow calculation. C. Thermal resistance (Ω) vs. temperature (*T*) (Bullard plot). D. Thermal conductivity as measured throughout the entire cored interval. In B and D, only data with standard deviations <0.1 W/(m·K) are shown. The width of the symbol indicates standard deviation of each measurement and red = Hole U1464B, blue = Hole U1464C, black = Hole U1464D.

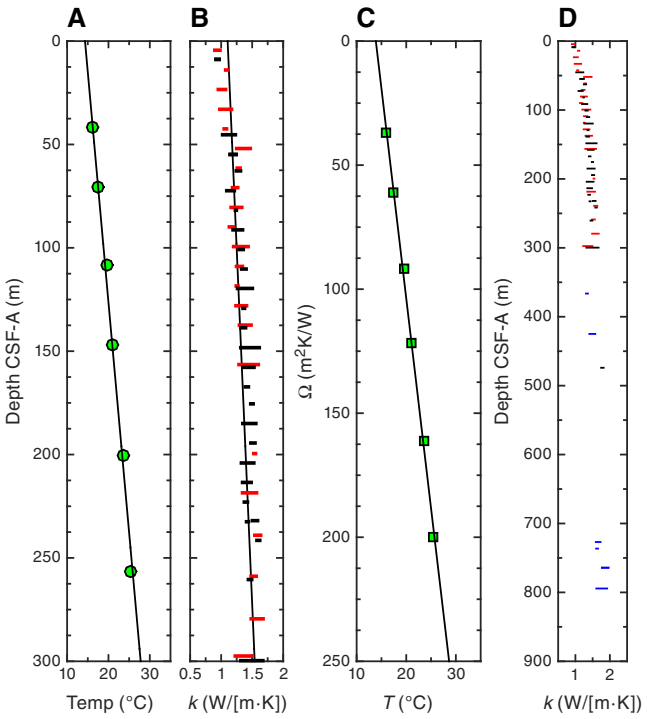

Downhole measurements

Downhole measurements were conducted in Hole U1464C with the triple combo tool string. The tool became stuck in the hole at 615 m wireline log matched depth below seafloor (WMSF) on the first up pass, probably due to hole cave in, and considerable effort was undertaken to retrieve the tool (see **Operations**). Despite this, the triple combo tool string measured total spectral gamma ray (HSGR), MS, and resistivity throughout the hole (0–783 m WMSF) during the down pass and between 783 and 615 m WMSF during the up pass. Bulk density and porosity were only obtained during the up pass. Logging runs with the Formation MicroScanner (FMS)-sonic and Versatile Seismic Imager (VSI) were not conducted because of the condition of the hole following the recovery of the triple combo. The HSGR log was in good agreement with NGR data from cores (see **Physical properties**), allowing correlation of wireline to core data. MS measurements were affected by temperature and were judged to be of insufficient quality for interpretation. Wireline bulk density and porosity measurements corresponded to the results of discrete sampling in cores in most of the limited interval logged with those tools. Six APCT-3 in situ temperature measurements were made in Hole U1464D.

Depth matching

The depth scales of the preprocessed logs were first shifted to make them relative to the seafloor (–276 m), which was determined by the step in HSGR observed on the triple combo main run. This differed by 0.7 m from the calculated seafloor depth of 275.3 meters below rig floor (mbrf) determined by the drillers. Based on the correlation of distinct features between the wireline HSGR record and NGR as measured on cores (see below), we observed a 0–4 m discrepancy between core depths (CSF-A) and wireline logging depths (WMSF). In the discussion below, we refer to all logs in WMSF and all cores in CSF-A, realizing that the match between the two is only approximate within several meters.

Natural gamma radiation

HSGR was measured both during the down pass and shortened up pass with the triple combo tool string. Because of hole collapse at 615 m WMSF, the data obtained from the down pass covered a larger depth interval than the up pass. We only present down pass data because the data from the up and down passes were similar in the overlapping interval (Figure **F34**). The HSGR log showed good agreement with the composite NGR data obtained on whole-round cores at this site. Between the seafloor and the end of the drill pipe (84 m WMSF), the wireline HSGR measurements are attenuated. Nevertheless, wireline HSGR in this interval also shows the three distinct peaks in NGR that were observed in cores at 8, 25, and 45 m CSF-A. Between 84 and 305 m WMSF, wireline HSGR ranges between 25 and 55 American Petroleum Institute gamma radiation units (gAPI). The relatively large variability in this interval is the result of variability in potassium (K) and thorium (Th), whereas the signal from uranium (U) was subdued. However, the large peak in core-based NGR observed at 309 m CSF-A and in HSGR at 305 m WMSF is the result of a peak in U concentration. Between 305 m WMSF and the bottom of the hole (747 m WMSF), HSGR is generally lower than in the overlying interval and ranges between 15 and 40 gAPI. However, a few HSGR peaks exceed this range and are as high as 52 gAPI. HSGR variability in this interval is primarily the result of variations in U, rather than variation in K or Th, both of which show generally low concentrations.

As mentioned above, some features in the wireline HSGR records from Hole U1464C were also observed in NGR on cores from this site. Four of the most robust core-log correlations are indicated by horizontal gray lines on Figure **F34**, all consisting of distinctive gamma ray peaks. The correlation of these features indicates that the wireline depth is consistently shallower than the cored depth. The offset between wireline and coring depths varied between 0 and 4 m.

Magnetic susceptibility

MS was measured during downhole logging with the triple combo in Hole U1464C. Similar to what was observed during downhole logging at IODP Sites U1461–U1463, the wireline MS measurements were affected by temperature (see **Downhole measurements** in the Site U1461 chapter, **Downhole measurements** in the Site U1462 chapter, and **Downhole measurements** in the Site U1463 chapter [Gallagher et al., 2017b, 2017c, 2017d]). This resulted in wireline MS measurements that were not comparable to MS data measured on cores. This effect was not corrected for during processing. Therefore, the wireline MS data were judged to be of insufficient quality for interpretation.

Porosity, density, and resistivity

We measured porosity and density with the triple combo tool string (Figure **F35**). Bulk density was measured with the Hostile En-

Figure F34. Hole U1464C diameter (caliper; only available from shortened up pass) and HSGR measured by triple combo, NGR from Hole U1464B–U1464D whole-round cores, and elemental uranium, thorium, and potassium concentrations estimated from Hole U1464B HSGR spectra.

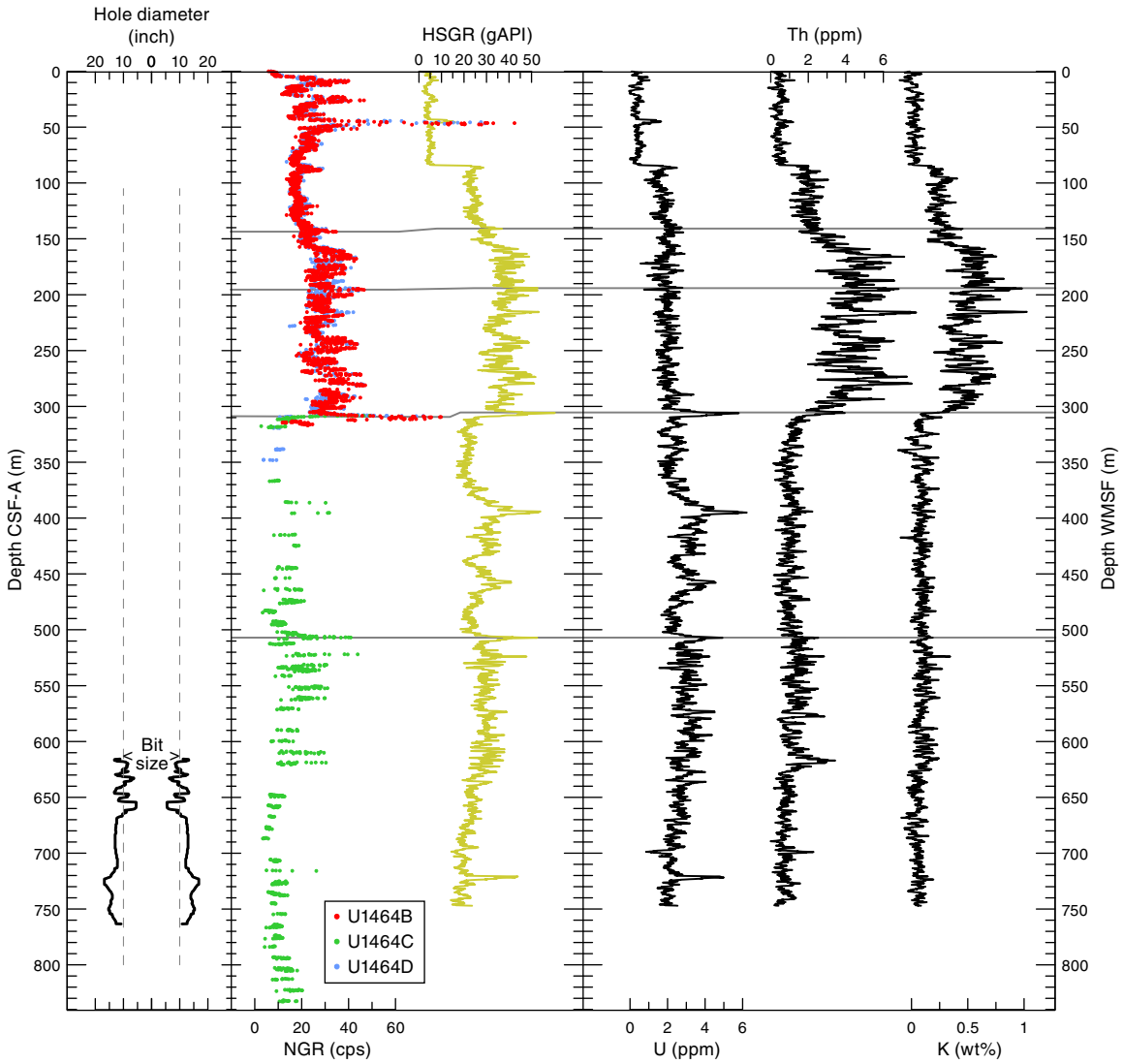

vironment Litho-Density Sonde (HLDS) between 617.67 and 763.67 m WMSF, and porosity was measured with the Accelerator Porosity Sonde (APS) between 617.52 and 756.20 m WMSF. The results were judged to be of reasonable quality, based on the systematic variation in the logs, standoff distance (STOF) of the APS tool (the distance between the tool and wall inferred from the APS tool signal), and consistency with the discrete MAD measurements on Hole U1464C cores. In order to visualize the average trend of the wireline porosity and bulk density logs, we smoothed these properties over ~25 m, whereas the noisier APS STOF was smoothed over ~50 m. Wireline-inferred bulk density ranges between 2 and 2.25 g/cm^3 over the logged interval, generally consistent with the MAD-inferred values. From 664 to 660 m WMSF, the wireline-inferred bulk density systematically decreases uphole to ~1.75 g/cm^3 in contrast to the MAD-inferred values, which are high in this interval. Although STOF was low at this point and the caliper was fully closed, both suggesting a constricted borehole in this same interval, we inferred that the tool was not able to make good contact with the wall.

Porosity measured by the APS tool, and corrected assuming that the material is limestone, starts at ~50% at 620 m WMSF and drops to ~35% at 750 m WMSF. Only between 680 and 720 m WMSF and between 735 and 755 m WMSF are the logging-inferred values consistent with the MAD-inferred values. Between 720 and 735 m WMSF, the wireline porosity data deviate substantially from values above and below this interval. Porosity could not be inferred correctly in this interval because of the width of the borehole (larger than the caliper can measure) and because of the large STOF (Figure **F35**).

In situ temperature

In situ temperature measurements were made in Hole U1464D using the APCT-3 in Cores 356-U1464D-5H, 8H, 12H, 16H, 22H, and 28H. The temperature logs are described and interpreted in **Physical properties**.

Figure F35. Hole U1464C diameter (caliper; black) and smoothed standoff distance (×10; blue) inferred from APS on triple combo and bulk density and porosity (lines = smoothed Hole U1464C wireline HLDS/APS, circles = Hole U1464C discrete MAD measurements).

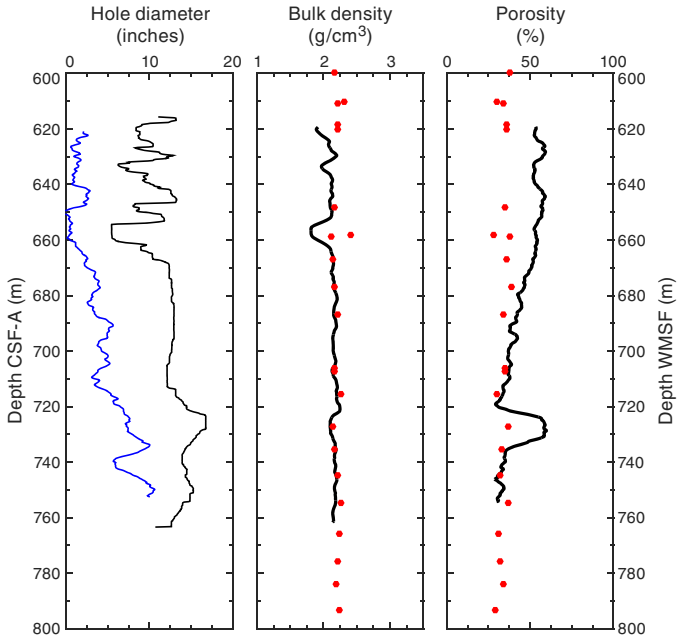

Stratigraphic correlation

Site U1464 was cored to ~840 m CSF-A using a combination of the APC, XCB, and RCB systems. The upper ~300 m was double cored with the APC system (Holes U1464B and U1464D), and a strong correlation was produced using the NGR data. The correlation was extended to ~320 m CSF-A using the APC (Hole U1464B) and XCB systems (Hole U1464D) but is less certain because of recovery gaps and biscuiting in the XCB cores. A splice could not be created because there were only two holes in the uppermost sections, but the correlation should be useful as sampling guidance for most paleoceanographic studies, particularly because sedimentation rates are elevated (17 cm/ky) in the expanded early Pliocene section that ranges from ~320 to 180 m CSF-A in Holes U1464B and U1464D.

Guidance for coring (using CSF-A)

Cores were measured for MS and GRA on the Special Task Multisensor Logger immediately after recovery at 10 cm intervals. The results were used to monitor for coring gaps in real time, and adjustments were made in Core 356-U1464D-19H, which was advanced by recovery to avoid repeating recovery gaps in cores downhole.

Correlation of the cores (to produce CCSF-A)

There were only two holes cored with the APC system; therefore, the aim was not to produce a splice but to correlate the cores so that sampling could occur without recovery gaps in the section. Both APC Holes U1464B and U1464D had good recovery down to Cores 356-U1464B-17H and 356-U1464D-17H (~155 m CSF-A). Deeper, core recovery varied from 70% to 90% in Hole U1464B and 39% to 103% in Hole U1464D. Both holes were mainly advanced by 9.7 m (the length of a full core using any of the coring systems) rather than by recovery. This resulted in large gaps in the downhole record of both holes when recovery was <100% and prevented generation of a splice. Nonetheless, correlation of the holes was possible with only a few intervals of uncertainty (Table **T16**; Figure **F36**).

Table T16. Affine table, Site U1464. **Download table in .csv format.**

Correlation was based primarily on NGR data because the variability in MS was particularly low, especially in the depth interval with the best recovery (0–155 m CSF-A). Nevertheless, in cases of uncertainty the MS patterns were used to improve the correlation. For example, in Core 356-U1464B-14H (120 m CSF-A) (Figure **F36B**) there is a large increase in NGR values at the boundary between Sections 3 and 4 (from 17–19 counts/s in Section 14H-3 to 26 counts/s in Section 14H-4). The peak is not present in Hole U1464D, nor is it found in MS in either hole.

Correlation to ~170 m CSF-A (Cores 356-U1464B-19H and 356-U1464D-19H) is robust (Figure **F36A–F36C**). Deeper than 170 m CSF-A, uncertainty is high as a result of limited overlap between cores and large recovery gaps (Figure **F36C–F36D**). Patterns in NGR and MS are consistent between the two holes but the gaps make absolute correlations equivocal. This interval of uncertainty begins with Core 356-U1464D-20H, which had to be appended below Core 356-U1464D-19H. Good correlations could be made below Core 356-U1464D-20H, between 195 and 218 m CCSF-A (Cores 356-U1464B-22H, 356-U1464D-22H, 356-U1464B-23H, and 356-U1464D-23H), resulting in a 23 m interval that is appropriate for continuous sampling.

Hole and site summaries (sedimentation rates)

A summary of the relationship between MS and NGR (see **Physical properties**), biostratigraphic, lithostratigraphic (see **Biostratigraphy and micropaleontology** and **Lithostratigraphy**), and magnetostratigraphic (see **Paleomagnetism**) data is shown on Figures **F37**, **F38**, and **F39**. Sedimentation rates calculated from biostratigraphic datums (see **Biostratigraphy and micropaleontology**) are presented graphically for Holes U1464B–U1464D (Figures **F37**, **F38**, **F39**) and Site U1464 (Figure **F40**). Sedimentation rates were calculated assuming a linear sedimentation rates between datums (in centimeters per thousand years and using the CSF-A depth scale).

Sedimentation rates are not detailed for the Miocene interval (Figures **F38**, **F39**, **F40**) because only three datums were identified in an interval of over 500 m of low core recovery. However, assuming deposition was continuous between the LBF datum at 707.57 m CSF-A and the nannofossil horizon at 552.5 m CSF-A (Figure **F38**), sedimentation was in the range of 25–30 cm/ky in the Miocene interval. However, the LBF datum represents the youngest possible age for 707.57 m CSF-A; if the horizon is older, Miocene sedimentation rates would be lower.

Biostratigraphy indicates an expanded lower Pliocene section. Pliocene sedimentation rates increase from ~1.5 cm/ky in the lower Zone NN12–NN13 to 17 cm/ky in the upper Zone NN12–NN13 and Zone NN14–NN15 (Figure **F37**). Sedimentation rates are elevated (5–8 cm/ky) through the remainder of the Pliocene (Zone NN16) and into the Pleistocene. Upper Pleistocene (Zone NN19-NN21) rates are similar but vary depending on the biostratigraphic group (nannofossils yield a rate of ~2 cm/ky and planktonic foraminifers yield ~4 cm/ky).

Figure F36. Correlation of the upper ~300 m CSF-A from Holes U1464B and U1464D. Solid lines = points of correlation between holes, dashed lines = some uncertainty in the correlation. A. 0–75 m CSF-A. B. 75–150 m CSF-A. (Continued on next page.)

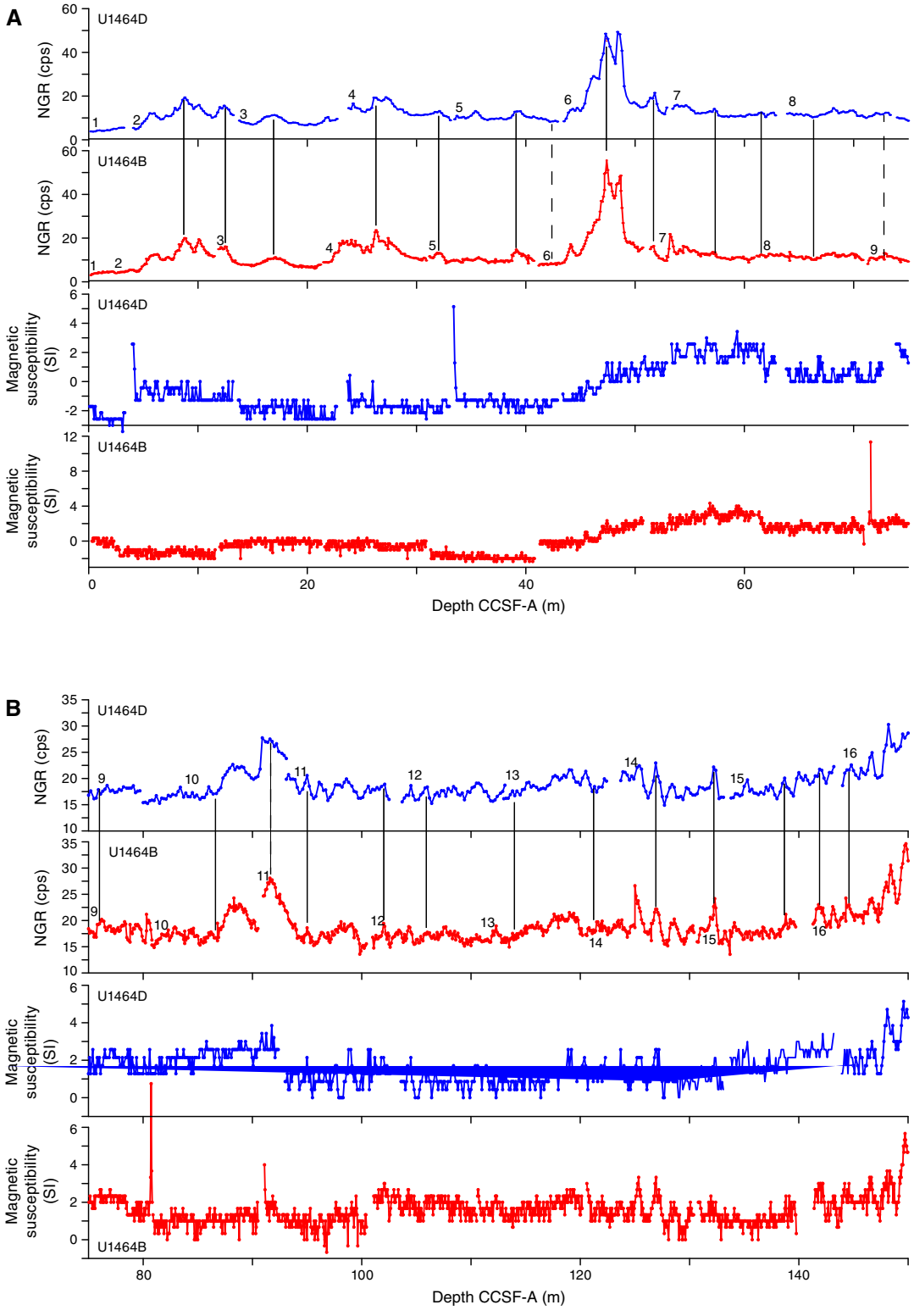

Figure F36 (continued). C. 150–225 m CSF-A. D. 225–300 m CSF-A. D. 225–300 m CSF-A.

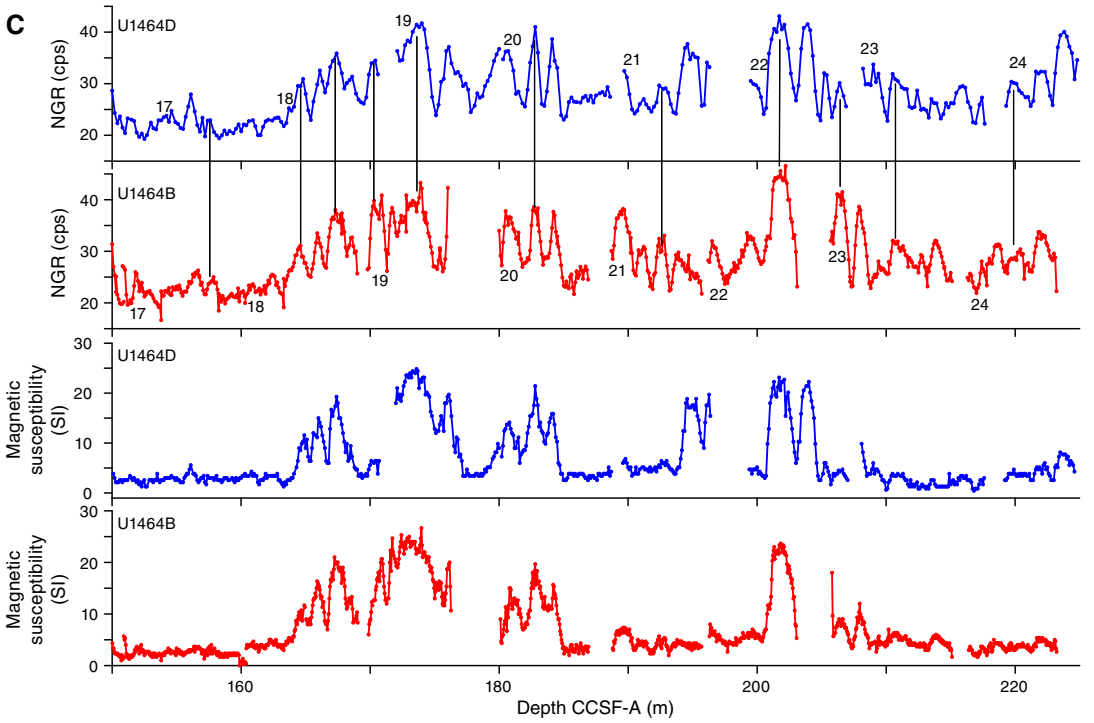

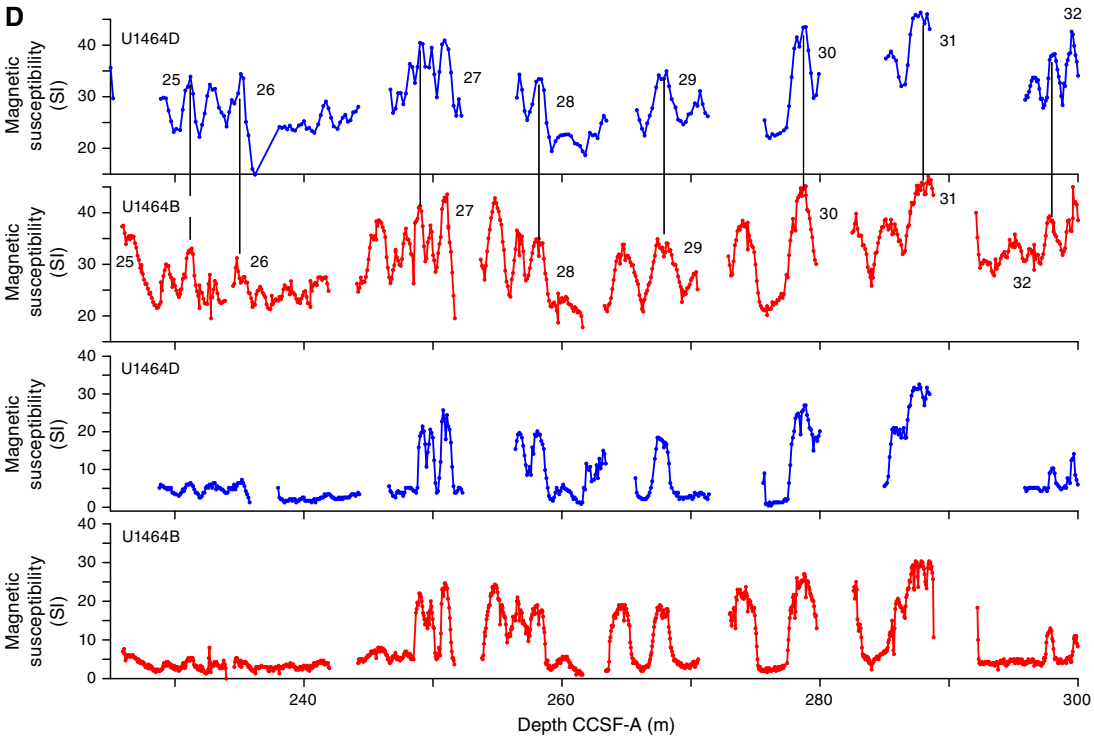

Figure F37. Hole U1464B summary showing core recovery, graphic lithology, lithostratigraphic units, age, and biostratigraphic data plotted against MS and NGR. Biostratigraphic zone boundary ages are shown. Age-depth model was produced from biostratigraphic datums only (see **Biostratigraphy and micropaleontology**) and assumes a linear sedimentation rate between datums (solid circles = calcareous nannofossils, open circles = planktonic foraminifers). Sedimentation rates are calculated separately for calcareous nannofossils (NN) and planktonic foraminifers (PF) where the datums diverge. Gray shading in PF zone indicates stratigraphic uncertainty. See Figure **F7** in the Expedition 356 methods chapter (Gallagher et al., 2017a) for lithology key. BF = benthic foraminifer. IS = inner shelf, MS = middle shelf, OS = outer shelf, UB = upper bathyal.

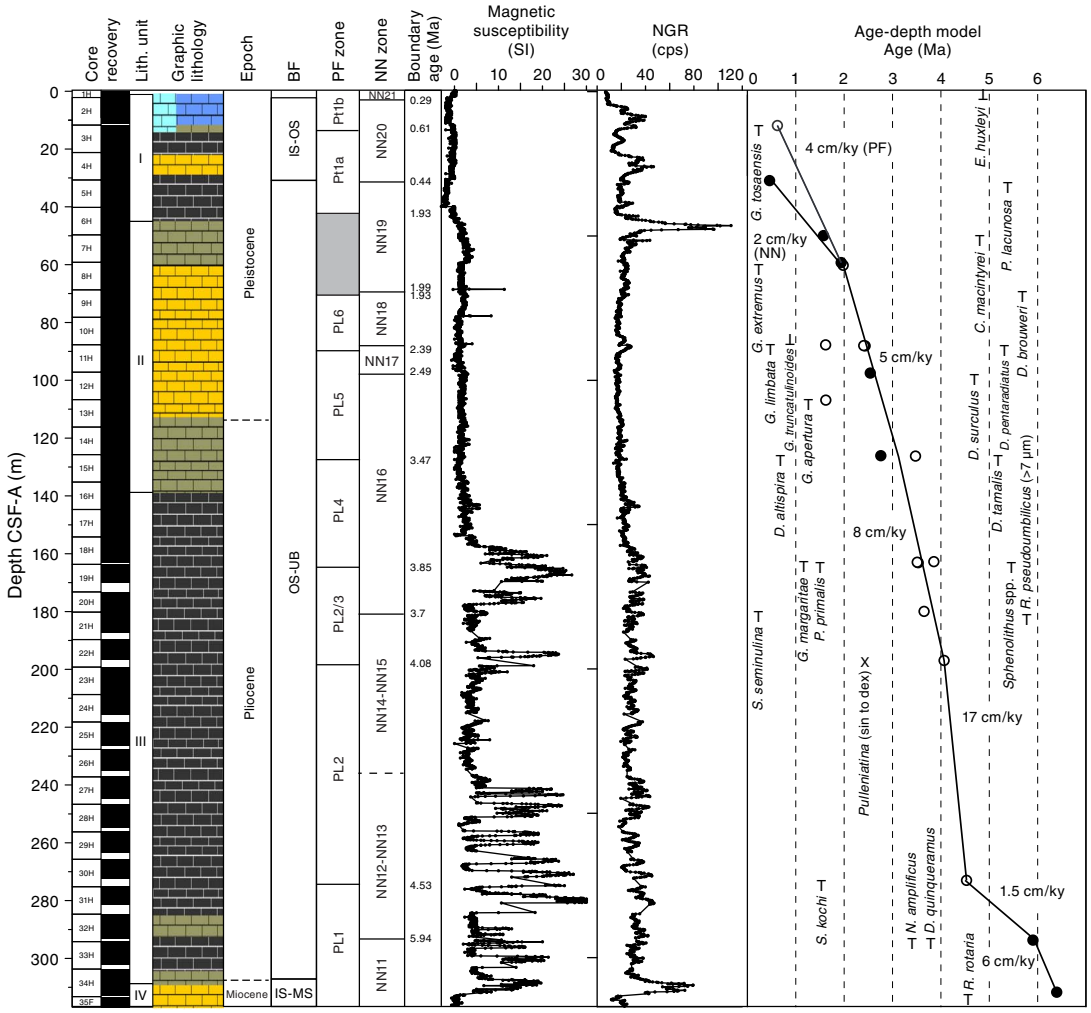

Figure F38. Hole U1464C summary showing core recovery, graphic lithology, lithostratigraphic units, age, and biostratigraphic data plotted against MS and NGR. Age-depth model was produced from biostratigraphic datums only (see **Biostratigraphy and micropaleontology**); a linear sedimentation rate may be assumed in this interval but is not plotted (see text for details and resulting sedimentation rate estimates). Solid circles = calcareous nannofossils, open square = benthic foraminifer. See Figure **F7** in the Expedition 356 methods chapter (Gallagher et al., 2017a) for lithology key.

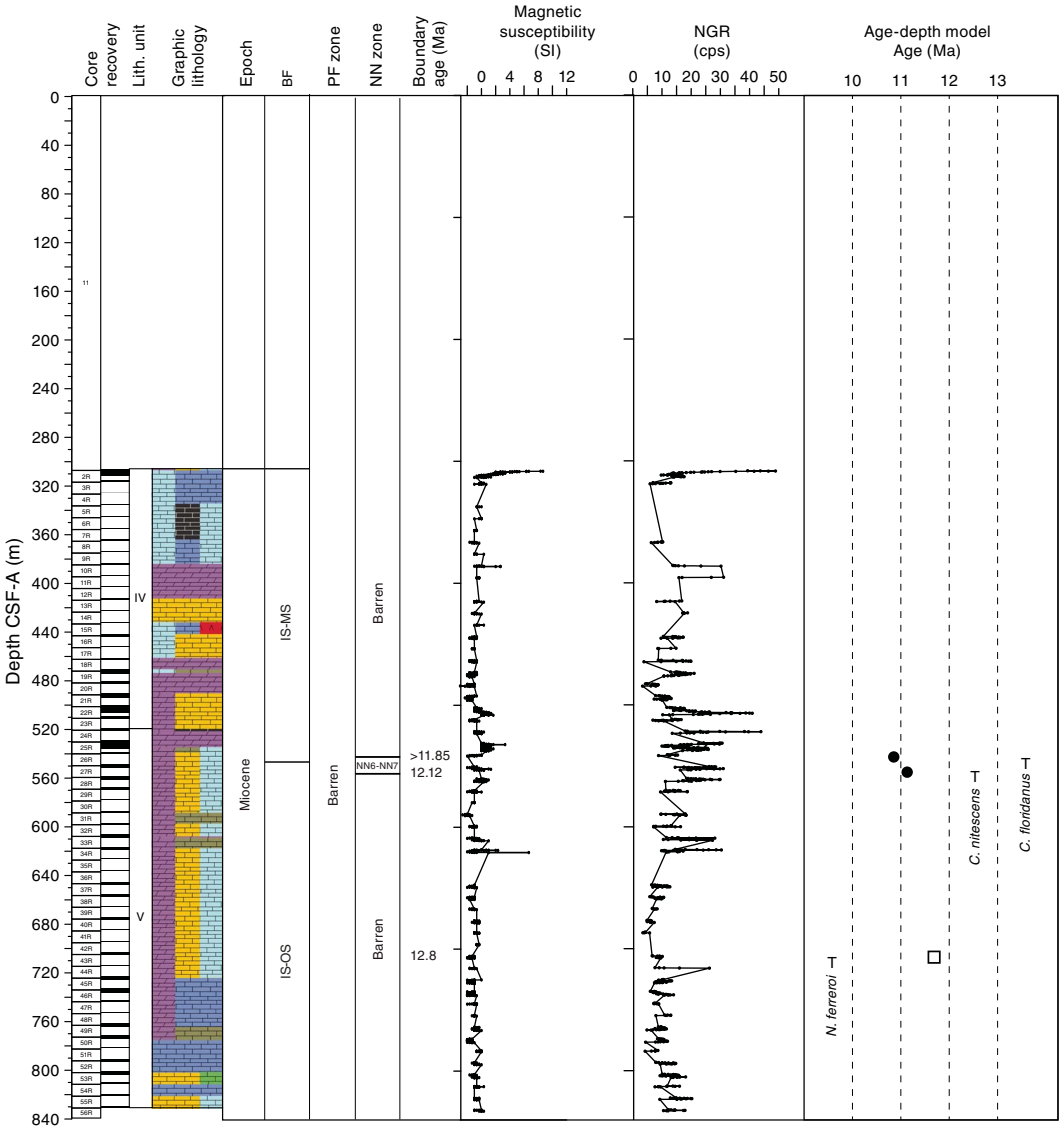

Figure F39. Hole U1464D summary showing core recovery, graphic lithology, lithostratigraphic units, age, and magnetostratigraphic and biostratigraphic data plotted against MS and NGR. Polarity is shown in black and white, gray intervals = uncertainty in the data (see **Paleomagnetism**). Biostratigraphic zone boundary ages are shown. Age-depth model was produced from biostratigraphic datums only (see **Biostratigraphy and micropaleontology**) and assumes a linear sedimentation rate between datums (solid circles = calcareous nannofossils, open circle = planktonic foraminifers). See Figure **F7** in the Expedition 356 methods chapter (Gallagher et al., 2017a) for lithology key.

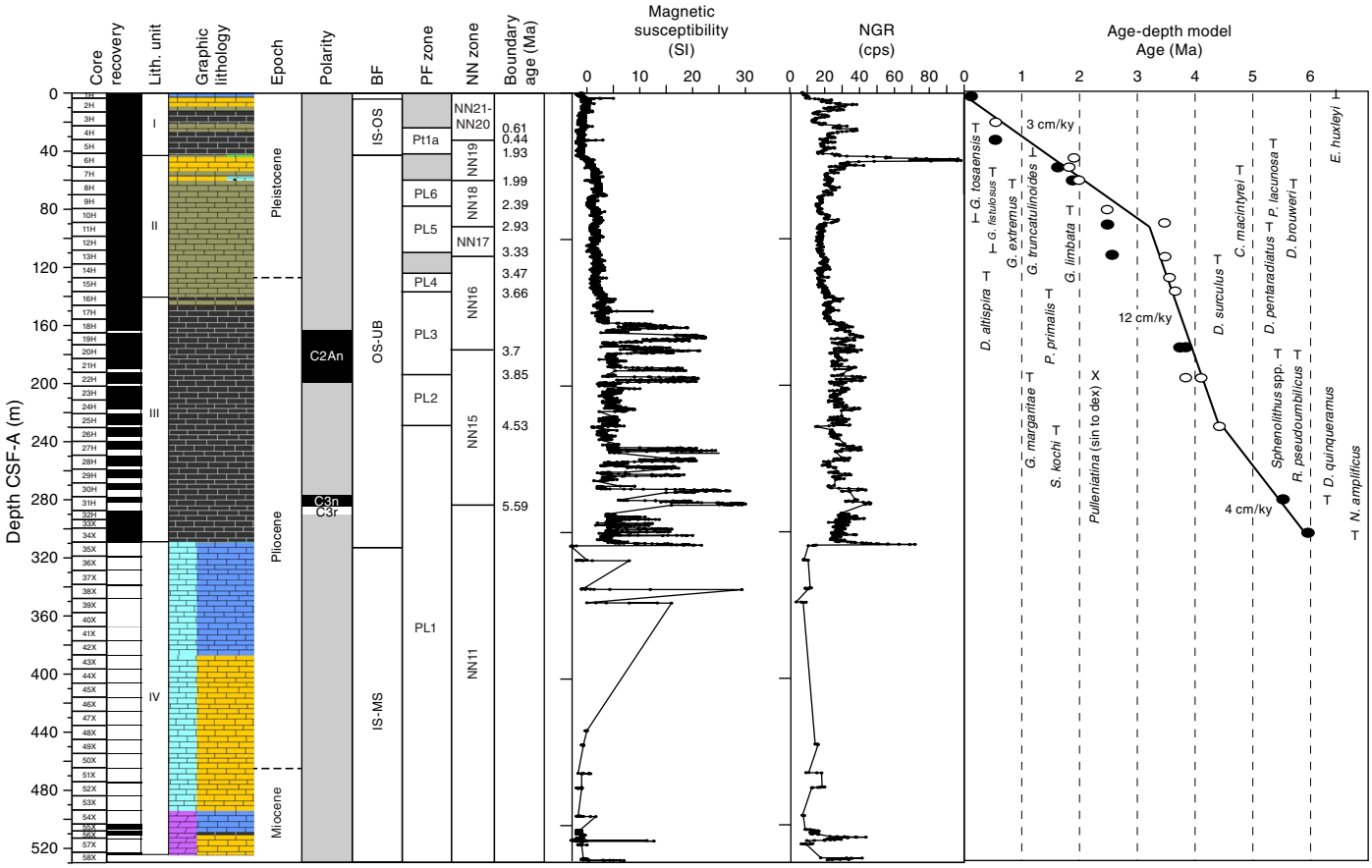

Figure F40. Site U1464 summary showing core recovery, graphic lithology, lithostratigraphic units, age, magnetostratigraphy, biostratigraphy, and NGR. Magnetic polarity is shown in black and white, gray intervals = uncertainty in the data (see **Paleomagnetism**). Biostratigraphic zone boundary ages are shown. Age-depth model was produced from biostratigraphic datums only (see **Biostratigraphy and micropaleontology**) and assumes a linear sedimentation rate between datums (solid circles = calcareous nannofossils, open circle = planktonic foraminifers, open square = benthic foraminifer). Sedimentation rates are calculated separately for calcareous nannofossils and planktonic foraminifers where the datums diverge. Note the break in horizontal scale for the age-depth model. Benthic foraminiferal assemblages were smoothed to generate this synthesis, resulting in slight differences from data presented in hole summaries.

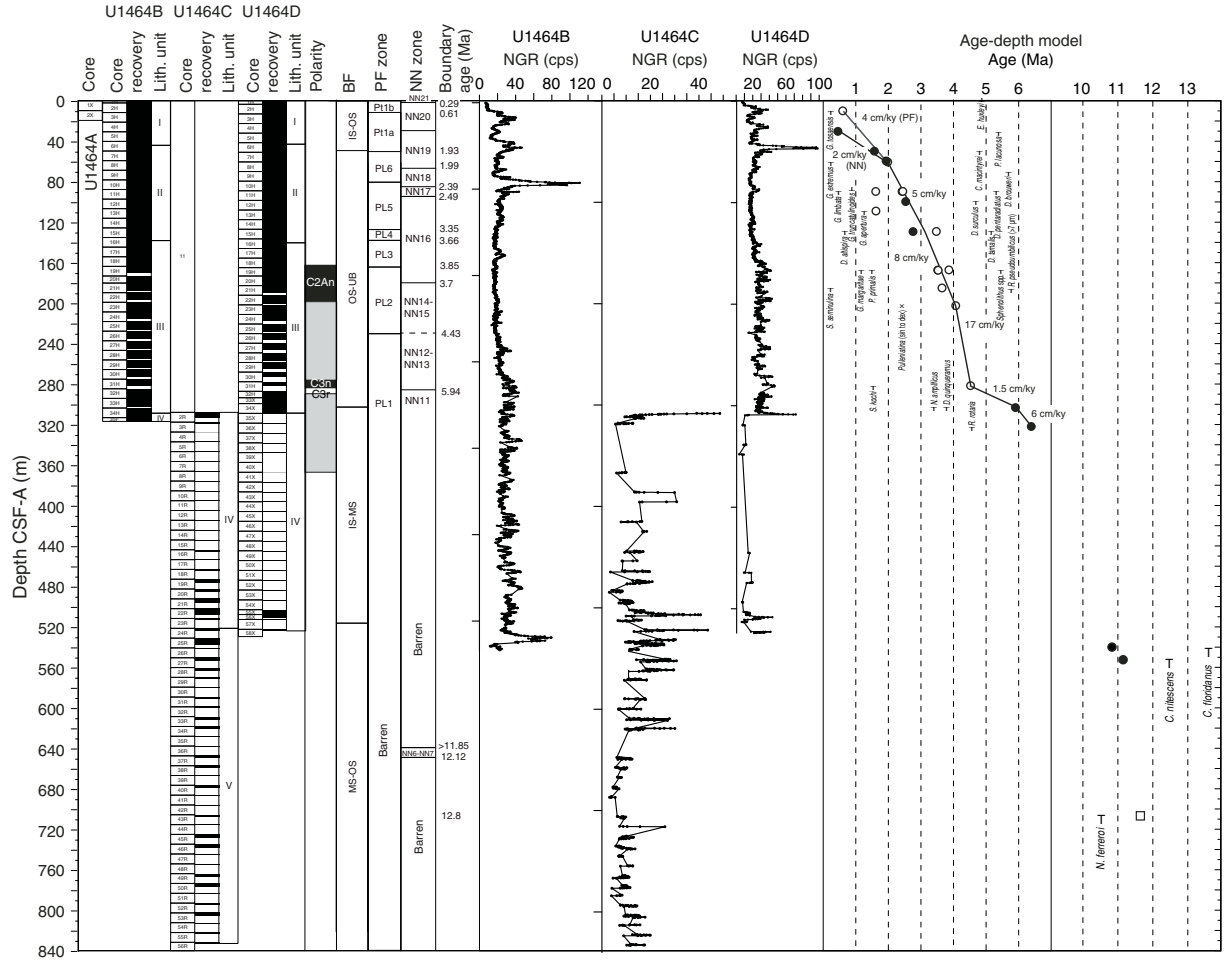

References

Blum, P., 1997. *Technical Note 26: Physical Properties Handbook—A Guide to the Shipboard Measurement of Physical Properties of Deep-Sea Cores*. Ocean Drilling Program. **http://dx.doi.org/10.2973/odp.tn.26.1997**

Debenay, J.-P., and Payri, C.E., 2010. Epiphytic foraminiferal assemblages on macroalgae in reefal environments of New Caledonia. *Journal of Foraminiferal Research,* 40(1):36–60. **http://dx.doi.org/10.2113/gsjfr.40.1.36**

Dunlop, D.J., and Özdemir, Ö., 1997. *Cambridge Studies in Magnetism* (Volume 3): *Rock Magnetism: Fundamentals and Frontiers:* Cambridge, United Kingdom (Cambridge University Press).

Gallagher, S.J., Fulthorpe, C.S., Bogus, K., Auer, G., Baranwal, S., Castañeda, I.S., Christensen, B.A., De Vleeschouwer, D., Franco, D.R., Groeneveld, J., Gurnis, M., Haller, C., He, Y., Henderiks, J., Himmler, T., Ishiwa, T., Iwatani, H., Jatiningrum, R.S., Kominz, M.A., Korpanty, C.A., Lee, E.Y., Levin, E., Mamo, B.L., McGregor, H.V., McHugh, C.M., Petrick, B.F., Potts, D.C., Rastegar Lari, A., Renema, W., Reuning, L., Takayanagi, H., and Zhang, W., 2017a. Expedition 356 methods. *In* Gallagher, S.J., Fulthorpe, C.S., Bogus, K., and the Expedition 356 Scientists, *Indonesian Throughflow.* Proceedings of the International Ocean Discovery Program, 356: College Station, TX (International Ocean Discovery Program). **http://dx.doi.org/10.14379/iodp.proc.356.102.2017**

Gallagher, S.J., Fulthorpe, C.S., Bogus, K., Auer, G., Baranwal, S., Castañeda, I.S., Christensen, B.A., De Vleeschouwer, D., Franco, D.R., Groeneveld, J., Gurnis, M., Haller, C., He, Y., Henderiks, J., Himmler, T., Ishiwa, T., Iwatani, H., Jatiningrum, R.S., Kominz, M.A., Korpanty, C.A., Lee, E.Y., Levin, E., Mamo, B.L., McGregor, H.V., McHugh, C.M., Petrick, B.F., Potts, D.C., Rastegar Lari, A., Renema, W., Reuning, L., Takayanagi, H., and Zhang, W., 2017b. Site U1461. *In* Gallagher, S.J., Fulthorpe, C.S., Bogus, K., and the Expedition 356 Scientists, *Indonesian Throughflow.* Proceedings of the International Ocean Discovery Program, 356: College Station, TX (International Ocean Discovery Program). **http://dx.doi.org/10.14379/iodp.proc.356.106.2017**

Gallagher, S.J., Fulthorpe, C.S., Bogus, K., Auer, G., Baranwal, S., Castañeda, I.S., Christensen, B.A., De Vleeschouwer, D., Franco, D.R., Groeneveld, J., Gurnis, M., Haller, C., He, Y., Henderiks, J., Himmler, T., Ishiwa, T., Iwatani, H., Jatiningrum, R.S., Kominz, M.A., Korpanty, C.A., Lee, E.Y., Levin, E., Mamo, B.L., McGregor, H.V., McHugh, C.M., Petrick, B.F., Potts, D.C., Rastegar Lari, A., Renema, W., Reuning, L., Takayanagi, H., and Zhang, W., 2017c. Site U1462. *In* Gallagher, S.J., Fulthorpe, C.S., Bogus, K., and the Expedition 356 Scientists, *Indonesian Throughflow.* Proceedings of the International Ocean Discovery Program, 356: College Station, TX (International Ocean Discovery Program). **http://dx.doi.org/10.14379/iodp.proc.356.107.2017**

Gallagher, S.J., Fulthorpe, C.S., Bogus, K., Auer, G., Baranwal, S., Castañeda, I.S., Christensen, B.A., De Vleeschouwer, D., Franco, D.R., Groeneveld, J., Gurnis, M., Haller, C., He, Y., Henderiks, J., Himmler, T., Ishiwa, T., Iwatani, H., Jatiningrum, R.S., Kominz, M.A., Korpanty, C.A., Lee, E.Y., Levin, E., Mamo, B.L., McGregor, H.V., McHugh, C.M., Petrick, B.F., Potts, D.C., Rastegar Lari, A., Renema, W., Reuning, L., Takayanagi, H., and Zhang, W., 2017d. Site U1463. *In* Gallagher, S.J., Fulthorpe, C.S., Bogus, K., and the Expedition 356 Scientists, *Indonesian Throughflow.* Proceedings of the International Ocean Discovery Program, 356: College Station, TX (International Ocean Discovery Program). **http://dx.doi.org/10.14379/iodp.proc.356.108.2017**

Gradstein, F.M., Ogg, J.G., Schmitz, M.D., and Ogg, G.M. (Eds.), 2012. *The Geological Time Scale 2012:* Amsterdam (Elsevier).

Hallock, P., and Glenn, E.C., 1986. Large foraminifera: a tool for paleoenvironmental analysis of Cenozoic carbonate depositional facies. *Palaios,* 1(1):55–64. **http://dx.doi.org/10.2307/3514459**

James, N.P., Bone, Y., Kyser, T.K., Dix, G.R., and Collins, L.B., 2004. The importance of changing oceanography in controlling late Quaternary carbonate sedimentation on a high-energy, tropical, oceanic ramp: northwestern Australia. *Sedimentology,* 51(6):1179–1205. **http://dx.doi.org/10.1111/j.1365-3091.2004.00666.x**

Jones, H.A., 1973. *Marine Geology of the Northwest Australian Continental Shelf.* Bureau of Mineral Resources, Geology and Geophysics, Canberra, Australia (Australian Government Publishing Service), 136. **http://www.ga.gov.au/corporate_data/104/Bull_136.pdf**

Kennett, J.P., and Srinivasan, M.S., 1983. *Neogene Planktonic Foraminifera: A Phylogenetic Atlas:* Stroudsburg, PA (Hutchinson Ross).

Lumsden, D.N., 1979. Discrepancy between thin section and X-ray estimates of dolomite in limestone. *Journal of Sedimentary Petrology,* 49(2):429–436. **http://dx.doi.org/10.1306/212F7761-2B24-11D7-8648000102C1865D**

Marshall, N., Novak, V., Cibaj, I., Krijgsman, W., Renema, W., Young, J., Fraser, N., Limbong, A., and Morley, R., 2015. Dating Borneo's deltaic deluge: middle Miocene progradation of the Mahakam Delta. *Palaios,* 30(1):7–25. **http://dx.doi.org/10.2110/palo.2013.066**

Martini, E., 1971. Standard Tertiary and Quaternary calcareous nannoplankton zonation. *In* Farinacci, A. (Ed.), *Proceedings of the Second Planktonic Conference, Roma 1970:* Rome (Edizioni Tecnoscienza), 2:739–785.

Pearson, P.N., 1995. Planktonic foraminifer biostratigraphy and the development of pelagic caps on guyots in the Marshall Islands group. *In* Haggerty, J.A., Premoli Silva, I., Rack, F., and McNutt, M.K. (Eds.), *Proceedings of the Ocean Drilling Program, Scientific Results,* 144: College Station, TX (Ocean Drilling Program), 21–59. **http://dx.doi.org/10.2973/odp.proc.sr.144.013.1995**

Renema, W., 2007. Fauna development of larger benthic foraminifera in the Cenozoic of Southeast Asia. *In* Renema, W. (Ed.), *Topics in Geobiology* (Volume 29): *Biogeography, Time, and Place: Distributions, Barriers, and Islands.* Landman, N.H., and Jones, D.S. (Series Eds.): Dordrecht, The Netherlands (Springer), 179–215. **http://dx.doi.org/10.1007/978-1-4020-6374-9_6**

Ryan, G.J., Bernadel, G., Kennard, J.M., Jones, A.T., Logan, G.A., and Rollet, N., 2009. A precursor extensive Miocene reef system to the Rowley Shoals reefs, WA: evidence for structural control of reef growth or natural hydrocarbon seepage? *APPEA Journal,* 49:337–363.

Saito, T., 1976. Geologic significance of coiling direction in the planktonic foraminifer *Pulleniatina. Geology,* 4(5):305–309. **http://dx.doi.org/10.1130/0091-7613(1976)4<305:GSOCDI>2.0.CO;2**

van Hinsbergen, D.J.J., Kouwenhoven, T.J., and van der Zwaan, G.J., 2005. Paleobathymetry in the backstripping procedure: correction for oxygenation effects on depth estimates. *Palaeogeography, Palaeoclimatology, Palaeoecology,* 221(3–4):245–265. **http://dx.doi.org/10.1016/j.palaeo.2005.02.013**

Wade, B.S., Pearson, P.N., Berggren, W.A., and Pälike, H., 2011. Review and revision of Cenozoic tropical planktonic foraminiferal biostratigraphy and calibration to the geomagnetic polarity and astronomical time scale. *Earth-Science Reviews,* 104(1–3):111–142. **http://dx.doi.org/10.1016/j.earscirev.2010.09.003**

Young, J.R., 1998. Neogene. *In* Bown, P.R. (Ed.), *Calcareous Nannofossil Biostratigraphy:* Dordrecht, The Netherlands (Kluwer Academic Publishing), 225–265.